

Magnetic properties and their correlation with lattice dynamics in $\text{HoFe}_{1-x}\text{Cr}_x\text{O}_3$ ($0 \leq x \leq 1$) compounds

Ganesh Kotnana

A Dissertation Submitted to
Indian Institute of Technology Hyderabad
In Partial Fulfillment of the Requirements for
The Degree of Doctor of Philosophy



भारतीय प्रौद्योगिकी संस्थान हैदराबाद
Indian Institute of Technology Hyderabad

Magnetic Materials and Device Physics Laboratory
Department of Physics
Indian Institute of Technology Hyderabad
Kandi, Sangareddy – 502 285

March, 2018

Contents

Declaration.....	v
Approval Sheet.....	vi
Acknowledgements	vii
Abstract	x
Nomenclature	xiii
List of figures.....	xvi
List of tables.....	xxi
1 Introduction.....	1
1.1 Perovskites.....	1
1.2 Crystal field effect.....	4
1.3 Jahn-Teller distortion	7
1.4 Magnetism	9
1.4.1 Diamagnetism	9
1.4.2 Paramagnetism	9
1.4.3 Ferromagnetism	10
1.4.4 Anti-ferromagnetism	10
1.4.5 Ferrimagnetism	14
1.5 Magnetic interactions.....	14
1.5.1 Exchange interaction.....	14
1.5.2 Direct exchange interaction.....	17
1.5.3 Indirect exchange interaction	18
1.5.4 Super exchange interaction	18
1.5.5 Double exchange interaction	19
1.5.6 Dzyaloshinsky-Moriya interaction	20
1.6 Effect of magnetic ordering on phonons	22
1.6.1 Probing magnetism by Raman scattering.....	23
1.7 Rare earth orthoferrites.....	24
1.7.1 Crystal structure.....	24

1.7.2	Magnetic properties.....	28
1.8	Magnetocaloric effect (MCE)	29
1.8.1	Basic theory of magnetocaloric effect	33
1.9	Motivation and objectives.....	35
1.9.1	Band gap tuning and orbital mediated electron-phonon coupling.....	37
1.9.2	Magnetic and magnetocaloric properties.....	38
1.9.3	Spin – phonon coupling.....	39
2	Experimental techniques.....	42
2.1	Solid state reaction method.....	42
2.2	X-ray diffraction (XRD)	45
2.2.1	Rietveld refinement.....	47
2.3	Raman spectroscopy	48
2.4	UV-Vis-NIR spectrophotometer	51
2.5	Mössbauer spectroscopy	52
2.6	Magnetization measurement techniques	55
2.6.1	Vibrating sample magnetometer (VSM).....	55
2.6.2	Magnetic property measurement system (MPMS).....	58
2.6.3	Physical property measurement system (PPMS).....	61
3	Structural and optical properties of $\text{HoFe}_{1-x}\text{Cr}_x\text{O}_3$ ($0 \leq x \leq 1$) compounds..	64
3.1	Experimental details	64
3.2	Structural properties	67
3.3	Optical properties	78
3.4	Conclusions.....	83
4	Magnetic and magnetocaloric properties of $\text{HoFe}_{1-x}\text{Cr}_x\text{O}_3$ ($0 \leq x \leq 1$) compounds.....	84
4.1	Experimental details	84
4.2	Magnetic and Hyperfine interactions in $\text{HoFe}_{1-x}\text{Cr}_x\text{O}_3$ ($0 \leq x \leq 1$) compounds	86
4.3	Magnetocaloric properties and nature of magnetic phase transition	99
4.4	Specific heat studies on $\text{HoFe}_{0.25}\text{Cr}_{0.75}\text{O}_3$ compound	109
4.5	Conclusions.....	112

5 Spin-phonon coupling in $\text{HoCr}_{1-x}\text{Fe}_x\text{O}_3$ ($x = 0$ and 0.5) compounds.....	114
5.1 Experimental details	114
5.2 Room temperature Raman spectroscopic studies.....	114
5.3 Magnetic properties	119
5.4 Temperature dependent Raman scattering studies.....	119
5.5 Conclusions.....	127
6 Summary and scope of future work.....	128
Highlights of the thesis	134
References.....	135
List of publications	157

Declaration

I declare that this written submission represents my ideas in my own words, and where others' ideas or words have been included, I have adequately cited and referenced the original sources. I also declare that I have adhered to all principles of academic honesty and integrity and have not misrepresented or fabricated or falsified any idea/data/fact/source in my submission. I understand that any violation of the above will be a cause for disciplinary action by the Institute and can also evoke penal action from the sources that have thus not been properly cited, or from whom proper permission has not been taken when needed.

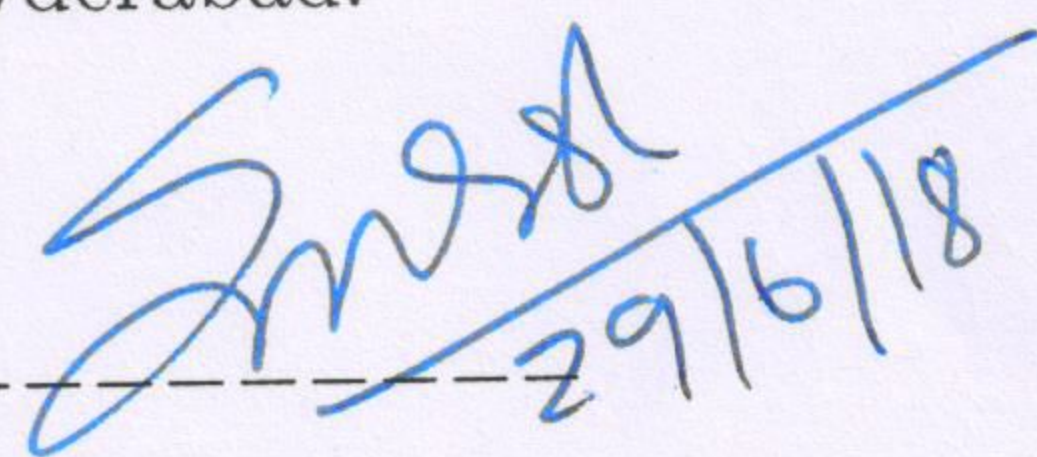
K. Ganesh

GANESH KOTNANA

PH13P1003

Approval Sheet

This thesis entitled "Magnetic properties and their correlation with lattice dynamics in $\text{HoFe}_{1-x}\text{Cr}_x\text{O}_3$ ($0 \leq x \leq 1$) compounds" by GANESH KOTNANA is approved for the degree of Doctor of Philosophy from IIT Hyderabad.

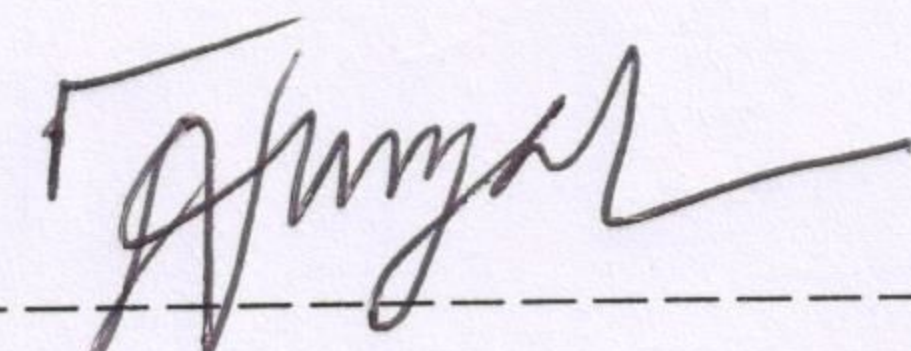


Prof. K. G. Suresh

Department of Physics

IIT Bombay

External Examiner

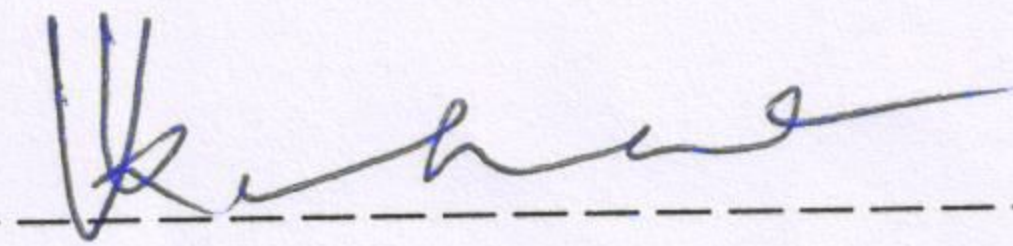


Dr. Suryanarayana Jammalamadaka

Associate professor

Department of Physics

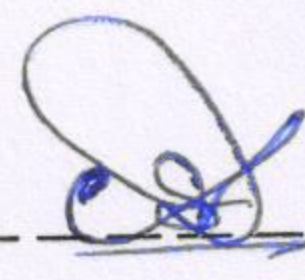
Adviser



Dr. V. Kanchana

IIT Hyderabad

Examiner



Dr. Atul Suresh Deshpande

IIT Hyderabad

Chairman

Acknowledgements

This thesis would not have been possible without the support of many people, who helped me directly or indirectly in the preparation and completion of this study. It gives me immense pleasure to convey my gratitude to all of them in my humble acknowledgement.

First and foremost, I would like to express my deepest gratitude to my research advisor **Dr. Suryanarayana Jammalamadaka** for giving me the opportunity to work under his guidance. His constant scientific, strategic and personal guidance, support and motivation were essential for the success of this thesis.

I am extremely thankful to my doctoral committee (DC) members, **Dr. V. Kanchana**, Department of Physics, IIT Hyderabad, India and **Dr. Atul Suresh Deshpande**, Department of Materials Science and Metallurgical Engineering, IIT Hyderabad, India, for the valuable feedback and support throughout my research period.

I would like to thank **Dr. J. Arout Chelvane**, AMG, DMRL, Hyderabad, India for providing experimental facility to carry out magnetization measurements. I am grateful to **Dr. P. D. Babu**, IUC-Mumbai, Mumbai, India for providing experimental facility to carry out magnetization, specific heat and neutron diffraction measurements.

I would also like to thank **Dr. V. Raghavendra Reddy**, **Dr. Vasant. G. Sathe** and **Dr. Alok Banerjee**, IUC-Indore, Indore, India for providing experimental facility to carry out Mössbauer spectroscopy measurements, temperature dependent Raman spectroscopy measurements, and magnetization measurements, respectively.

I am grateful to Faculty members and staff of Department of Physics for their kindness and support. I am also grateful to Indian Institute of Technology Hyderabad and Ministry of Human Resource and Development for providing the financial support to carry out the present thesis work.

I take this opportunity to thank my lab mates, Dr. M. Venkatnarayana, Mr. A. Soundara raj, Mr. Abhishek Talapatra, Mr. U. M. Kannan, Mr. Dwipak Prasad Sahu, Mr. Anjan Kumar Jena, Mr. Apu Kumar Jana, Mr. Bhibuti Bhushan Nayak, Mr. Ajit Kumar Sahoo for their wonderful company during my Ph.D. work.

I am very grateful for the good friends I have made during my stay at IIT Hyderabad. I thank Mr. P. Srinivas Reddy, Mr. V. N. S. Pradeep, Mr. Damodar Devarakonda, Dr. G. Vijay Kumar, Dr. Y. Raj Kumar for their help and support when I met with an accident. I also thank Mr. Kumar Raja Kandula, Mr. Aribina Narendra, Mr. Madhav Kumar for their help during measurements. I would also like to thank my fellow researchers, seniors for their constant support.

Most importantly, none of this would have been possible without the love and support of my family. I would like to express my heart-felt gratitude to my parents and family members for their constant support and encouragement for my higher studies.

GANESH KOTNANA

Dedicated to

My Parents and Family Members

Abstract

Perovskites with general formula ABO_3 (A is rare earth ion or Yttrium and B is a transition metal) have been the most versatile compounds in oxide research. Among various perovskite oxides, rare earth orthoferrite ($RFeO_3$) and orthochromite ($RCrO_3$) compounds with distorted perovskite structure have drawn considerable attention due to their unique physical properties and potential applications. Among $RFeO_3$ compounds, holmium orthoferrite ($HoFeO_3$) has been studied extensively for ultrafast recording applications. The crystal structure of $HoFeO_3$ is orthorhombic with a space group of $Pbnm$ at room temperature and possesses G-type antiferromagnetic with a magnetic ordering temperature (T_N) around 641 K. Apart from T_N , $HoFeO_3$ exhibits the spin reorientation (SR) transition of Fe^{3+} at 50 - 60 K.

According to Goodenough-Kanamori theory, Cr^{3+} is best choice for Fe^{3+} to show superior magnetic properties due to super exchange interactions, which may exhibit interesting magnetic properties and lattice dynamics. Hence, in this thesis we explored the structural, magnetic properties and their correlation with lattice dynamics in $HoFe_{1-x}Cr_xO_3$ ($0 \leq x \leq 1$) compounds.

The objectives of present thesis are

(a) Band gap tuning and orbital mediated electron-phonon coupling

To our knowledge, until now the electron - phonon coupling has been observed only in the Jahn - Teller active compounds. However, it would be very interesting if we can observe electron - phonon coupling in the Jahn - Teller inactive compound. For this purpose we choose $HoFeO_3$ which is a Jahn - Teller inactive, which may become Jahn - Teller active by substituting Cr. We anticipate that electron transfer mechanism can takes

place from Fe site to the Cr site when an incident photon energy equals to the ground state energy gap between Fe^{3+} and Cr^{3+} . *Hence, one of our aims is to understand the electron-phonon coupling in $\text{HoFe}_{1-x}\text{Cr}_x\text{O}_3$ ($0 \leq x \leq 1$) compounds which may leads to charge transfer between Fe and Cr through Raman spectroscopy.*

RFeO_3 and RCrO_3 compounds have been believed to possess p – type semiconducting behaviour, which may be very much useful in developing the optoelectronic devices. *However, to the best of our knowledge, detailed information on band gap values is not available in the literature neither on HoFeO_3 nor on HoCrO_3 . In addition, it would also be of great interest to monitor the change in the band gap value by applying the chemical pressure either at Fe site or Cr site.*

(b) Magnetic and magnetocaloric properties

RFeO_3 compounds have the complex spin structure between the rare earth (R) and the transition metal (TM) ions, which makes them of great interest to study their magnetic properties. Controlling the magnetic ordering temperatures and enhancement of magnetic properties in these compounds would be helpful in magnetic storage applications. One of the characteristic magnetic transition of RFeO_3 compound is spin reorientation (SR) during which the direction of easy axis of magnetization of Fe^{3+} sub lattice changes from one crystal axis to another upon varying the temperature. *Controlling the orientation of these spins can therefore lead to drastic changes in magnetic properties and offer unique functionality and potential applications in future spintronic devices. Hence, in the present work, we put our efforts in exploring the magnetic and local interactions in $\text{HoFe}_{1-x}\text{Cr}_x\text{O}_3$ ($0 \leq x \leq 1$) compounds through magnetization measurements and Mössbauer spectroscopy.* Apart from that, RFeO_3 and RCrO_3 compounds have been

explored for their magnetocaloric properties and suitability of them for magnetic refrigeration applications. *Hence, it is important to explore magnetocaloric properties and nature of magnetic transition in $\text{HoFe}_{1-x}\text{Cr}_x\text{O}_3$ ($0 \leq x \leq 1$) compounds.*

(c) Spin – phonon coupling

The discovery of the multiferroic materials, has allowed tuning the ferroelectric state (FE) with magnetic field and (anti) ferromagnetic state with electric field as there exists a strong coupling between various states. Atypical multiferroic behaviour has been observed in HoCrO_3 compound and the origin of ferroelectricity has been explained on the basis of probable displacement of Ho^{3+} ion and rotation of the oxygen octahedra in the non-centrosymmetric $\text{Pna}2_1$ space group. Contrary to this, the temperature dependent structural properties on HoCrO_3 compound have been investigated by X-ray and neutron diffraction and have shown no signature of structural phase transition below T_N . However, local structural change (which may lead to multiferroicity) through spin-phonon coupling has been demonstrated in RCrO_3 (R - Y, Lu, Gd, Eu and Sm) compounds using temperature dependent Raman spectroscopy. *Hence, in the present investigation we performed temperature dependent Raman spectroscopy in order to explore the coupling that exists between spin and phonon modes, which may lead to local structural change in $\text{HoCr}_{1-x}\text{Fe}_x\text{O}_3$ ($x = 0$ and 0.5) compounds.*

Keywords: *orthoferrite, spin-phonon coupling, spin reorientation, magnetism*

Nomenclature

ABBREVIATIONS

AFM	Antiferromagnetic
FM	Ferromagnetic
PM	Paramagnet
FE	Ferroelectric
R	Rare earth
TM	Transition Metal
DE	Double exchange
DM	Dzyaloshinsky-Moriya
JT	Jahn-Teller
CF	Crystal field
nm	Nanometer
MCE	Magnetocaloric effect
XRD	X-ray diffraction
VSM	Vibrating sample magnetometer
PPMS	Physical property measurement system
UV Vis NIR	Ultraviolet Visible Near infrared
ZFC	Zero field cooling
FC	Field cooling

FWHM	Full width half maximum
RC	Refrigeration capacity
RCP	Relative cooling power
eV	Electron volt
Oe	Oersted
kV	Kilovolt
kg	kilogram

NOTATIONS

ENGLISH SYMBOLS

A	Area, absorbance
T_C	Curie temperature
T_{SR}	Spin reorientation temperature
S	Entropy
H	Magnetic field
M	Magnetization
T	Temperature
C_p	Specific heat at constant pressure
H_C	Critical field
T_N	Neel temperature
d	Interplanar spacing
a, b, c	Lattice parameter (\AA)
n	Order of diffraction

K	Kelvin
k_B	Boltzmann constant
$^{\circ}\text{C}$	degree centigrade
I	Intensity
l	length
C	Concentration
J	Joule
E_g	Energy gap
h	Planks constant
g	gram
J_i	Interface exchange coupling coefficient

GREEK SYMBOLS

χ	Magnetic susceptibility
λ	Wavelength
μ_B	Bohr magneton
μ_0	Permittivity of vacuum
ν	frequency
ω	phonon wave number
v	velocity

List of figures

Figure	Caption	Page No.
1.1	(a) Ideal perovskite ABO_3 with cubic structure (b) AO_{12} cuboctahedra and (c) BO_6 octahedra	2
1.2	Crystal field effect in octahedral and tetrahedral environment	5
1.3	Splitting of both e_g and t_{2g} states in the octahedral environment due to Jahn-Teller effect	8
1.4	Variation of reciprocal of magnetic susceptibility with temperature for para-, ferro-, and antiferromagnetic materials	11
1.5	(a) to (d) Different types of antiferromagnetic arrangements in a magnetic unit cell	13
1.6	Schematic representation of exchange interactions of (a) antiferromagnetic and ferromagnetic orientation in direct interaction, (b) the indirect interactions through conduction electrons, (c) antiferromagnetic and ferromagnetic ordering in super-exchange interaction, depending on the bond angle, and (d) ferromagnetic ordering in double exchange interactions, Re-drawn from Ref. [37]	15
1.7	Crystal structure of $HoFeO_3$ compound. In the figure, blue sphere is holmium (Ho), the sphere in the octahedral is iron (Fe) and red sphere indicates oxygen (drawn using VESTA Software)	25
1.8	The magnetic entropy change for $H = 50$ kOe for the RCo_2 , RAl_2 , $Gd_5(Si_{1-x}Ge_x)_4$, $Mn(As_{1-x}Sb_x)$, $MnFe(P_{1-x}As_x)$ and $La(Fe_{13-x}Si_x)$ families plus a number of individual compounds versus the Curie temperature (From Ref. 84)	30
1.9	Schematic representation of two thermodynamic processes of a magnetocaloric effect when a magnetic field is applied or removed in a magnetic system. During isothermal process, total entropy change is non zero and negative, while temperature change is non zero and positive during adiabatic process	32
2.1	Schematic representation of different stages of sintering process [141]. Fig. 2.1 (a) denotes the particles of the compound before the process of heat treatment. The process of densification and	43

	Coarsening is shown in Fig. 2. 1 (b) and Fig. 2.2 (c) respectively. Fig. 2.1 (d) represents the particles of the compound after sintering	
2.2	Schematic diagram of x-ray diffraction pattern (XRD). P_1 and P_2 corresponds to different planes	46
2.3	Schematic of the energy level diagram of the Raman scattering	50
2.4	Schematic illustration of the principles of Mössbauer technique. ^{57}Co decays slowly into an excited state of the ^{57}Fe nucleus. As it is evident, 91% of the decay is rapid to $I = 3/2$ state which then decays to $I = 1/2$ ground state. This decay releases a 14.4 keV photon. The experiment was performed by moving the ^{57}Co source at a speed v relative to the sample which contain some ^{57}Fe nuclei. The detector measures the transmission of γ -rays through the sample which can be used to deduce the absorption	53
2.5	The effect of chemical shift, quadrupole splitting and magnetic splitting on the nuclear energy levels of ^{57}Fe	54
2.6	Schematic diagram of vibrating sample magnetometer (VSM)	56
2.7	Schematic diagram of DC SQUID (superconducting quantum interference device) [150]	59
2.8	Schematic diagram of DC SQUID system in the magnetic property measurement system (MPMS) [151]	60
2.9	Thermal connections to sample and sample platform in PPMS Heat Capacity Option [152]	62
3.1	Powder x-ray diffraction patterns of $\text{HoFe}_{1-x}\text{Cr}_x\text{O}_3$ ($0 \leq x \leq 1$). It is evident that all the compounds are formed in single phase	65
3.2	(a) Variation of lattice parameter with Cr composition. (b) Variation of tolerance factor (circle symbol) and FeO_6 average tilt angle (square symbol) with Cr composition	68
3.3	Energy Dispersive X-ray Spectroscopy of $\text{HoFe}_{1-x}\text{Cr}_x\text{O}_3$ compounds with (a) $x = 0$, (b) $x = 0.25$, (c) $x = 0.5$, (d) $x = 0.75$ and (e) $x = 1$ compositions	69
3.4	Room temperature Raman spectra of $\text{HoFe}_{1-x}\text{Cr}_x\text{O}_3$ ($0 \leq x \leq 1$) compounds with an excitation of 532 nm	72

3.5	(a) Franck-Condon (FC) mechanism for Jahn-Teller active perovskites. $v_{g,0}, v_{g,1}, v_{g,2}, \dots, v_{g,n}$ and $v_{e,0}, v_{e,1}, v_{e,2}, \dots, v_{e,n}$ represents the vibrational states of Fe^{3+} and Cr^{3+} respectively. For FC mechanism to happen for a vibrational mode, the virtual state $ v_r\rangle$ of Raman process must coincide with any vibrational state of electronically excited state. δ indicates lattice distortion due to Jahn – Teller effect as a result of charge transfer mechanism (b) Octahedral sites of Fe^{4+} and Cr^{2+} respectively. Dotted arrow in the figure indicates charge transfer mechanism and lattice relaxation	73
3.6	(a) Intensity variation of A_g peak and (b) wave number shift of A_g peak for the $HoFe_{1-x}Cr_xO_3$ ($0 \leq x \leq 1$) compounds	76
3.7	Absorption spectra of $HoFe_{1-x}Cr_xO_3$ ($0 \leq x \leq 1$) compounds	79
3.8	(a) Tauc’s plots to determine the band gap values of $HoFe_{1-x}Cr_xO_3$ ($0 \leq x \leq 1$) compounds. (b) Variation of the band gap with respect to Cr composition	80
3.9	(a) Shows the energy diagram of $HoFeO_3$ (b) Energy diagram of $HoCrO_3$ (c) probable energy diagram for $HoFe_{1-x}Cr_xO_3$. It is evident from the frame (c) that when $x < 0.5$, the valance band maxima (VBM) and conduction band minima (CBM) shifts to higher energy (dark red color). However, the shift in VBM is due to strong hybridization of d orbitals of Fe and Cr with p - orbitals of oxygen in valance band. When $x > 0.5$, band gap is dominated by unoccupied d -orbitals of Cr in conduction band which leads to increase in band gap (purple color)	82
4.1	Temperature (T) dependence of susceptibility (χ) pertinent to normalized magnetization (M) at (a) high temperature and (b) low temperature region for $HoFe_{1-x}Cr_xO_3$ ($0 \leq x \leq 1$) compounds	85
4.2	Variation of Néel temperature T_N of $HoFe_{1-x}Cr_xO_3$ ($0 \leq x \leq 1$) compounds with Cr^{3+} concentration	87
4.3	Temperature dependence of inverse molar susceptibility of $HoFe_{1-x}Cr_xO_3$ ($0 \leq x \leq 1$) compounds measured at 1000 Oe in the range of 5 – 300 K. Small dots represents the best fit of Curie-Weiss law	90
4.4	Room temperature ^{57}Fe Mössbauer spectrum of polycrystalline $HoFe_{1-x}Cr_xO_3$ ($0 \leq x \leq 1$) compounds. The experimental data is represented by the plus “+” symbol and the solid line is the best fit of the data	95

4.5	(a) – (d) First quadrant magnetization isotherms around Ho^{3+} ordering temperature with an applied field up to 60 kOe for $\text{HoFe}_{1-x}\text{Cr}_x\text{O}_3$ ($0.25 \leq x \leq 1$) compounds	98
4.6	First quadrant magnetization isotherms around (a) – (b) SR Cr^{3+} ordering temperature pertinent to $x = 0.25$ and $x = 0.50$ compounds, (c) – (d) compounds with an applied field up to 60 kOe for $\text{HoFe}_{1-x}\text{Cr}_x\text{O}_3$ ($0.25 \leq x \leq 1$) compounds	100
4.7	(a) – (d) Temperature dependence of the magnetic entropy $-\Delta S_M$ obtained from isothermal M vs. H data corresponding to Fig. 4.5 (a) – Fig. 4.5 (d) for $\text{HoFe}_{1-x}\text{Cr}_x\text{O}_3$ ($0.25 \leq x \leq 1$) compounds	103
4.8	(a) – (d) Temperature dependence of the magnetic entropy $-\Delta S_M$ obtained from isothermal M vs. H data corresponding to Fig. 4.6 (a) – Fig. 4.6 (d) for $\text{HoFe}_{1-x}\text{Cr}_x\text{O}_3$ ($0.25 \leq x \leq 1$) compounds	104
4.9	(a) – (d) Arrott plots deduced from magnetization isotherms corresponding to Fig. 4.5 (a) – Fig. 4.5 (d) for $\text{HoFe}_{1-x}\text{Cr}_x\text{O}_3$ ($0.25 \leq x \leq 1$) compounds	106
4.10	(a) – (d) Arrott plots deduced from magnetization isotherms corresponding to Fig. 4.6 (a) – Fig. 4.6 (d) for $\text{HoFe}_{1-x}\text{Cr}_x\text{O}_3$ ($0.25 \leq x \leq 1$) compounds	107
4.11	(a) Variation of specific heat C_p with temperature (T) at different magnetic fields (b) subtraction of phonon and electron contribution using third order polynomial from the specific heat data. Fitted data is shown as red line and experimental data is shown as black square symbol (c) variation of C_{mag}/T and S_{mag} with temperature (d) variation of adiabatic temperature change ΔT_{ad} with magnetic field for $\text{HoFe}_{0.25}\text{Cr}_{0.75}\text{O}_3$ compound	111
5.1	Room temperature Raman spectrum pertinent to (a) HoCrO_3 and (b) $\text{HoCr}_{0.5}\text{Fe}_{0.5}\text{O}_3$ compounds	115
5.2	Raman spectrum of HoCrO_3 compound in the temperature range 80 – 200 K	118
5.3	(a – e) variation of peak position pertinent to Raman modes of $B_{2g}(2)$, $A_g(4)$, $A_g(5)$, $B_{2g}(3)$ and $B_{3g}(3)$ respectively	120
5.4	(a) Temperature dependence of phonon mode peak position of $B_{3g}(3)$ mode. Inset shows the variation of line width of $B_{3g}(2)$ mode. (b)	123

Plot of $\Delta\omega$ (T) and $\frac{M^2(T)}{M_{\text{sat}}^2}$ as a function of temperature for $B_{3g}(3)$ mode pertinent to HoCrO_3 compound

- 5.5 Temperature evolution (200 – 300 K) of Raman spectrum for $\text{HoCr}_{0.5}\text{Fe}_{0.5}\text{O}_3$ compound 125
- 5.6 Temperature evolution (200 – 300 K) of the peak position of A_g mode in $\text{HoCr}_{0.5}\text{Fe}_{0.5}\text{O}_3$ compound, corresponding line width is shown in upper inset. Lower inset shows the temperature dependence of $B_{2g}(1)$ mode 126

List of tables

Table	Caption	Page No.
1.1	Effective magnetic moments for transition metals [29]	6
1.2	Geometrical parameters characterizing the crystal structure of RFeO ₃ compounds [76]	26
1.3	Néel temperatures of rare earth orthoferrites, RFeO ₃ with different rare earth ion [57]	27
3.1	Lattice parameter, cell volume, selected bond lengths, bond angles from Rietveld refinement pertinent to HoFe _{1-x} Cr _x O ₃ ($0 \leq x \leq 1$) compounds	66
3.2	Atomic percentage (%) of HoFe _{1-x} Cr _x O ₃ compounds obtained from EDAX results	70
4.1	Effective magnetic moment μ_{eff} , paramagnetic Curie temperature θ of HoFe _{1-x} Cr _x O ₃ ($0 \leq x \leq 1$) compounds obtained from the best fit of χ^{-1} vs. T by Curie-Weiss law	91
4.2	Parameters obtained from Mössbauer spectroscopy for HoFe _{1-x} Cr _x O ₃ ($0 \leq x \leq 1$) compounds at 300 K	96
5.1	The symmetry analysis of the Raman modes in HoCr _{1-x} Fe _x O ₃ ($x = 0$ and 0.5) compounds recorded at room temperature. The activating distortion and the main atomic motions which corresponds to each phonon mode are assigned based on Ref. [136-137], [159], [222]. This table also reveals comparison between reported results and present ones	116

Chapter 1

Introduction

1.1 Perovskites

The perovskite mineral with chemical formula CaTiO_3 has first been discovered in the Ural Mountains, Russia by Gustav Rose in 1839 and named after Russian mineralogist Lev Perovski [1]. The term perovskite is used to denote the compounds with general formula ABO_3 , where A denotes the trivalent rare earth metal (La, Gd, Pr, Ho, ...) or divalent alkali earth (Ca, Sr, Ba, ...) and B is a $3d$ transition metal (Mn, Cr, Fe, Co, Ti, ...). Indeed, there exists strong coupling between the spin, electric charge, and lattice degrees of freedom, due to which the complex and unusual properties have been observed in perovskite compounds [2]. The ideal perovskite ABO_3 has a cubic structure with a space group $\text{Pm}\bar{3}\text{m}$ [2] as shown in Fig. 1.1 (a). The common description of perovskite (ABO_3) is a simple cubic structure in which B-cations locates at the centre of the oxygen octahedra (BO_6), whereas the A-cations locates at the corner of the cube. Here, A cation is surrounded by twelve oxygen anions (AO_{12}) and B cation is surrounded by six oxygen anions (BO_6) as shown in Fig. 1.1 (b) and Fig. 1.1 (c) respectively. In general, manganites, orthoferrites, orthochromites, cobaltites, etc. consists perovskite structure and crystalize in orthorhombic structure. Despite forming in similar structure, their magnetic properties strongly depend on the electronic configuration of both the transition metal (TM) and rare earth (R) ions.

Much interest has been generated in these compounds due to the alteration of physical properties by doping at A-site or B-site. On top of that depending on the ionic size of the element that we substitute, one can have a flexibility to tune the

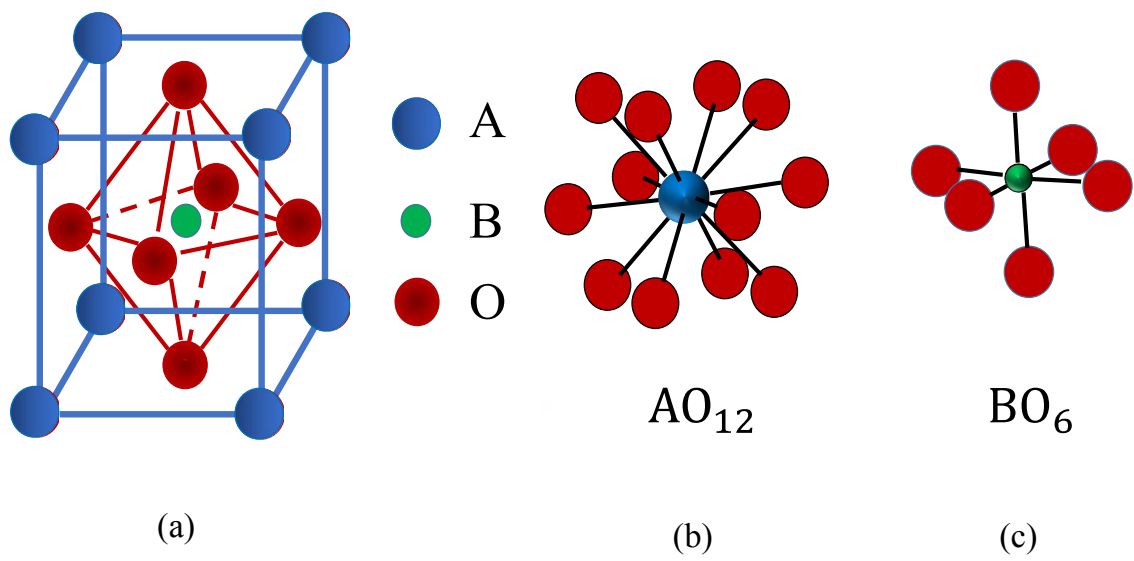


Figure 1.1: (a) Ideal perovskite ABO_3 with cubic structure (b) AO_{12} cuboctahedra and (c) BO_6 octahedra.

structural distortion and the electronic structure of the compound. Consequently, one can engineer the electrical, optical, thermal and magnetic properties [2]. Generally, the structure of perovskite compounds depends on the size ratio of the incorporated elements. In an ideal perovskite ABO_3 structure, the ionic radii of A-site cations consist similar size as oxygen anions and larger in size with respect to the B-site cations. Essentially, the bond angle B-O-B is 180° for ideal perovskite with cubic structure, however, due to difference in ionic radii of A and B ions, Jahn-Teller effect, etc., ideal cubic structure would be distorted to orthorhombic or other.

This distortion can be quantified using Goldschmidt's tolerance factor (GTF) [3], which can be defined as

$$t = \frac{r_A + r_O}{\sqrt{2}(r_B + r_O)} \quad \dots\dots (1.1)$$

where r_A , r_B and r_O are ionic radii of the A, B cations and oxygen anion respectively. The value of ' t ' is unity for an ideal cubic perovskite, but it would be less than unity ($t < 1$) for distorted perovskite. The value of ' t ' lies within the range of 0.8 – 1.0 for stable perovskite compounds. The oxidation state of B cation effects the value of ' t ' which vary from 0.886 to 1.139 for $A^+B^{5+}O^{3-}$ type perovskite compounds, from 0.822 to 1.061 for $A^{2+}B^{4+}O^{3-}$ type compounds, and from 0.832 to 1.012 for $A^{3+}B^{3+}O^{3-}$ type compounds. It has been found that the tolerance factor can only approximate the formation of a crystal with perovskite structure and doesn't give information about the space group [2].

The incorporation of different chemical elements at different sites leads to distortion of the perovskite structure away from the ideal cubic structure. Intense research has been devoted by many groups to study different distortions and their impact on the crystal symmetry [2, 4-15]. Three main types of distortions have been commonly discussed [10]:

- (i) Rotation of corner linked, rigid BO_6 octahedra

- (ii) Displacement of the A or B cation away from their high symmetry position
- (iii) Distortion of the BO_6 octahedra

In few cases these distortions coexist due to the flexibility of the perovskite structure. Typically, two structural distortions are possible from cubic structure, namely (i) rotation (tilt) of BO_6 octahedra around $[101]$ & $[010]$ and (ii) displacement of rare-earth (R^{3+}) ion. Distortion from cubic structure lowers the symmetry and leads to interesting properties such as colossal magneto-resistance [16-20], superconductivity [21-25], multiferroicity [26-28]. Among them, the multiferroicity can be due to displacement of A and B cations.

1.2 Crystal field effect

In general, the magnetism of $3d$ transition metals is due to partially filled outermost $3d$ -orbit electrons and the wave functions of the same are spatially extended compared to $4f$ electron wave function. The properties of these electrons would be modulated by crystal field (CF). Essentially, the crystal field (CF) is defined as the average electric field produced by neighbouring ions in the crystal. The size and nature of crystal field effect depend crucially on the symmetry of the local environment. In most of the transition metal oxides, the transition metal is surrounded by the oxygen ligands in octahedral and tetrahedral environment as shown in Fig. 1. 2. The crystal field arises in these cases due to electrostatic repulsion from the electrons in oxygen orbitals. Generally, $3d$ -orbitals have five degenerate energy levels such as $3d_{xy}$, $3d_{yz}$, $3d_{zx}$, $3d_{x^2-y^2}$ and $3d_z^2$. These five energy levels are categorized into e_g ($3d_z^2$ and $3d_{x^2-y^2}$) levels and t_{2g} ($3d_{xy}$, $3d_{yz}$ and $3d_{zx}$) levels. The difference between the energies of the t_{2g} and e_g orbitals in an octahedral or tetrahedral environment is Δ .

In octahedral environment, among the five sub orbitals, e_g ($3d_z^2$ and $3d_{x^2-y^2}$) orbitals of transition metal forms σ -bonds with $2p$ orbitals of oxygen (O^{2-}) ligand, due to which the degeneracy would be lifted by $3\Delta/5$. On the other hand, t_{2g} ($3d_{xy}$, $3d_{yz}$ and $3d_{zx}$) orbitals of transition metal forms π -bonding with $2p$ orbitals of O^{2-} , which leads to decrease in energy by $2\Delta/5$. Contrary to this, in case of transition metal in

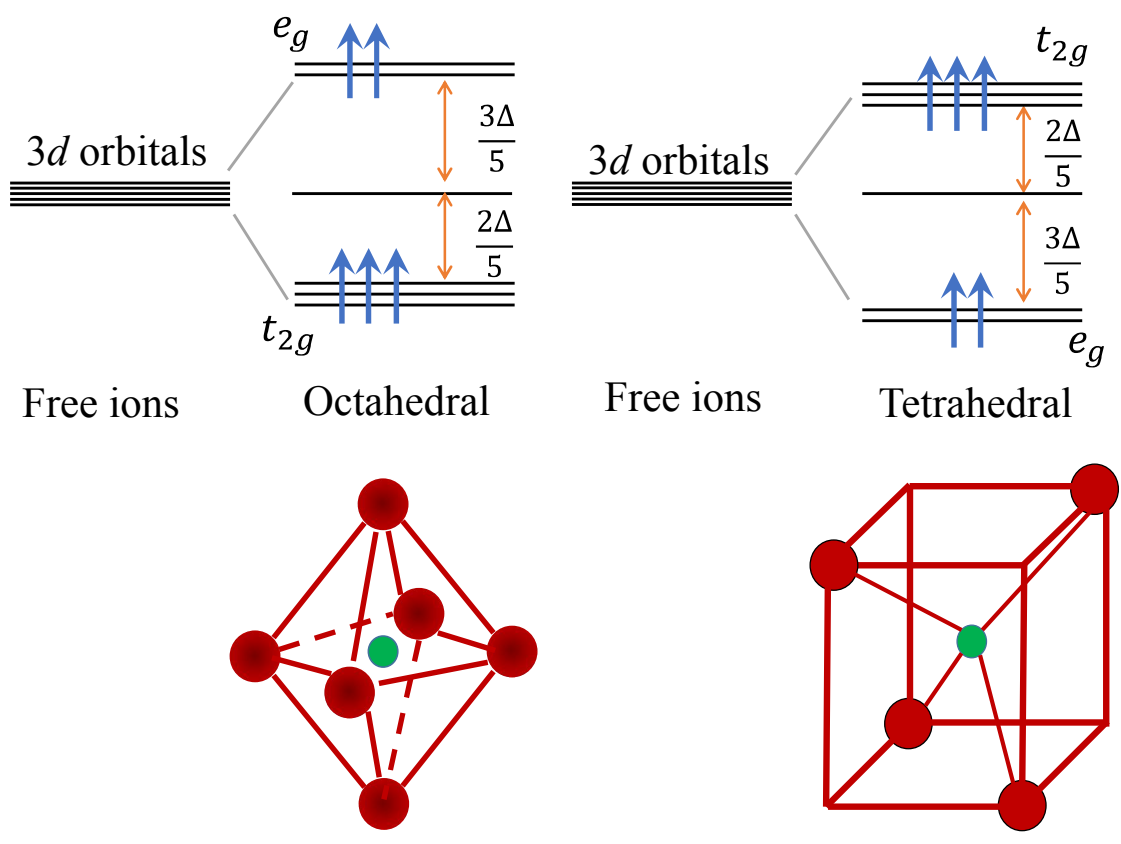


Figure 1.2: Crystal field effect in octahedral and tetrahedral environment.

Table 1.1: Effective magnetic moments for transition metals [29].

Ion	Configuration	Ground Level	$\mu_{eff} = g\sqrt{J(J+1)} \mu_B$	$\mu_{eff} = g\sqrt{S(S+1)} \mu_B$	$\mu_{eff} (\mu_B)$ experimental
Ti ³⁺ , V ⁴⁺	3d ¹	² D _{3/2}	1.55	1.73	1.70
V ³⁺	3d ²	³ F ₂	1.63	2.83	2.61
Cr ³⁺ , V ²⁺	3d ³	⁴ F _{3/2}	0.77	3.87	3.85
Mn ³⁺ , Cr ²⁺	3d ⁴	⁵ D ₀	0	4.90	4.82
Fe ³⁺ , Mn ²⁺	3d ⁵	⁶ S _{5/2}	5.92	5.92	5.82
Fe ²⁺	3d ⁶	⁵ D ₄	6.70	4.90	5.36
Co ²⁺	3d ⁷	⁴ F _{9/2}	6.63	3.87	4.90
Ni ²⁺	3d ⁸	³ F ₄	5.59	2.83	3.12
Cu ²⁺	3d ⁹	² D _{5/2}	3.55	1.73	1.83

tetrahedral environment, for t_{2g} orbitals the degeneracy would be lifted by $2\Delta/5$ and the energy of e_g orbitals would decrease by $3\Delta/5$ [29]. The crystal field that exists in transition metal may also modify the magnetic properties. For instance, in case of transition elements, due to quenching of orbital angular momentum, there is an observable difference in the value of theoretically calculated effective magnetic moment ($\mu_{eff} = g\sqrt{J(J+1)} \mu_B$) and experimentally measured values. As a result of quenching of orbital angular momentum $L = 0$, in the case of transition metals, $J = S$ (spin alone) [30], and (μ_{eff}) can be calculated using the relation $\mu_{eff} = g\sqrt{S(S+1)} \mu_B$, where the quantum numbers J and S refer to total and spin angular momentum respectively. Table 1.1 shows various transition metal ions, respective μ_{eff} and comparison for μ_{eff} that has been extracted using theory and experiment [29].

On the other hand, the magnetism in rare earth elements originates from the $4f$ electrons, which are deep inside from the outermost orbitals. Due to screening of $4f$ orbitals by $6s$ orbitals, the crystal field effect on $4f$ orbitals is less. Hence, $4f$ orbitals will not experience the crystal field effect from the neighbouring ions, due to which in case of rare earth elements, $J = L + S$. The effective magnetic moment of rare earth metals can be measured using the relation, $\mu_{eff} = g\sqrt{J(J+1)} \mu_B$.

1.3 Jahn-Teller distortion

In some of the transition metals, $3d$ orbitals with a specific valence state of an ion (Mn^{3+}) are asymmetrically occupied by the electrons within the degenerate e_g and t_{2g} energy levels in an octahedral environment. For example, Mn^{3+} with d^4 electronic configuration having four electrons in the d -orbitals and their occupancy is shown in the Fig. 1.3. Due to the crystal field, five degenerate d -orbitals of Mn^{3+} will split into higher energy e_g orbitals and lower energy t_{2g} orbitals. Out of four electrons, three would be occupied in t_{2g} orbitals and one in e_g orbitals, which is quite unstable. Due to this, the lattice (octahedral) undergoes spontaneous distortion in order to lower the crystal field symmetry by splitting the energy levels.

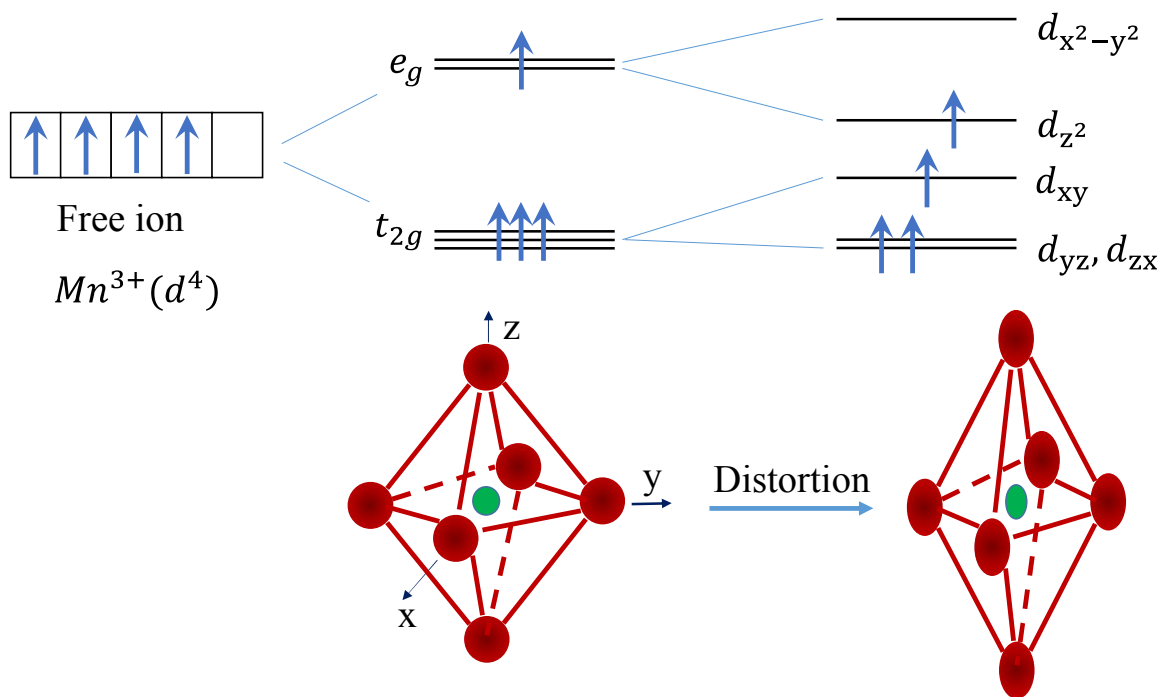


Figure 1.3: Splitting of both e_g and t_{2g} states in the octahedral environment due to Jahn-Teller effect.

This is called Jahn-Teller effect. In case of octahedral environment, distortion occurs in two ways such as elongation and compression as shown in Fig. 1.3. During the elongation, there would be a decrease in the overlap of oxygen p -orbitals with one of the e_g (d_z^2) orbital, and an increase of the overlap with other e_g ($d_{x^2-y^2}$) orbitals. Hence the energy of $d_{x^2-y^2}$ is more compared to that of d_z^2 orbital. Similarly in t_{2g} orbitals, d_{xy} level is lifted up compared to d_{yz} and d_{zx} levels. In the present thesis, both Fe^{3+} (d^5) and Cr^{3+} (d^3) are Jahn-Teller inactive ions.

1.4 Magnetism

We can classify magnetic materials based on the interaction between the magnetic moments. Apart from the interactions, we also have induced effects, which may lead to diamagnetism. In general, one can classify magnetic materials as follows [31]:

- (i) Diamagnetism (induced magnetism)
- (ii) Paramagnetism
- (iii) Ferromagnetism
- (iv) Anti-ferromagnetism
- (v) Ferrimagnetism

1.4.1 Diamagnetism

When an external magnetic field is applied to magnetic material, the orbital motion of electrons changes in such a way that the induced magnetic moment opposes the applied magnetic field (Lenz's law). The induced diamagnetic moment will persist as long as the material is exposed to magnetic field [32].

1.4.2 Paramagnetism

The presence of unpaired electron spins in paramagnetic material gives rise to a magnetic moment. The magnetic moments in this case are randomly oriented when the field is not applied. The magnetization of paramagnetic material is directly proportional to H/T [29]. The temperature dependent susceptibility of paramagnetic materials with N number of magnetic moments per unit volume each having magnetic moment of μ is given by Curie's law

$$\chi = \frac{\mu_0 N \mu^2}{3k_B T} = \frac{C}{T} \quad \dots (1.2)$$

where k_B is the Boltzmann's constant, $C = \frac{\mu_0 N \mu^2}{3k_B}$ is a Curie constant specific for each material [33]. The modified Curie law (Curie-Weiss law) is given by

$$\chi = \frac{C}{T - \theta} \quad \dots (1.3)$$

where θ represents the Curie temperature and can be positive, negative or zero. The positive value of θ indicates that the material is ferromagnetic below a certain temperature and θ corresponds to the transition temperature (Curie temperature T_C). On the other hand, the negative value of θ indicates that the material is antiferromagnetic below a certain temperature and θ corresponds to the transition temperature (Néel temperature T_N). A few examples of paramagnetic materials include salts of transition element, and oxides of the rare earths and the rare earth elements [31].

1.4.3 Ferromagnetism

In case of ferromagnetic materials, there would indeed be spontaneous magnetization within the domain and they exhibit cooperative phenomena. Weiss proposed a molecular field theory to understand the spontaneous magnetization behaviour in ferromagnetic materials [33]. According to Weiss, the magnetic moments within the domains of ferromagnetic materials align parallel to each other below T_C due to the presence of a molecular field $B_{mf} = \lambda M$ where λ is molecular field constant, and M is spontaneous magnetization of the material. Few examples of FM materials include transition metals like Fe, Co, and Ni with T_C values of 1043 K, 1394 K and 631 K [31] respectively.

1.4.4 Anti-ferromagnetism

In Antiferromagnetic (AFM) materials, the neighbouring magnetic moments of equal magnitude order antiparallel to each other below Néel temperature T_N , and

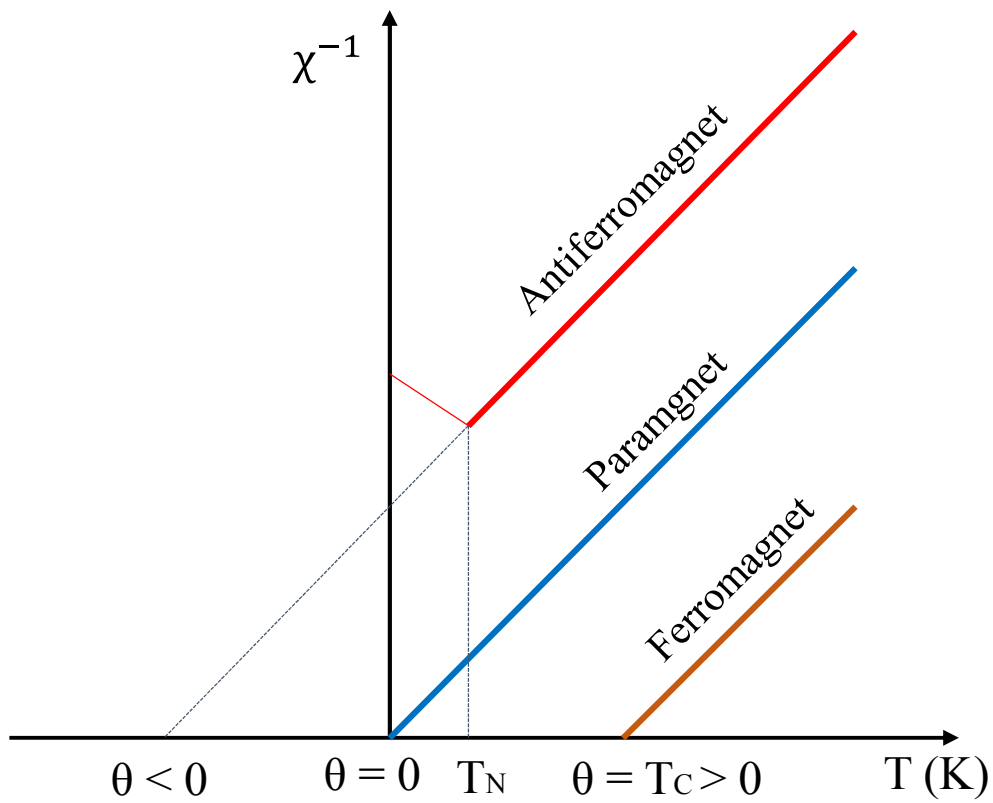


Figure 1.4: Variation of reciprocal of magnetic susceptibility with temperature for para-, ferro-, and antiferromagnetic materials.

gives rise to a zero net magnetization. Above T_N , these materials almost behave like a paramagnet. AFM materials show small and positive susceptibility.

The behaviour of inverse susceptibility of para-, ferro-, and antiferromagnetic material can be visualized using the equation 1.3 as shown in Fig. 1.4. Some examples of AFM materials and corresponding Néel temperatures are FeMn (67 K), MnO (116 K), CoO (292 K), FeO (116 K), Cr₂O₃ (307 K), α -Fe₂O₃ (950 K) [31].

Apart from the above, perovskite compounds also exhibits anti-ferromagnetism. In general, compounds which exhibit AFM nature show zero net magnetization as mentioned earlier. However, in some cases, the slight tilt of moments (canted nature) results a small net magnetization. It is in this context, perovskite oxide compounds with Pbnm space group are examples of canted anti-ferromagnets with a spin canting perpendicular to the spin easy axis [34]. Based on the interaction between magnetic moments in magnetic unit cell, different kinds of AFM ordering is possible as shown in Fig. 1.5 [35].

A-type: The coupling of magnetic moments in the same plane is ferromagnetic while inter-plane coupling is anti-ferromagnetic.

C-type: The coupling of magnetic moments in the same plane is anti-ferromagnetic while inter-plane coupling is ferromagnetic.

E-type: Following a cube edge, with in the plane, two spins point in one direction and the next two in the other direction.

G-type: The coupling of magnetic moments is anti-ferromagnetic both in intra-plane and inter-plane directions. This configuration is very common in cubic perovskites due to the fact that the super exchange interaction through oxygen atoms force all nearest-neighbour moments to align in anti-ferromagnetic nature. The examples for the perovskites with G-type magnetic configuration: rare earth orthoferrites (RFeO₃) [34] and orthochromites (RCrO₃) [36].

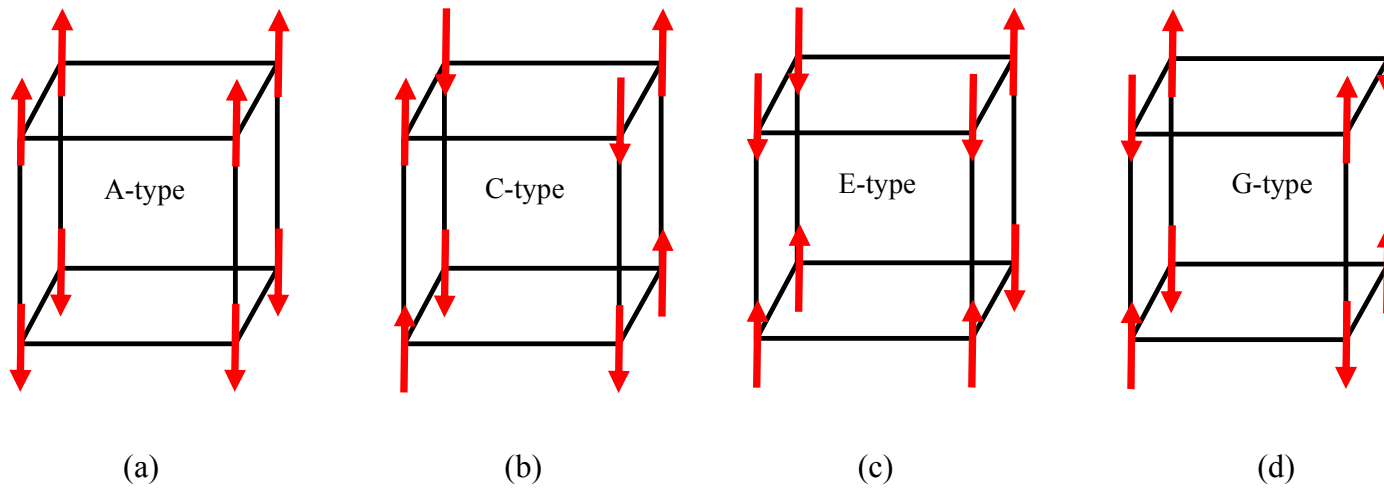


Figure 1.5: (a - d) Different types of antiferromagnetic arrangements in a magnetic unit cell.

1.4.5 Ferrimagnetism

In case of ferrimagnetic materials, the moments would be anti-ferromagnetically aligned. However, the magnitude of magnetic moments in both the sublattices will not be equal, which leads to net magnetization. Few examples of ferrimagnetic materials are MnFe_2O_4 , NiFe_2O_4 , CoFe_2O_4 , Fe_3O_4 , $\text{Ho}_3\text{Fe}_5\text{O}_{12}$, $\text{Gd}_3\text{Fe}_5\text{O}_{12}$, etc. [29].

1.5 Magnetic interactions

The magnetic properties of any magnetic material depend on the strength of exchange interactions between the magnetic moments associated with the ions in it [29]. The exchange interactions include direct exchange, indirect exchange, super exchange, double exchange, and Dzyaloshinsky-Moriya (DM) interaction.

1.5.1 Exchange interaction

Exchange interactions lie at the core of the phenomenon of long range magnetic order, and depends on the separation and spatial arrangement of localized magnetic moments in solids. The exchange interactions are quantum mechanical in nature due to the fact that the electrons are indistinguishable particles. These have been first treated by Heisenberg in 1928 to interpret the origin of the enormously large molecular field, which is responsible for the parallel alignment of magnetic moments in the domains of ferromagnetic materials [31].

Consider a simple model with just two electrons which have spatial coordinates r_1 and r_2 and corresponding wave functions $\psi_a(r_1)$ and $\psi_b(r_2)$ respectively. The total wave function of the system $\psi_a(r_1)\psi_b(r_2)$, which does not obey exchange symmetry. Therefore, the total wave function of the system can be written in terms of symmetrized or antisymmetrized product states which behave properly under the operation of particle exchange.

The total wave function for electrons must be antisymmetric so that the spin part must either be antisymmetric singlet state χ_s ($S = 0$) in the case of a symmetric

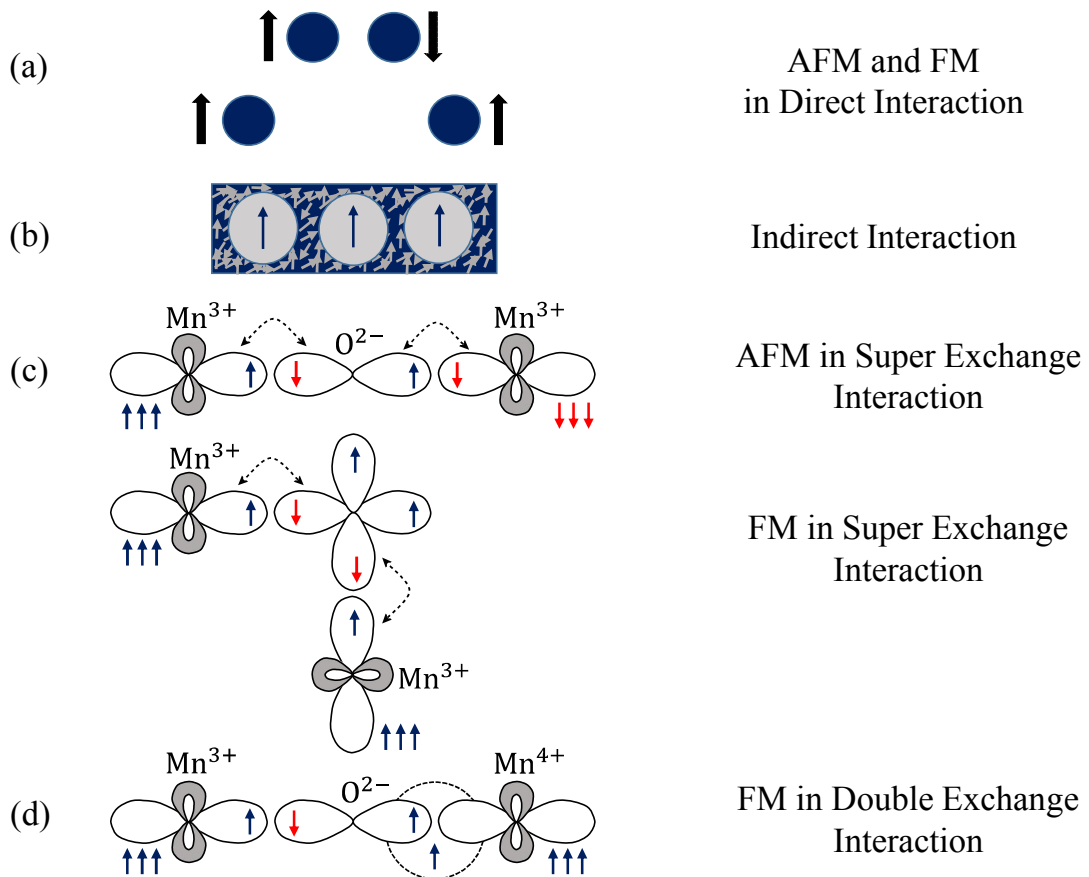


Figure 1.6: Schematic representation of exchange interactions of (a) antiferromagnetic and ferromagnetic orientation in direct interaction, (b) the indirect interactions through conduction electrons, (c) antiferromagnetic and ferromagnetic ordering in super-exchange interaction, depending on the bond angle, and (d) ferromagnetic ordering in double exchange interactions, Re-drawn from Ref. [37].

spatial state or symmetric triplet state χ_T ($S = 1$) in the case of an antisymmetric spatial state.

Therefore we can write the wave function for the singlet case ψ_S and the triplet case ψ_T as

$$\begin{aligned}\psi_S &= \frac{1}{\sqrt{2}} [\psi_a(\mathbf{r}_1)\psi_b(\mathbf{r}_2) + \psi_a(\mathbf{r}_2)\psi_b(\mathbf{r}_1)] \chi_S \\ \psi_T &= \frac{1}{\sqrt{2}} [\psi_a(\mathbf{r}_1)\psi_b(\mathbf{r}_2) - \psi_a(\mathbf{r}_2)\psi_b(\mathbf{r}_1)] \chi_T\end{aligned}\quad \text{..... (1.4)}$$

where both the spatial and spin parts of the wave function are included. The energies of the two possible states are

$$\begin{aligned}E_S &= \int \psi_S^* \hat{H} \psi_S \, d\mathbf{r}_1 \, d\mathbf{r}_2 \\ E_T &= \int \psi_T^* \hat{H} \psi_T \, d\mathbf{r}_1 \, d\mathbf{r}_2\end{aligned}\quad \text{..... (1.5)}$$

with the assumption that the spin parts of the wave function χ_S and χ_T are normalized. The difference between the two energies is

$$E_S - E_T = 2 \int \psi_a^*(\mathbf{r}_1)\psi_b^*(\mathbf{r}_2) \hat{H} \psi_a(\mathbf{r}_2)\psi_b(\mathbf{r}_1) \, d\mathbf{r}_1 \, d\mathbf{r}_2 \quad \text{..... (1.6)}$$

For a singlet state $S_1 \cdot S_2 = -3/4$ while for a triplet state $S_1 \cdot S_2 = 1/4$. Hence the Hamiltonian can be written in the form of an ‘effective Hamiltonian’

$$\hat{H} = \frac{1}{4} (E_S + 3E_T) - (E_S - E_T) \mathbf{S}_1 \cdot \mathbf{S}_2 \quad \text{..... (1.7)}$$

This is the sum of a constant term and a term which depends on spin. The constant can be absorbed into other constant energy terms, but the second term is more interesting. The exchange constant (or exchange integral), J is defined by

$$J = \frac{E_S - E_T}{2} = \int \psi_a^*(\mathbf{r}_1)\psi_b^*(\mathbf{r}_2) \hat{H} \psi_a(\mathbf{r}_2)\psi_b(\mathbf{r}_1) \, d\mathbf{r}_1 \, d\mathbf{r}_2 \quad \text{..... (1.8)}$$

and hence the spin-dependent term in the effective Hamiltonian can be written

$$\widehat{H}^{\text{spin}} = -2J \mathbf{S}_1 \cdot \mathbf{S}_2 \quad \text{..... (1.9)}$$

If $J > 0$, $E_S > E_T$ and the triplet state $S = 1$ is favoured (ferromagnetic state). If $J < 0$, $E_S < E_T$ and the singlet state $S = 0$ is favoured (anti – ferromagnetic state). This equation is relatively simple to derive for two electrons, but generalizing to a many-body system is far from trivial. Nevertheless, it was recognized in the early days of quantum mechanics that interactions shown in equation 1.9 is applicable only to nearest neighbour atoms. If we have many atoms in a system, the Hamiltonian can be written using the Heisenberg model as

$$\widehat{H} = -\sum_{ij} J_{ij} \mathbf{S}_i \cdot \mathbf{S}_j \quad \text{..... (1.10)}$$

where J_{ij} is the exchange constant between the i^{th} and j^{th} spins. The factor of 2 is omitted because the summation includes each pair of spins twice. Another way of writing equation 1.10 is

$$\widehat{H} = -2\sum_{i>j} J_{ij} \mathbf{S}_i \cdot \mathbf{S}_j \quad \text{..... (1.11)}$$

where $i > j$ avoids the ‘double-counting’ and hence the factor of two returns. Often it is possible to take J_{ij} as a constant J for nearest neighbour spins.

1.5.2 Direct exchange interaction

The interaction between the magnetic moments of neighbouring ions, which are close enough to overlap their wavefunctions is known as direct exchange interaction, and is shown in Fig. 1.6 (a). The strength of direct exchange interaction reduces with increase in the distance between neighbouring ions. When the ions are close enough for strong overlap of their wavefunctions, this interaction favours anti-ferromagnetic ordering of the spins, according to Pauli’s exclusion principle. However, ferromagnetic ordering of the spins is favourable when the ions are far enough to minimize the electron-electron repulsion.

1.5.3 Indirect exchange interaction

The interaction between the magnetic moments of ions through conduction electrons is known as indirect exchange interaction, and is shown in Fig. 1.6 (b). In the case of metals with localized electrons (e.g. for rare earth metal with $4f$ electrons), the overlap of the involved wave functions would be very small, and the direct exchange interaction may not be the dominating mechanism for magnetic properties. In such cases, the indirect interaction causes the magnetic ordering. The separation between the magnetic ions interacting through indirect exchange will decide the nature of magnetic coupling (ferromagnetic or anti-ferromagnetic).

1.5.4 Super exchange interaction

Super exchange interaction can be described as the interaction between the magnetic moments of two nearest neighbouring ions mediated through a non-magnetic ion. The interaction between the moments of a pair of Mn^{3+} cations through a non-magnetic oxygen (O^{2-}) anion is an example for this kind of interaction, and shown in Fig. 1.6 (c). The strength and sign of superexchange interaction depends on the occupation and orbital degeneracy of the involving magnetic ions. Goodenough [38] discussed most possible cases to consider in superexchange interaction. Their results were summarized as Goodenough-Kanamori rules [39-41], which were reformulated by Anderson [42] in a simple way that makes it unnecessary to consider the oxygen.

(i) If the lobes of singly occupied $3d$ orbitals corresponding to two metal (M) cations point toward each other, the exchange is strong due to large overlap, and gives rise to anti-ferromagnetic interaction. This is the usual case for 120° - 180° M-O-M bonds, and shown in Fig. 1.6 (c).

Out of two valence electrons of O^{2-} , the spin down electron forms covalent bonding with spin up electron of left side Mn^{3+} cation, while the spin up electron of oxygen forms covalent bonding with spin down electron of right side Mn^{3+} cation. In this case, the interaction between the electrons of Mn^{3+} cations is antiferromagnetic.

(ii) If the overlap integral between singly occupied $3d$ orbitals corresponding to two metal (M) cations is zero by symmetry, the exchange is relatively weak and gives rise to ferromagnetic interaction. This is the case for 90° M-O-M bonds, and shown in Fig. 1.6 (c).

Out of two valence electrons of O^{2-} , the spin down electron form covalent bonding with spin up electrons of left side Mn^{3+} cation, while the spin down electron of another O^{2-} orbital form a covalent bonding with spin up electrons of down side Mn^{3+} cation. In this case, the interaction between the electrons of Mn^{3+} cations is ferromagnetic.

(iii) If the lobes of singly occupied $3d$ orbitals of a cation have an overlap with an empty or doubly occupied orbitals of a cation of the same type, the exchange is relatively weak and gives rise to ferromagnetic interaction.

Super exchange interaction between metal cations mediated through a non-magnetic anion is more commonly antiferromagnetic in nature due to the fact that the overlap integrals likely to be larger than zero and bond angle M - O - M would be $> 90^\circ$ [38].

1.5.5 Double exchange interaction

Double exchange interaction is the interaction between magnetic moments of ions with mixed valence configuration. This mechanism was proposed by Zener [43-44] in 1951, and is essentially a super exchange interaction between $3d$ atoms. Zener model proposed that, hopping of conduction electrons between two ions can be possible only if the electron spins of two ions are parallel. It takes place only in an environment containing ions of more than one oxidation state (example Mn^{3+} , Mn^{4+}), and as shown in Fig. 1.6 (d). The magnetic interaction between Mn^{3+} and Mn^{4+} ions through oxygen (O^{2-}) ion can be explained on the basis of Zener model as follows: the simultaneous transfer of an electron from Mn^{3+} to oxygen and from oxygen to Mn^{4+} ion is involved in this process, so that it is called double exchange (DE) interaction. Out of two valence electrons of O^{2-} , the spin down electron form covalent bonding with spin up electron of left side Mn^{3+} cation, while the spin up

electron of oxygen forms ionic bonding with right side Mn^{4+} cation. In this case, the interaction between the electrons of Mn^{3+} and Mn^{4+} cations is ferromagnetic in nature. In the case of manganese ions (Mn^{3+} , Mn^{4+}) with parallel spins, DE always prefers the ferromagnetism, due to the fact that the electrons transfer becomes more difficult due to onsite Hund's coupling when the spins of manganese ions are antiparallel. The electron transfer also depends on Mn-O-Mn bond angle. If the bond angle is 180° , the overlap of d -orbitals of manganese and p -orbitals of oxygen is large and the interaction is strong. If the bond angle deviates from 180° , the overlap reduces and the interaction becomes very weak.

1.5.6 Dzyaloshinsky-Moriya interaction

Some magnetic materials with uniaxial or lower symmetry favours the canted nature of the spins away from the original antiferromagnetic alignment and produce a weak ferromagnetism perpendicular to anti-ferromagnetic axis. Essentially, in Dzyaloshinsky – Moriya (DM) interaction, spin – orbit coupling plays a major role by producing excited states on one magnetic ion. Indeed there would be an interaction between these excited states and the ground state of other ion through exchange interactions. This concept was first proposed by Igor Dzyaloshinsky [45] and later by Toru Moriya [46-47]. The DM interaction, also called as antisymmetric exchange interaction between two neighbouring magnetic spins via a non-magnetic ligand, which can be expressed as

$$H_{DM} = D_{ij} \cdot (S_i \times S_j) \quad \dots\dots (1.12)$$

where S_i and S_j are the spins of two magnetic ions involving in the interaction, and D_{ij} is a DM constant. The DM vector \mathbf{D}_{ij} is proportional to the spin-orbit coupling constant and depends on the position of the ligand ion between two magnetic transition metal ions. The vector \mathbf{D}_{ij} lies along the axis of symmetry [48].

The DM interaction plays a role in the orienting magnetic moments in the case of orthoferrites and orthochromites. Weak ferromagnetism in the orthoferrites has been attributed to the antisymmetric exchange interaction (DM interaction)

between magnetic ions. For a perovskite ABO_3 structure, the substitution in the A-site and B-site and a size mismatch between the A and B ions usually make the oxygen octahedral tilt and rotate, resulting in a distortion. Therefore, each oxygen ion sandwiched between two neighbouring B ions may move away from the middle point, giving a bent B-O-B bond and breaking the B-B axis rotation symmetry. This bent B-O-B bond will change the DM interaction as a relativistic correction to the superexchange between the magnetic B ions. Through the above analysis, the strength of the antisymmetric B-O-B exchange interactions are changed by structural deformation and tilting, which is caused by element substitution in perovskite.

In $HoFeO_3$ compound, below 30 K it is the contributions from both Fe and Ho and will have the form [49]

$$\begin{aligned}
 E_{\text{antisymmetric}} = & \sum_{i=1,4}^{j=i+1,4} D_{\text{Fe-Fe},i,j} \cdot (M_{\text{Fe}}(i) \times M_{\text{Fe}}(j)) + D_{\text{Ho-Ho},i,j} \cdot (M_{\text{Ho}}(i) \times M_{\text{Ho}}(j)) \\
 & + \sum_{i=1,4}^{j=1,4} D_{\text{Fe-Ho},i,j} \cdot (M_{\text{Fe}}(i) \times M_{\text{Ho}}(j))
 \end{aligned}
 \tag{1.13}$$

The $D_{n,i,j}$ are Dzyaloshinski vectors include contributions from single ion anisotropy as well as antisymmetric exchange. This antisymmetric exchange energy varies rapidly in the temperature range in which the Ho sub-lattices are ordering. While the ordered Ho moments are small it is dominated by the terms containing $D_{\text{Fe-Fe}}$ and the sense of ferromagnetic moment is determined by the first summation in the above equation 1.13. As the degree of Ho order increases the terms in the third summation, which containing products of the Fe and Ho moments, begin to exceed those dependent on Fe moments only and the sense of the ferromagnetic moment may change. Finally at the lowest temperatures when the Ho moments approach saturation the Ho-Ho interactions dominate. Doping of Cr^{3+} ions at Fe^{3+} site in $HoFeO_3$ compound leads to change the Fe-O-Fe angle which in turn effect the DM interaction the doped compounds.

From the above it is clear that there exist various magnetic interactions depending on the compound that we choose. These magnetic interactions would completely depend on the structural properties such as lattice parameter, kind of symmetry that exists in particular compound. This global change in structural parameters may also influence the local structure, which is in terms of change in phonon modes. From the above, it is clear that there exists strong correlation between the local structure and magnetic interactions, which will be of great interest to study.

1.6 Effect of magnetic ordering on phonons

An important aspect of real spin system is the influence of the spin – spin interactions on lattice dynamics. Since the strength of the exchange forces depend crucially on bond length and bond angles, if there is any modulation in the local arrangement of the magnetic ions, the exchange interactions would alter, which hints that there exists a coupling between lattice and spin. The spin-phonon coupling in the case of $\text{La}_{1-x}\text{Mn}_x\text{O}_3$ perovskite oxide with Pnma structure has been modelled by Granado *et. al.* [50]. This modeling starts from the superexchange based on nearest neighbour $\text{Mn}_i - \text{Mn}_j$ spin Heisenberg Hamiltonian

$$H_{spin} \approx - \sum_{i,j>1} J_{ij} \langle S_i \cdot S_j \rangle \quad \dots\dots (1.14)$$

where J_{ij} is the superexchange integral, $\langle S_i \cdot S_j \rangle$ is the scalar spin correlation function and the summation in j is over three nearest neighbours of the i^{th} Mn ion such that each pair is not considered twice. The change of J_{ij} due to α^{th} Raman active normal mode of vibration, ΔJ_{ij}^α , can be obtained by a second-order Taylor expansion on the O^{2-} displacements associated to that mode:

$$\Delta J_{ij}^\alpha (u_k^\alpha(t)) = [u_k^\alpha(t) \cdot \nabla_k] J_{ij} + \frac{1}{2} [u_k^\alpha(t) \cdot \nabla_k]^2 J_{ij} \quad \dots\dots (1.15)$$

where $u_k^\alpha(t)$ is the displacement vector from the equilibrium positions of the k^{th} O^{2-} ion, placed between the i^{th} and j^{th} Mn^{3+} ions for the α^{th} normal mode of vibration. Notice that we have assumed first neighbours interactions only. Inserting

equation 1.15 into equation 1.14 and considering the Hamiltonian $H = H_{\text{latt}} + H_{\text{spin}}$, the total potential energy of a Raman active normal mode α is separated into “lattice” and “spin” contributions, where the “spin” term may be written in the form

$$U_{spin}^{\alpha} = \frac{1}{2} \sum_k u_k^{\alpha}(t) D_{spin} u_k^{\alpha}(t) \quad \dots (1.16)$$

The angular frequency shift of the phonon due to magnetic ordering is then given by

$$(\Delta\omega_{\alpha})_{s-ph} = \frac{1}{2\mu_{\alpha}\omega_{\alpha}} \sum_k \hat{u}_k^{\alpha}(t) D_{spin} \hat{u}_k^{\alpha}(t) \quad \dots (1.17)$$

where μ_{α} is the reduced mass and $\hat{u}_k^{\alpha} = \frac{u_k^{\alpha}}{|u_k^{\alpha}|}$.

Un-doped LaMnO₃ presents Pnma crystal structure, and in this case we can write

$$(\Delta\omega_{\alpha})_{s-ph} = -\frac{N}{2\mu_{\alpha}\omega_{\alpha}} \left\{ 2\langle S_i \cdot S_j \rangle_{xz} [\hat{u}_{O1}^{\alpha}(t) \cdot \nabla_{O1}]^2 J_{xz} + \langle S_i \cdot S_j \rangle_y [\hat{u}_{O2}^{\alpha}(t) \cdot \nabla_{O2}]^2 J_y \right\} \quad \dots (1.18)$$

Where N is the number of Mn³⁺ ions and O1 and O2 refer to an xz-plane and a y-direction O²⁻ ion, respectively.

1.6.1 Probing magnetism by Raman scattering

As we mentioned earlier, it is important to understand the correlation between spin and lattice dynamics. Phonon scattering measurements using Raman spectroscopy has been widely used to investigate the changes in the lattice dynamics as it offers an opportunity to probe the local structural changes [51]. However, one can also apply Raman scattering technique to magnetic materials to investigate the magnetic phase transition only if spin-phonon coupling has a clear influence on phonon scattering [50]. This is an indirect way of probing magnetism by analysing the effect of the ordering of the magnetic moments on the structure. At a magnetic phase transition, the alignment of spins induces strain in the magnetic material by means of magnetostriction. Magnetostriction causes a distortion in the lattice and thus

magnetic ordering couples to the phonon system. The interaction between phonon frequency and the magnetic moments is commonly assumed [52] as

$$\omega_{\text{sp}} = \omega_0 + \gamma \langle S_i S_j \rangle \quad \dots\dots (1.19)$$

where ω_{sp} , ω_0 , γ , S_i and S_j represents the frequency due to spin-phonon coupling, undisturbed frequency, the spin-phonon coupling constant, and spin moments corresponds to spin at i^{th} and j^{th} sites respectively.

1.7 Rare earth orthoferrites

Rare earth orthoferrites with chemical formula RFeO_3 (R is rare earth ion) with distorted perovskite structure has appealed continued experimental and theoretical interest due to their novel magnetic and magneto-optical properties [53-56]. These compounds have been the subject of intense research, which aimed at a better understanding of magnetic properties under external parameters such as temperature, electric field, magnetic field, pressure, etc. [34, 57-58]. Apart from their fundamental interest, due to higher velocity of domain walls (~ 20 km/s) orthoferrites have been explored in the devices based on memory [59-65]. Apart from the above, these compounds have potential applications in magneto-optical current sensors, magnetic sensors, light spot position measurements, magneto-optical rotational speed sensors and fast lasting optical switches [66-69]. On top of that these materials also have much potential for photocatalytic activity [70], solid oxide fuel cells [71], gas sensors [72], detection of ozone in monitoring environment [73], and multiferroic behaviour [74-75].

1.7.1 Crystal structure

At ambient conditions, RFeO_3 compounds crystallize in an orthorhombic structure with Pbnm space group. Essentially, the orthoferrite Pbnm phase can be derived from the ideal cubic perovskite phase Pm3m by octahedral rotations. The unit cell of orthoferrite consists four formula units. Figure 1.7 depicts the crystal structure of orthoferrite. Tilts of FeO_6 octahedral are the predominant type of distortions in the case of rare earth ferrite. Glazer [6] introduced a notation to describe the octahedral

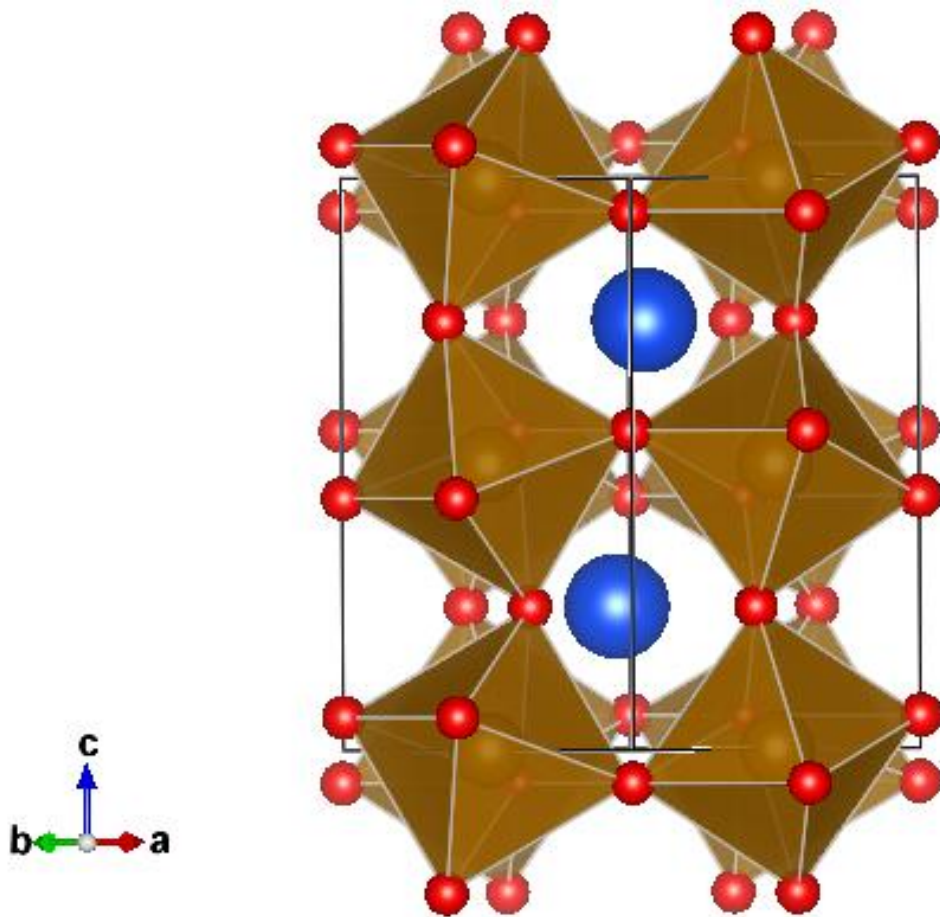


Figure 1.7: Crystal structure of HoFeO₃ compound. In the figure, blue sphere is holmium (Ho), the sphere in the octahedral is iron (Fe) and red sphere indicates oxygen (drawn using VESTA Software).

Table 1.2: Geometrical parameters characterizing the crystal structure of RFeO₃ compounds [76].

RFeO ₃	Ionic radii $r_{R^{3+}}$ (Å ^o)	Tolerance factor (t)	D^a	ϕ_1 (degree)	ϕ_2 (degree)	$\langle \phi \rangle$
PrFeO ₃	1.179	0.892	0.00663	16.249	16.776	16.512
NdFeO ₃	1.163	0.886	0.00964	17.382	17.616	17.499
SmFeO ₃	1.132	0.876	0.01381	18.226	18.884	18.555
EuFeO ₃	1.120	0.871	0.01632	19.490	19.750	19.620
GdFeO ₃	1.107	0.867	0.01823	19.934	20.036	19.985
TbFeO ₃	1.095	0.863	0.01879	20.613	20.774	20.693
DyFeO ₃	1.083	0.859	0.02035	21.090	21.369	21.230
HoFeO ₃	1.072	0.855	0.02133	21.644	21.669	21.656
ErFeO ₃	1.062	0.851	0.02200	22.405	22.096	22.250
TmFeO ₃	1.052	0.848	0.02130	22.762	22.387	22.574
YbFeO ₃	1.042	0.844	0.02214	23.218	22.976	23.097
LuFeO ₃	1.032	0.841	0.02242	23.620	23.269	23.444

^a D is the orthorhombic deformation, $D = (1/3) \sum_i |a_i - \langle a \rangle| / \langle a \rangle$ where a_i are the cell parameters a , c , $b/\sqrt{2}$ and $\langle a \rangle = (abc/\sqrt{2})^{1/3}$.

Table 1.3: Néel temperatures of rare earth orthoferrites, $RFeO_3$ with different rare earth ion [57].

Rare earth ion at $RFeO_3$	La	Pr	Nd	Sm	Eu	Gd	Tb	Dy	Y	Ho	Er	Tm	Yb	Lu
Néel temperature T_N (K)	740	707	687	674	662	657	647	645	640	639	636	636	627	623

tilt system of a perovskite crystal. These rotations are described with respect to cubic axis x-, y-, and z- and represented by the symbols a, b and c as shown in Fig. 1.7. In Glazer’s notation, these octahedral tilts can be expressed as $a^+b^+a^-$ [6] or rotations around $[101]_{pc^-}$, $[010]_{pc^-}$, and $[111]_{pc^-}$ pseudo-cubic (pc) axis [2].

In the above notations, superscripts “+” and “-” indicates the sense of rotation in successive layers. The symbol “+” stands for octahedral rotation in the successive layer in the same direction, i.e. in-phase. On the other hand, “-” stands for anti-phase octahedral tilt in the successive layer. Zero is used as superscript in the case of no rotation around a particular axis. For example, $a^0a^0a^0$ is used to denote cubic Pm3m structure without octahedral tilt [2, 6].

Table 1.2 summarizes the structural parameters such as tolerance factor t , orthorhombic deformation D , FeO_6 octahedral tilt angles ϕ_1 , ϕ_2 and average tilt angle $\langle\phi\rangle$ which are used to characterize the crystal structure of $RFeO_3$ [76] compounds. An increase in the orthorhombic deformation D as well as decrease in the tolerance factor ‘ t ’ with respect to a decrease in ionic radii of rare earth metal ($r_{R^{3+}}$) is evident from the Table 1.2. This indicates a distortion in the lattice, due to which the FeO_6 octahedra will tilt for self-accommodating in the lattice matrix.

1.7.2 Magnetic properties

The presence of two magnetic ions, rare earth (R^{3+}) and iron (Fe^{3+}) in the crystal structure of $RFeO_3$ lead to existence of complex magnetic interactions such as $R^{3+}-R^{3+}$, $Fe^{3+}-Fe^{3+}$, and $R^{3+}-Fe^{3+}$. Upon changing the temperature, the complex interactions as mentioned above would alter and lead to interesting magnetic properties such as magnetization reversal [77], exchange bias [78], Morin transition [78], multiferroicity [75] etc. Particularly, Fe^{3+} moments in these orthoferrites exhibit canted antiferromagnetic (AFM) state and show a weak ferromagnetic moment (WFM) below their Néel temperature (620-750 K) respectively as shown in Table 1.3 [57]. Essentially, Fe^{3+} moments order antiferromagnetically with an angle to c-axis due to Dzyaloshinsky-Moriya antisymmetric exchange interaction. Hence,

the magnetic moments parallel to c-axis cancels out, while the moments perpendicular to c-axis gives rise to a weak spontaneous magnetization.

On the other hand, the R^{3+} moments magnetically order below a transition temperature much lower than the Néel temperature. Above this transition temperature, R^{3+} moments are in paramagnetic regime, but partially magnetized under the molecular field of Fe^{3+} moments. One of the distinctive magnetic transitions of $RFeO_3$ compounds is spin reorientation (SR) during which the direction of magnetic moments of Fe^{3+} sub lattice changes from one crystal axis to other upon varying the temperature due to domination of R^{3+} - Fe^{3+} interaction over Fe^{3+} - Fe^{3+} interaction.

The crystal symmetry of $RFeO_3$ compounds allows three magnetic configurations for Fe^{3+} moments labelled as Γ_4 (G_x, A_y, F_z), Γ_2 (F_x, C_y, G_z) and Γ_1 (A_x, G_y, C_z) [34]. Here G, C, A and F represents antiferromagnetic, weak anti-ferromagnetic, weak anti-ferromagnetic, and ferromagnetic vectors respectively in terms of Bertaut's notations [79] for cubic structure. Among the above mentioned magnetic structures, Γ_1 configuration does not display any net magnetic moment, whereas Γ_2 and Γ_4 configurations exhibit weak ferromagnetic moments along x- and z-directions respectively. Below T_N , Fe^{3+} moments align according to Γ_4 . In the case of $RFeO_3$ compounds having magnetic R^{3+} , with decreasing temperature below T_N , the high temperature Γ_4 phase change to low temperature Γ_2 phase separated by an intermediated magnetic configuration Γ_{24} phase due to R^{3+} - Fe^{3+} interaction [80]. $DyFeO_3$ compound shows $\Gamma_4 \rightarrow \Gamma_1$ transition while $\Gamma_4 \rightarrow \Gamma_2$ is absent [81].

1.8 Magnetocaloric effect (MCE)

The demand for the materials which can be used in magnetic refrigeration technology has ever been growing due to their applicability at room temperature as well as cryogenic temperature. The materials whose temperature alter in response to external stimulation such as mechanical, electric, and magnetic are referred as caloric (solid) materials [82-86]. Refrigeration using the caloric materials have

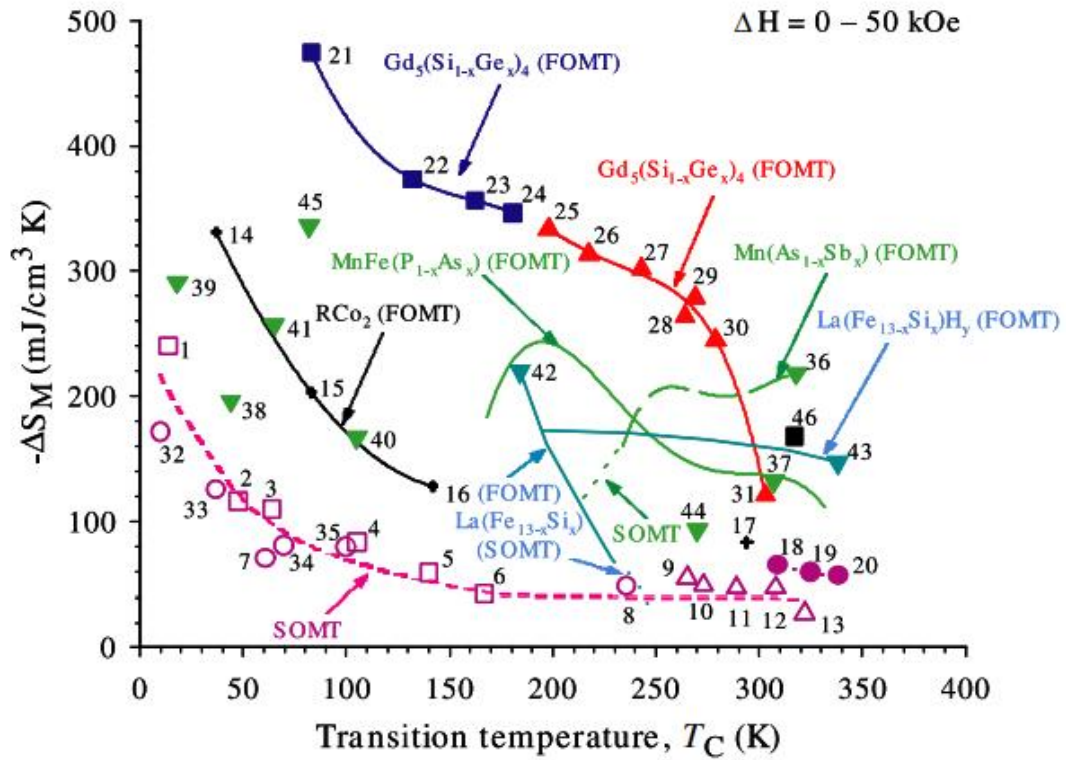
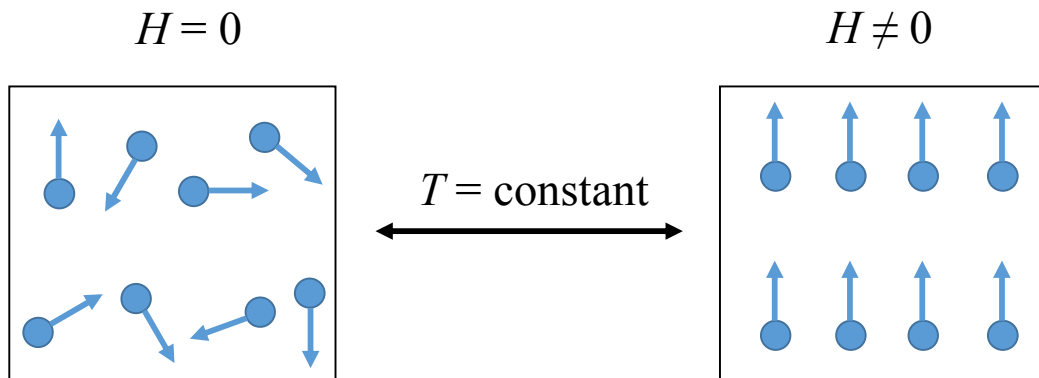


Figure 1.8: The magnetic entropy change for $H = 50 \text{ kOe}$ for the RCo_2 , RAl_2 , $\text{Gd}_5(\text{Si}_{1-x}\text{Ge}_x)_4$, $\text{Mn}(\text{As}_{1-x}\text{Sb}_x)$, $\text{MnFe}(\text{P}_{1-x}\text{As}_x)$ and $\text{La}(\text{Fe}_{13-x}\text{Si}_x)$ families plus a number of individual compounds versus the Curie temperature (From Ref. 84).

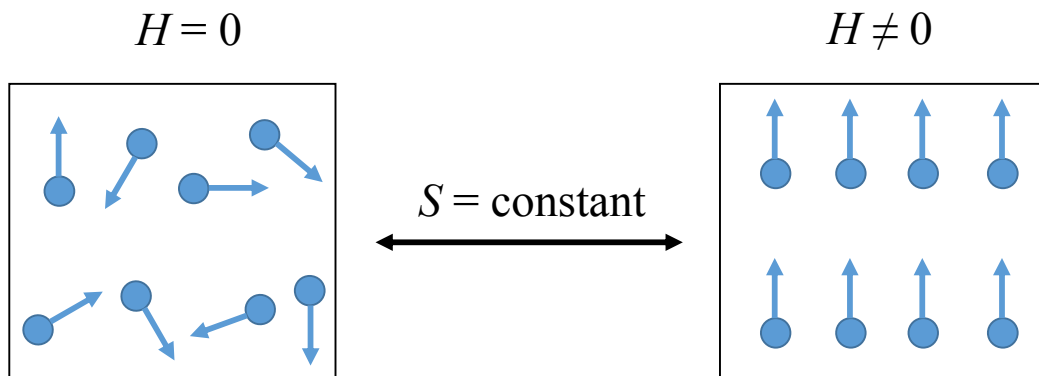
significant advantages such as higher energy efficiency and environmental safety over the conventional gas compression techniques.

The majority of the work among the notable research on magnetocaloric materials has been devoted to search for new materials for room temperature applications by studying their properties and feasibility of their production in an economic way. The magnetic entropy change for $H = 50$ kOe for the RCO_2 , RAl_2 , $\text{Gd}_5(\text{Si}_{1-x}\text{Ge}_x)_4$, $\text{Mn}(\text{As}_{1-x}\text{Sb}_x)$, $\text{MnFe}(\text{P}_{1-x}\text{As}_x)$ and $\text{La}(\text{Fe}_{13-x}\text{Si}_x)$ families plus a number of individual compounds versus the Curie temperature are shown in Fig. 1.8 (taken from Ref. 84). Upon looking at Fig. 1.8, it is evident that the value of $-\Delta S_M$ decreases while going from low temperature to room temperature [87]. It is also apparent that large values of $-\Delta S_M$ are reported for those compounds which consists first order magnetic transition (FOMT). Most of these compounds consist rare-earth metals either in pure or combined in alloys, for example, $\text{Gd}_5\text{Si}_2\text{Ge}_2$ [88]. The alloy that consist praseodymium and nickel (PrNi_5) has shown large MCE and has allowed to approach temperatures near absolute zero (to within one milliKelvin) [89]. In addition to the above mentioned compounds, RCO_2 based systems ($R = \text{Er}, \text{Ho}, \text{Dy}$) [90], $\text{Gd}_5\text{Si}_2\text{Ge}_2$ and $\text{Gd}_5(\text{Si}_{1-x}\text{Ge}_x)_4$ and related 5:4 materials [91] have shown significant MCE properties. $\text{La}(\text{Fe}_{13-x}\text{M}_x)$ -based compounds like $\text{La}(\text{Fe}_{1-x}\text{Co}_x)_{11.9}\text{Si}_{1.1}$ series, second order phase transition material, have been studied due the ease of its production on an industrial scale through powder metallurgical process and tunability of Curie temperature through the adjustment of Co content [92]. In addition, Mn-based compounds and $\text{MnAs}_{1-x}\text{Sb}_x$ series [93], many manganites such as $\text{La}_{1-x}\text{M}_x\text{MnO}_3$ (where $M = \text{Ca}$ and Sr) [84], and $\text{Fe}_{49}\text{Rh}_{51}$ [94] known to have the highest value of MCE near room temperature.

MCE is a magneto-thermal response (heating or cooling) of a magnetic material, when it is exposed to magnetic field adiabatically. Such phenomenon is analogous to the heating and cooling of a refrigerant gas in response to compression and expansion, which can be realized indirectly as a change in magnetic entropy (ΔS_M) [95-97, 88]. The MCE is an intrinsic characteristic of magnetic solids, which has



Isothermal process: $\Delta S_T = S(T, H) - S(T, 0) < 0$



Adiabatic process: $\Delta T_S = T(S, H) - T(S, 0) > 0$

Figure 1.9: Schematic representation of two thermodynamic processes of a magnetocaloric effect when a magnetic field is applied or removed for a magnetic system. During isothermal process, total entropy change is non zero and negative, while temperature change is non zero and positive during adiabatic process.

been discovered for the first time in 1881 in iron by Warburg [98]. The origin of MCE was explained independently by Debye [99] and Giauque [100].

A magnetic material with large change in magnetic entropy ΔS_M (T, H) or adiabatic temperature (ΔT) and a sufficiently large value of refrigeration capacity (RC) can be used as suitable candidate for magnetic refrigeration [101]. In the subsequent sections, we will present fundamental concepts of magnetocaloric effect.

1.8.1 Basic theory of magnetocaloric effect

The physical origin of MCE is attributed to the coupling between magnetic sublattice and the external magnetic field H. The spin system of a ferromagnetic (FM) or a paramagnetic (PM) materials can be influenced by the applied magnetic field, which changes the magnetic contribution to the entropy of the solid. The MCE can be realized through thermodynamical process, which relates the magnetic variables (magnetization and magnetic field) to the entropy and temperature.

As illustrated in Fig. 1.9, the application of external magnetic field to the magnetically disordered system in adiabatic condition align the magnetic moments in an ordered fashion, which substantially lowers the magnetic entropy. To maintain the total entropy constant, the entropy of the lattice system will increase in order to compensate the magnetic entropy reduction. This increase in lattice entropy leads to rise the temperature of the material. Therefore, the MCE of a substance is quantified by two parameters, isothermal entropy change, ΔS_T , and adiabatic temperature change, ΔT_S . The reduction of magnetic entropy and the rise of its temperature greatly occur near absolute 0 K for a PM materials, and near its magnetic ordering temperature (the Curie temperature, T_C) for a FM material.

The Maxwell's thermodynamic equation [102] which relates magnetic field H, magnetization M to the temperature T, and entropy S of a magnetic material is

$$\left(\frac{\partial S}{\partial H}\right)_T = -\left(\frac{\partial M}{\partial T}\right)_H \quad \dots\dots (1.20)$$

The change in magnetic entropy $\Delta S_M(T, H)$ for an adiabatic process can be calculated by integrating equation 1.20,

$$\Delta S_M(T, H) = S_M(T, H) - S_M(T, 0) = \int_0^H \left(\frac{\partial M(T, H)}{\partial T} \right)_H dH \quad \dots (1.21)$$

This equation indicates that the change in magnetic entropy is proportional to both the derivative of magnetization with respect to temperature at constant field and to the field variation. From the magnetization measurements at different magnetic fields and temperature intervals, the change in entropy can be calculated by

$$\Delta S_M(T, H) = \sum_i \frac{M_{i+1}(T_{i+1}, H) - M_i(T_i, H)}{T_{i+1} - T} \Delta H \quad \dots (1.22)$$

On the other hand, the change in entropy can be calculated from the magnetic field dependence of heat capacity C_H measurements by

$$\Delta S_M(T, H) = \int_0^H \frac{C(T, H) - C(T, 0)}{T} dT \quad \dots (1.23)$$

where $C(T, H)$ and $C(T, 0)$ represent the heat capacity values in the presence of a magnetic field H and absence of field ($H = 0$) respectively.

Using the following thermodynamic relation [102]:

$$\left(\frac{\partial T}{\partial H} \right)_S = - \left(\frac{\partial S}{\partial H} \right)_T \left(\frac{\partial T}{\partial S} \right)_H \quad \dots (1.24)$$

$$C_H = T \left(\frac{\partial S}{\partial T} \right)_H \quad \dots (1.25)$$

and using equation 1.20, the infinitesimal adiabatic temperature change can be obtained by the following expression

$$dT_{ad} = - \left(\frac{T}{C(T, H)} \right)_H \left(\frac{\partial M(T, H)}{\partial T} \right)_H dH \quad \dots (1.26)$$

After integrating this equation, one can obtain the expression that characterize the magnetocaloric effect,

$$\Delta T_{ad}(T, \Delta H) = - \int_0^H \left(\frac{T}{C(T, H)} \right)_H \left(\frac{\partial M(T, H)}{\partial T} \right)_H dH \quad \dots (1.27)$$

From the equation 1.21 and equation 1.27, it is clear that the large value of MCE (large value of ΔS_M and ΔT_{ad}) can be obtained with higher value of $\left(\frac{\partial M}{\partial T} \right)_H$ and smaller value of $C(T, H)$ at the same temperature.

1.9 Motivation and objectives

Perovskites with general formula ABO_3 (A is rare earth ion or Yttrium and B is a transition metal) have been the most versatile compounds in oxide research [16, 21, 26, 103]. Among perovskite oxides, rare earth orthoferrite ($RFeO_3$) compounds with distorted perovskite structure have drawn considerable attention due to their unique physical properties [34]. These compounds have been found potential applications such as ultrafast magneto-optical recording [104], laser-induced thermal spin reorientation [105], precession excitation induced by terahertz pulses [106], inertia-driven spin switching [107], and magnetism induced ferroelectric multiferroics [108].

It has been believed that variety of interesting properties can be achieved by applying chemical pressure with different kinds of cations at B-site of perovskite materials [109]. The only trivalent nature of elements in the structure of $RFeO_3$ and $RCrO_3$ compounds make them attractive for isovalent substitutions. The $RFe_{1-x}Cr_xO_3$ compounds with mixed Fe and Cr at B-site have shown superior physical properties compared to the end member $RFeO_3$ and $RCrO_3$ compounds. For example, complex magnetic behaviour has been reported on $Nd(Cr_{1-x}Fe_x)O_3$ [110] and $Y(Fe_{1-x}Cr_x)O_3$ [111] respectively. Temperature and magnetic field induced magnetization reversal and multiferroic behaviour have been observed in various compounds [112-114]. On top of that, large value of magnetic entropy ($-\Delta S_M \sim 29.2$

J/kg-K at 3 K with a magnetic field of 4.5 T) change has been reported on $\text{GdFe}_{0.5}\text{Cr}_{0.5}\text{O}_3$ [115] compound.

Among RFeO_3 compounds, holmium orthoferrite (HoFeO_3) has been the well-known studied perovskite compound for ultrafast recording applications [107]. The crystal structure of HoFeO_3 is orthorhombic with a space group of Pbnm at room temperature and possesses G-type antiferromagnetic with a magnetic ordering temperature (T_N) around 641 K [76]. Apart from T_N , HoFeO_3 exhibits the SR transition [76] of Fe^{3+} at 50 - 60 K with magnetic structure changing from $G_xA_yF_z$ (Γ_4) to $F_xC_yG_z$ (Γ_2), where G_x , A_y , and F_z stand for spin component along x-, y-, and z- axis in terms of Bertaut's notation [79], respectively. Few reports [116-117] have been shown that substitution with a rare earth element at Ho site and a transition metal element at Fe site led to a structural distortion and change in the magnetic properties of HoFeO_3 compounds.

The effect of Pr^{3+} doping at the Ho^{3+} site and Mn^{3+} at the Fe^{3+} site on the magnetic properties of HoFeO_3 compound has been studied in 2014 by Shujuan Yuan *et. al.* [116]. An increase in SR transition temperature (T_{SR}) from 50 K at $x = 0$ to 76 K at $x = 0.3$ has been observed in the case of $\text{Ho}_{1-x}\text{Pr}_x\text{FeO}_3$ compound. This change in T_{SR} has been attributed to the distortion of the crystal structure. On the other hand, a decrease in T_N has been observed in $\text{HoFe}_{1-x}\text{Mn}_x\text{O}_3$ compound, and the origin is ascribed to the weakening of Fe^{3+} - Fe^{3+} antiferromagnetic interaction by the replacement of Fe^{3+} ions with Mn^{3+} ions.

Influence of Ni substitution at Fe-site on morphological, optical and magnetic properties of HoFeO_3 compound has been studied in 2016 by Zubida Habib *et. al.* [117]. A decrease in band gap has been observed with an increase of Ni content, which explained on the basis of structural distortion. An increase in saturation magnetization and a decrease in coercive field has been evident with an increase of Ni content, and the same has been attributed to reduction of uncompensated spins.

According to Goodenough-Kanamori theory, Cr^{3+} is best choice for Fe^{3+} to show superior magnetic properties due to super exchange interaction [39, 41]. Hence, in

this thesis we explored the structural, magnetic properties and their correlation with lattice dynamics in $\text{HoFe}_{1-x}\text{Cr}_x\text{O}_3$ ($0 \leq x \leq 1$) compounds.

1.9.1 Band gap tuning and orbital mediated electron-phonon coupling

It has been believed that in the cubic perovskites, due to the distortion of the lattice, symmetry of structure lowers and this leads to the appearance of the Raman-active phonons [118]. The influence of the electronic configuration and orbital ordering on the Raman spectra of these distorted perovskites has been addressed by Allen *et. al.* [119]. Local oxygen breathing mode through an orbital mediated electron-phonon coupling has been observed in the Raman spectrum of the distorted perovskite compound based on the mixed Fe and Cr ions at B – site. Such intriguing phenomenon has been explained on the basis of the Franck-Condon picture following a photon induced transfer of an electron from Fe to adjacent Cr ion [120]. Similar behaviour has been observed on the other compound $\text{La}_{1-y}\text{Sr}_y\text{Mn}_{1-x}\text{M}_x\text{O}_3$ ($\text{M} = \text{Cr}, \text{Co}, \text{Cu}, \text{Zn}, \text{Sc}$ or Ga) [121]. Electron – lattice dynamics are very important in the rare earth-transition metal oxides to understand the phenomenon of colossal magnetoresistance [16]. On the other hand, exploring the correlation between the structural, magnetic and orbital ordering is very much essential to understand the charge transfer mechanism which is base for the electron – phonon coupling. To our knowledge, until now the electron - phonon coupling has been observed only in the Jahn – Teller active compounds. However, it would be very interesting if we can observe electron - phonon coupling in the Jahn – Teller inactive compound. For this purpose we choose the HoFeO_3 which is a Jahn – Teller inactive, which may become Jahn – Teller active by substituting Cr. We anticipate that electron transfer mechanism can takes place from Fe site to the Cr site when an incident photon energy equals to the ground state energy gap between Fe^{3+} and Cr^{3+} . Hence, one of our aims is to understand the electron-phonon coupling which may leads to charge transfer between Fe^{3+} and Cr^{3+} through Raman spectroscopy.

RFeO_3 and RCrO_3 compounds have been believed to possess p – type semiconducting behaviour [122], which may be very much useful in developing the

optoelectronic devices. *However, to the best of our knowledge, detailed information on band gap values is not available in the literature neither on HoFeO₃ nor on HoCrO₃. In addition, it would also be of great interest to monitor the change in the band gap value by applying the chemical pressure either at Fe site or Cr site. To achieve our goal, in the present work, Cr is chosen to apply the chemical pressure at Fe-site of HoFeO₃ compound.*

1.9.2 Magnetic and magnetocaloric properties

RFeO₃ compounds have the complex spin structure between the rare earth (R) and the transition metal (TM) ions [34], which makes them of great interest to study their magnetic properties. Indeed the canted antiferromagnetism, Dzyaloshinsky – Moriya exchange interaction [123, 47], very small anisotropy of Fe spins in a – c plane and large anisotropy along b – axis [124] may play vital role in determining RFeO₃ magnetic properties. The Fe³⁺ magnetic moments in RFeO₃ compounds order antiferromagnetically (AFM) and consists canted nature with respect to the AFM axis at a temperature T_N ranging from 620 - 750 K. This canting nature produces weak ferromagnetic (FM) moment in the direction perpendicular to the AFM axis. The spontaneous magnetic moment of RFeO₃ compounds at room temperature is around 100 Oe, which is very small [125]. Controlling the magnetic ordering temperatures and enhancement of magnetic properties in these compounds would be helpful in magnetic storage device applications. One of the characteristic magnetic transition of RFeO₃ is spin reorientation (SR) during which the direction of easy axis of magnetization of Fe³⁺ sub lattice changes from one crystal axis to another upon varying the temperature [126]. At low temperatures, the ordering of rare earth (R³⁺) moments leads to dominate the R³⁺-Fe³⁺ interaction over Fe³⁺-Fe³⁺ interaction. This causes a SR transition to occur below T_N in RFeO₃ compounds. Controlling the orientation of these spins can therefore lead to drastic changes in magnetic properties and offer unique functionality and potential applications in future spintronic devices.

On top of that oxidation state of Fe influences the magnetic properties of these orthoferrites. Mössbauer spectroscopy [127] is an important microscopic technique

to determine local interactions via hyperfine interaction, i.e. the interactions between the nuclear charge distribution and extra nuclear electric and magnetic fields. These hyperfine interactions [127] give rise to isomer shift (IS), the quadrupole splitting (QS) and the magnetic Zeeman splitting. *Hence, in the present work, we put our efforts in exploring the magnetic and local interactions in $\text{HoFe}_{1-x}\text{Cr}_x\text{O}_3$ ($0 \leq x \leq 1$) compounds through magnetization measurements and Mössbauer spectroscopy.*

RFeO_3 and RCrO_3 compounds have been explored for their MCE properties and suitability of them for magnetic refrigeration applications [114, 128-129]. For example, a large MCE value of $-\Delta S_M \sim 8.4$ J/kg-K and $\text{RC} \sim 217$ J/kg at 15 K and 4 T has been observed in DyCrO_3 due to ordering of Dy^{3+} at 2.3 K [129]. Yin *et.al*, have reported large MCE value of $-\Delta S_M \sim 10.5$ J/kg-K at 4 T around Dy^{3+} ordering (14 K) in $\text{DyFe}_{0.5}\text{Cr}_{0.5}\text{O}_3$ compound [114]. Although several reports have shown MCE on various magnetic materials, as this field is highly demanding numerous new materials need to be explored for MCE applications. Particularly, much attention is required to search for new materials with giant MCE below 30 K for the utilization in space applications. *Hence, it is important to explore magnetocaloric properties and nature of magnetic transition in $\text{HoFe}_{1-x}\text{Cr}_x\text{O}_3$ ($0 \leq x \leq 1$) compounds.*

1.9.3 Spin – phonon coupling

The discovery of the multiferroic materials, has allowed tuning the ferroelectric state (FE) with magnetic field and (anti) ferromagnetic state with electric field as there exists a strong coupling between various states [130-131]. These materials have been found applications in various technological devices such as magneto-electronic [130] and memory devices [131]. Since there has been much demand for these exotic materials, there is a quest for developing new materials which can exhibit aforesaid properties near room temperature.

Multiferroic properties have been reported on BiFeO_3 [132] and BiCrO_3 [133] compounds, and the origin of which in the former have been attributed to the

presence of stereo-chemically active lone electron pair of Bi^{3+} ion [132] and are under intense debate for the latter. In addition, a structural phase transition from a monoclinic structure with a space group of $C2/c$ to an orthorhombic structure with a space group of $Pnma$ has been observed in BiCrO_3 compound above 420 K through temperature dependent Raman spectroscopy studies [133].

Apart from the above, RMO_3 ($R = \text{Ho, Gd, etc.}, M = \text{Cr, Fe, Mn}$) compounds have extensively been investigated for the multiferroic properties [134-136]. Improper ferroelectricity has been observed in rare earth orthochromites, RCrO_3 around the magnetic ordering temperature of Cr^{3+} moments and its origin has been ascribed to the interaction between R^{3+} and Cr^{3+} moments [137]. Atypical multiferroic behaviour in HoCrO_3 compound has been reported by Ghosh *et.al.*, [138] and the origin of ferroelectricity has been explained on the basis of probable displacement of Ho^{3+} ion and rotation of the oxygen octahedra in the non-centrosymmetric $Pna2_1$ space group. Contrary to this, the temperature dependent structural properties on HoCrO_3 compound have been investigated by X-ray and neutron diffraction and have shown no signature of structural phase transition below T_N [139]. However, local structural change (which may lead to multiferroicity) through spin-phonon coupling has been demonstrated in RCrO_3 ($R = \text{Y, Lu, Gd, Eu and Sm}$) compounds using temperature dependent Raman spectroscopy [136].

Recently, it has been reported that the role of spin-phonon coupling in stabilizing the ferroelectric ordering in rare earth chromites/ferrites/manganites (RMO_3 with $M = \text{Cr, Fe, Mn}$) [134-136]. Ferreira *et. al.*, have been reported on the correlation between spin-phonon coupling and multiferroicity in GdMnO_3 [134]. Signature of spin-phonon coupling which may lead to structural rearrangements in GdFeO_3 compound has been demonstrated by Anjali *et.al.*[135]. Yet in another study, crucial role of spin-phonon coupling in inducing FE ordering in GdCrO_3 compound has been well manifested by Bhadram *et. al.*[136].

On the other hand, in the doped compound $\text{DyFe}_{0.5}\text{Cr}_{0.5}\text{O}_3$, origin of ferroelectricity has been correlated to the displacement of Dy^{3+} ions and stretching of oxygen octahedral [114]. Therefore, there has been an intense debate whether, the spin – phonon coupling leads to structural change in HoCrO_3 compound. *Hence, in the present investigation we performed temperature dependent Raman spectroscopy in order to explore the coupling that exists between spin and phonon modes, which may lead to local structural change in $\text{HoCr}_{1-x}\text{Fe}_x\text{O}_3$ ($x = 0$ and 0.5) compounds.*

Chapter 2

Experimental Techniques

In this chapter we discuss about various experimental techniques that we used to prepare $\text{HoFe}_{1-x}\text{Cr}_x\text{O}_3$ ($0 \leq x \leq 1$) compounds and to characterize them. $\text{HoFe}_{1-x}\text{Cr}_x\text{O}_3$ ($0 \leq x \leq 1$) compounds were prepared using conventional solid state reaction route. Structural characterization of as prepared compounds was carried out using powder x-ray diffraction (XRD) and Raman spectroscopy studies. Optical properties were studied using UV-Vis-NIR spectroscopy. Change in local atomic and electronic structure around the nuclei was studied using ^{57}Fe Mössbauer spectroscopy. Magnetic measurements were carried out using vibrating sample magnetometer (VSM) and magnetic property measurement system (MPMS). Specific heat studies were carried out using a physical property measurement system (PPMS). In the subsequent sections, we discuss about principles of various experimental methods that we used in detailed way.

2.1 Solid state reaction method

Solid state diffusion is one of the most widely used methods to prepare complex oxides using microcrystalline precursor powders [140]. This process involves neither a solvent medium nor controlled vapour-phase interactions. The rate of diffusion would happen at high temperatures ($1000 - 1500^\circ \text{C}$) and completely depends on the inter-diffusion. In addition, the rate of diffusion would also depends on the ambient atmosphere, structural properties of the starting materials, their surface area, reactivity, and the change in the thermodynamic free energy associated with the reaction. Solid state reaction method mainly involves the grinding starting powders and sintering at higher temperatures to achieve a phase pure ceramic powders compounds with high density.

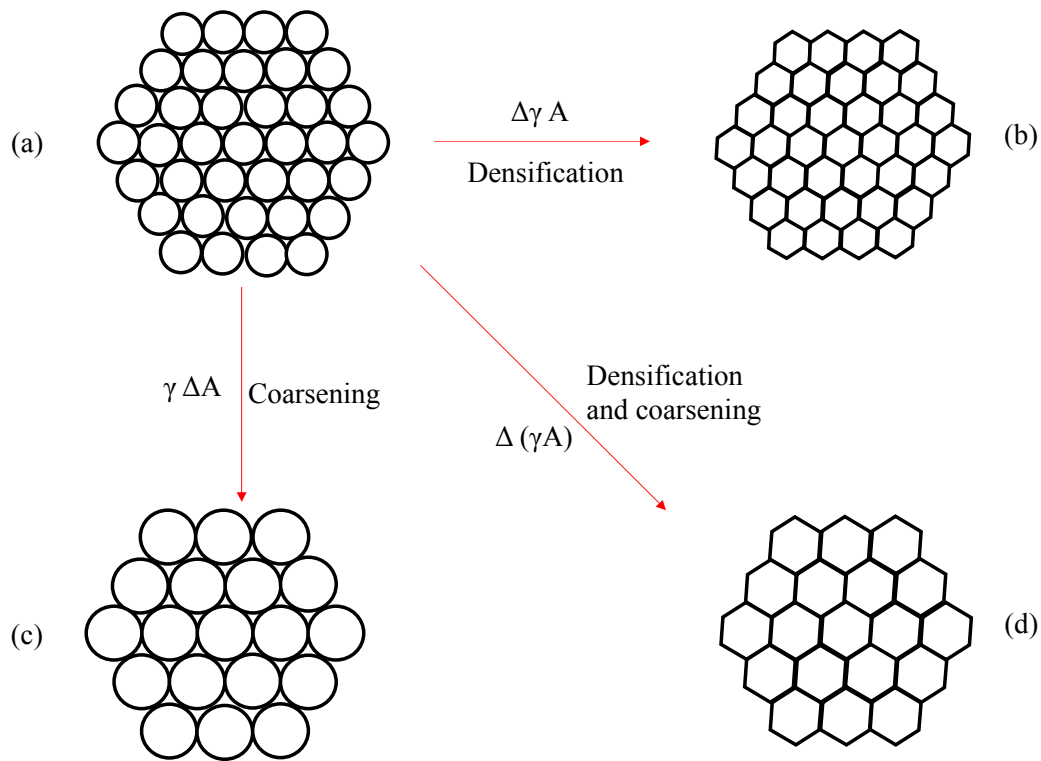


Figure 2.1: Schematic representation of different stages of sintering process [141]. Fig. 2.1 (a) denotes the particles of the compound before the process of heat treatment. The process of densification and Coarsening is shown in Fig. 2. 1 (b) and Fig. 2.2 (c) respectively. Fig. 2.1 (d) represents the particles of the compound after sintering.

In general, polycrystalline compounds can be prepared either by solid state or sol-gel routes. As it would be difficult to achieve inter diffusion at room temperature, heating of the powder mixture (which consists constituent elements) is mandatory to overcome the kinetic barriers and to get single phase compounds. It is very much important to have good reaction interface between the particles, which can be achieved by making powders in pellet form before heat treatment. This heat treatment process can be called as sintering.

The driving force for sintering is the reduction in surface free energy (interfacial free energy) of the consolidated mass of particles. The total surface free energy of the compact powder is expressed as γA where γ represents the specific surface energy and A denotes the total surface area of the compact powder. The change in the total surface free energy can be written as [141]

$$\Delta(\gamma A) = A\Delta\gamma + \gamma\Delta A \quad \dots\dots (2.1)$$

where $\Delta\gamma$ represents the reduction of surface energy due to the densification (by transport matter from inside the grains into the pores) and the reduction of the area (ΔA) is due to the expansion of grain size (Coarsening). Essentially, in the solid state route, the replacement of solid-vapour interface by solid-solid interface gives the reduction of the interfacial energy. The schematic diagram of the sintering process is shown in Fig. 2.1. Figure 2.1 (a) represents the particles of the compound before sintering. The process of densification is shown in Fig. 2.1 (b) while Coarsening is shown in Fig. 2.1 (c). The particles of the compound after sintering is shown in Fig. 2.1 (d).

In the present study, polycrystalline compounds of $\text{HoFe}_{1-x}\text{Cr}_x\text{O}_3$ ($0 \leq x \leq 1$) were prepared by the conventional solid state reaction method. High purity oxide powders of Ho_2O_3 , Fe_2O_3 , and Cr_2O_3 (purity > 99.9%) (Sigma-Aldrich chemicals India) were used as starting raw materials and were mixed together in stoichiometric ratios. The mixture thus obtained was thoroughly and repeatedly ground in the isopropanol alcohol using an agate mortar and pestle to ensure the

homogeneity. Pellets were prepared using the resultant powder and sintered sequentially at 1000° C for 12 h, 1200° C for 12 h and 1250° C for 24 h respectively.

2.2 X-ray diffraction (XRD)

To reveal the crystallographic structure and phase purity of the prepared compounds, a non-destructive analytical technique, x-ray diffraction (XRD) was used [142-143]. XRD is one of the X-ray scattering technique based on constructive interference due to the diffraction of X-rays by crystal lattice. The powder x-ray diffraction works based on the principle of Bragg's Law, which is shown in Fig. 2.1.

According Bragg's law, the interaction of the incident rays with the compound produces constructive interference pattern only if the path difference between the two rays is an integral multiple of the wavelength. This law relates the wavelength of electromagnetic radiation (λ) to the diffraction angle (θ), and the lattice spacing (d_{hkl}) in a crystalline sample as follows:

$$n \lambda = 2d_{hkl} \sin\theta \quad (\text{Bragg's law}) \quad \dots\dots (2.2)$$

where $n \geq 0$ is an integer. The condition for Bragg's law to satisfy is $\lambda \leq 2d_{hkl}$ since $\sin\theta \leq 1$ at all the time.

In the present thesis, the diffraction pattern with peaks corresponding to the different planar distances were obtained using $\theta - 2\theta$ scanning mode. In this particular scanning mode, x - ray source was fixed whereas the sample was rotated about an axis that was normal to the plane containing the x-ray beam and the detector. The rotation of the detector was twice compared to that of the sample rotation, and the strongest signal was obtained for zeroth order ($n = 1$) diffraction.

In general, from a diffraction pattern, one can get information about peak position and intensity. From the position of diffraction peak, one can determine the crystal structure and symmetry of the contributing phase. On the other hand, the intensity determines the total scattering from each of the plane.

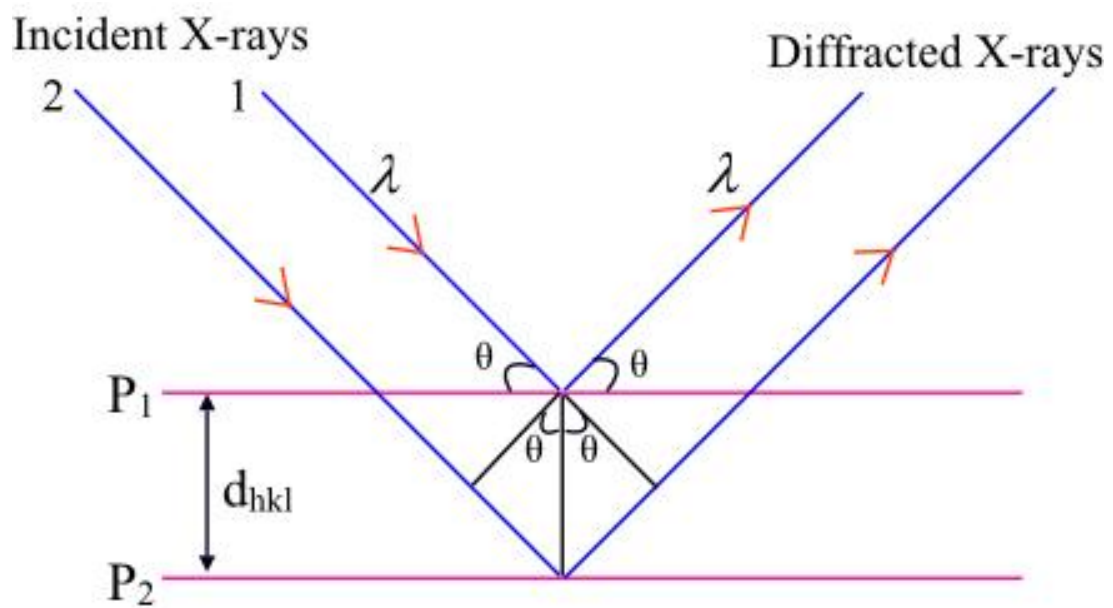


Figure 2.2: Schematic diagram of x-ray diffraction pattern (XRD). P_1 and P_2 corresponds to different planes.

In case of the powder diffraction, the intensity of scattered x - rays can be expressed as

$$I_{(hkl)} = K \frac{1 + \cos^2 2\theta}{4 \sin^2 \theta \cos \theta} |F_{(hkl)}|^2 \quad \dots (2.3)$$

where $I_{(hkl)}$ denotes the intensity of reflection from (h k l) plane, and $F_{(hkl)}$ represents the structure factor for the reflection (h k l), which can be written as

$$F_{(hkl)} = \sum_i f_i \exp[2\pi j(hx_i + ky_i + lz_i)] \quad \dots (2.4)$$

where x_i, y_i, z_i are the coordinates of i^{th} atom, f_i is the atomic scattering factor.

2.2.1 Rietveld refinement

Rietveld refinement has been a most accurate method to determine the structural parameters of the compound accurately [144]. From this, the structural information can be obtained by fitting experimental data with theoretical model using least square method. Essentially, in this least square method, number of parameters such as position of the atoms, thermal parameters, occupancy of the atoms, instrumental parameters and peak shape parameters would be adjusted to get a best fit between the theoretical and experimental diffraction pattern.

In the present thesis, we have refined the powder XRD patterns of $\text{HoFe}_{1-x}\text{Cr}_x\text{O}_3$ ($0 \leq x \leq 1$) compounds using General Structural Analysis System (GSAS) software. Initially, we have refined the background and peak shape using a polynomial function and pseudo-Voigt function respectively. During the refinement, the lattice parameters, half width parameters, scaling factors and the coefficients of background polynomial were mainly varied. In addition to the above mentioned global parameters, fractional atomic co-ordinates, isotropic displacement (temperature) parameter and occupancy (chemical occupancy normalized to the multiplicity of the general position of the group) values were also refined. The values of chemical occupancy for holmium (Ho) and oxygen (O) was taken as '1' during the refinement.

The quality of the refinement is evaluated based on the values of reliability factors such as R_p , R_{wp} , and χ^2 , which have been defined as below [145].

$$\text{Profile factor, } R_p = 100 \times \left[\frac{\sum_{i=1,n} |y_i - y_{c,i}|}{\sum_{i=1,n} y_i} \right] \quad \dots (2.5)$$

Here y_i and $y_{c,i}$ represents the observed point (experimental) and the calculated point respectively whereas ‘n’ denotes the number of data points.

$$\text{Weighted profile factor, } R_{wp} = 100 \times \left[\frac{\sum_{i=1,n} \omega_i |y_i - y_{c,i}|^2}{\sum_{i=1,n} \omega_i y_i^2} \right]^{1/2} \quad \dots (2.6)$$

Here, $\omega_i = \frac{1}{\sigma_i^2}$, σ_i^2 is the variance for the observation, y_i .

$$\text{Expected weight factor, } R_{exp} = 100 \times \left[\frac{n - p}{\sum_{i=1,n} \omega_i y_i^2} \right]^{1/2} \quad \dots (2.7)$$

Here, $(n - p)$ represents the number of degrees of freedom. The total number of experimental points and the number of refined parameters are denoted by n and p respectively.

$$\text{Reduced chi-square, } \chi^2 = \left[\frac{R_{wp}}{R_{exp}} \right]^2 \quad \dots (2.8)$$

2.3 Raman spectroscopy

Raman spectroscopy is a scattering phenomenon, which works based on inelastic scattering of the monochromatic light incident on a compound, usually from a laser source [146]. This phenomenon was discovered in 1928 by Sir Chandrasekhara Venkata Raman, using sunlight as a source, telescope as a collector and his eyes as a detector. Raman measurement is an important technique used for chemical

identification and characterization of molecular structures. When the light incident on a compound, it may be reflected, absorbed, or scattered. By analysing the scattered light from the compound, one can get the information about the chemical and structural information.

During the measurement, the electric field of monochromatic light incident on the compound excites the molecule to higher energy states (virtual excited states). On the other hand, while coming back to its initial vibration state (ground state), a photon would be released with three different frequencies as follows:

1. Rayleigh scattering: The frequency of the emitted photon would be same as the incident radiation.
2. Stokes Raman scattering: The frequency of the emitted photon is lesser than that of incident radiation.
3. Anti-Stokes Raman scattering: The frequency of the emitted photon is higher than that of incident radiation.

The situation is schematically shown in Fig. 2.3. Essentially, in a molecular system, these frequencies would lie in the ranges associated with rotational, vibrational, and electronic level transitions. The scattered radiation usually consists polarization characteristics different from those of the incident radiation. The scattering occurs over all directions and both the intensity and polarization of the scattered radiation depend on the direction of observation. Through Raman spectroscopy one can obtain structural information such as bond vibrations or various modes that would arise due to structural distortion in the compound.

In the present thesis, Raman spectra was recorded at room temperature using a Laser Micro Raman spectrometer (Bruker, Senterra) with an excitation source of 532 nm and with a power of 10 mW. Temperature dependent Raman spectra were recorded with a LabRam-HR800 micro Raman spectrometer equipped with a Peltier cooled charge-coupled device detector, and an Ar⁺ ion laser excitation source with a wavelength of 488 nm. The overall spectral resolution is 1 cm⁻¹.

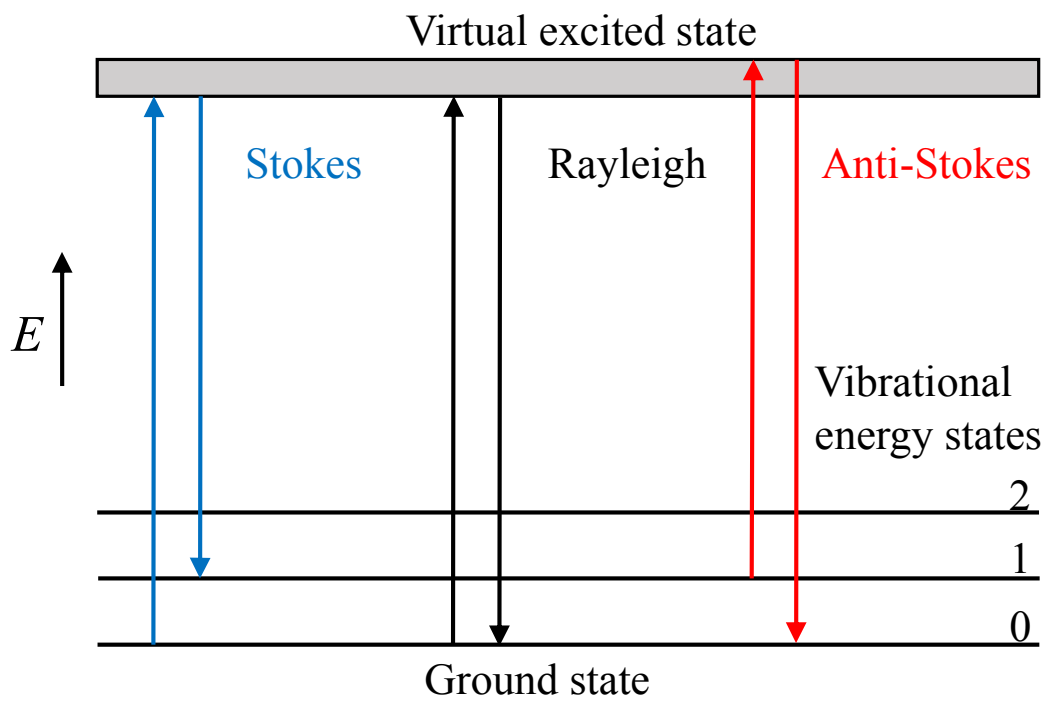


Figure 2.3: Schematic of the energy level diagram of the Raman scattering.

2.4 UV-Vis-NIR spectrophotometer

UV-Vis-NIR spectrophotometer is a spectroscopic instrument to measure the intensity of absorbance of light in the ultra-violet (200 - 400 nm), visible (400 - 800 nm) and near infrared regions (800 - 3300 nm) by the compound. Apart from the absorbance, it can also measure reflectance and transmittance of the light as a function of wavelength. Essentially, when the light (UV-Vis-NIR region) falls on the compound, light would be absorbed by molecule and there would indeed be electronic transitions to higher energy states. This technique can be used to absorbance spectra of various compounds/solutions of transition metal ions and highly conjugated organic compounds. This instrument works on Beers-Lamberts law, given by

$$A = \log \frac{I_0}{I} = \varepsilon * C * l \quad \text{..... (2.9)}$$

where A is the absorbance, I_0 is the intensity of the incident light falling on the sample, I is the intensity of the light leaving from the sample cell, ε is the molar absorptivity, C is the concentration of solution and l is the length of the sample cell.

One of the important applications of the spectrophotometer is the measurement of the optical band gap of various compounds. Band gap is defined as the energy difference between the bottom of the conduction and the top of the valence band. The energy that is required to excite an electron from the valence band to the conduction band is called the band gap energy. Band gap measurement is useful to identify whether a particular material is an insulator or semiconductor.

The band gap of a material can be determined using the Tauc's equation [147], which relates the optical absorption coefficient (α), photon energy ($h\nu$), and the energy gap E_g as given below

$$\alpha h\nu = (h\nu - E_g)^{1/2} \quad \text{..... (2.10)}$$

The value of E_g can be obtained using the above equation and by extrapolating the linear region of $h\nu$ vs. $(ah\nu)^2$ graph to x – axis.

In the present thesis, optical absorbance of the samples was measured at room temperature using Perkin Elmer Lambda 1050 UV-Vis-NIR spectrophotometer in the wavelength range of 200 - 800 nm.

2.5 Mössbauer spectroscopy

Mössbauer spectroscopy has been a resourceful spectroscopic technique based on nuclear resonant gamma (γ) ray scattering known as Mössbauer effect [148]. This technique provides information about electronic, magnetic and structural properties within the compound. Using this technique, one can probe the hyperfine transitions between the excited and ground states of the nucleus using the combination of Mössbauer Effect and Doppler shift. Mössbauer spectroscopy process involves the emission of a γ - ray by one nucleus, followed by the absorption of this γ - ray by a second nucleus, which becomes excited. “Mössbauer Effect” was first observed in 1957 by Rudolph Mössbauer, and received the Nobel Prize in Physics in 1961 for his work. The principle of this technique is illustrated in Fig. 2.4.

Firstly, a source containing ^{57}Co provides an excited ^{57}Fe by means of a decay of ^{57}Co into an excited ^{57}Fe with $I = 5/2$ state. Subsequently, there would be a rapid decay to $I = 3/2$ state and then to $I = 1/2$ ground state. This decay process releases a photon with an energy of 14.4 keV (γ - ray). This γ - ray will excite a transition in the sample under study, only if the energy gap is equal to 14.4 keV (frequency of $\nu = 3.5 \times 10^{18}$ Hz). This process is known as resonant absorption. Essentially, in the case of γ - ray, emission from one nucleus and a resonant absorption of the same by second nucleus does not usually take place due to relatively large momentum associated with recoil energy of the nucleus. During the measurement, the source containing ^{57}Co moves at a constant speed v relative to the sample which contain ^{57}Fe nuclei. By moving the ^{57}Co source, one can slightly vary the frequency of γ - ray to achieve a resonant absorption as a result of the Doppler effect. This recoil-free emission and resonant absorption of γ - ray are

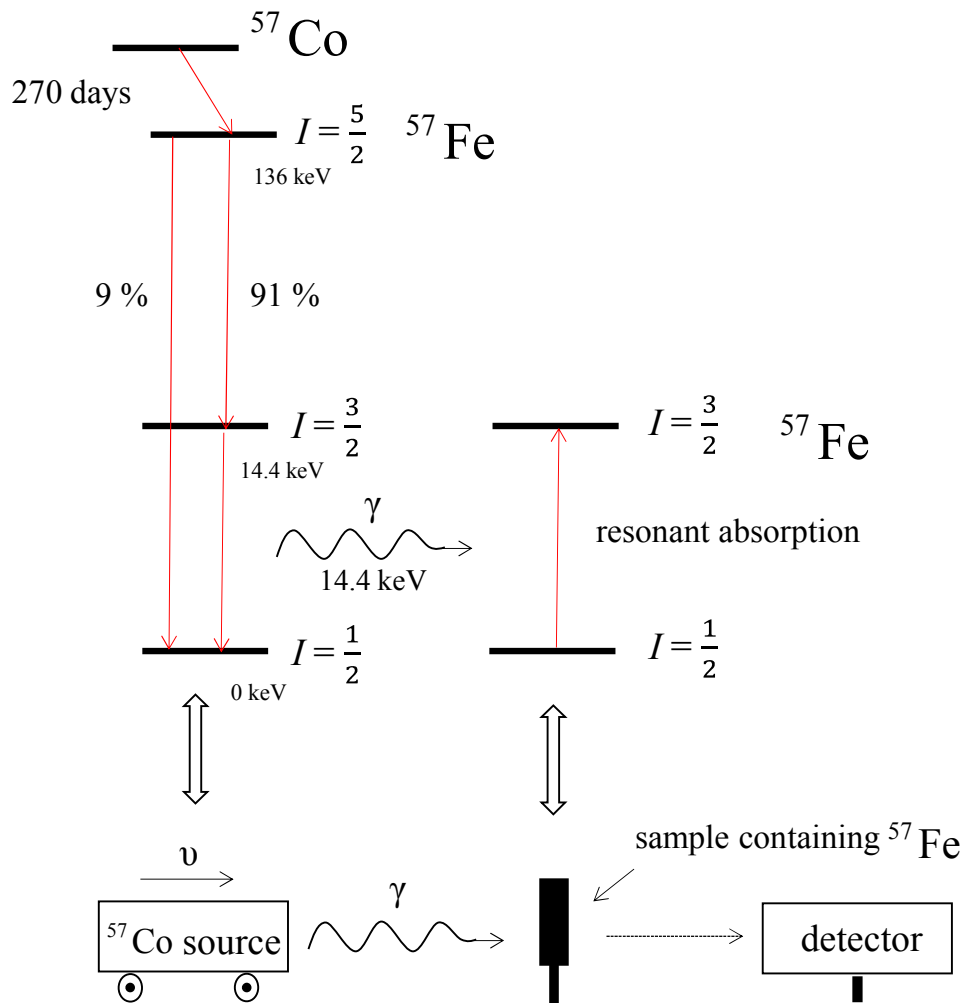


Figure 2.4: Schematic illustration of the principles of Mössbauer technique. ^{57}Co decays slowly into an excited state of the ^{57}Fe nucleus. As it is evident, 91% of the decay is rapid to $I = 3/2$ state which then decays to $I = 1/2$ ground state. This decay releases a 14.4 keV photon. The experiment was performed by moving the ^{57}Co source at a speed v relative to the sample which contain some ^{57}Fe nuclei. The detector measures the transmission of γ -rays through the sample which can be used to deduce the absorption.

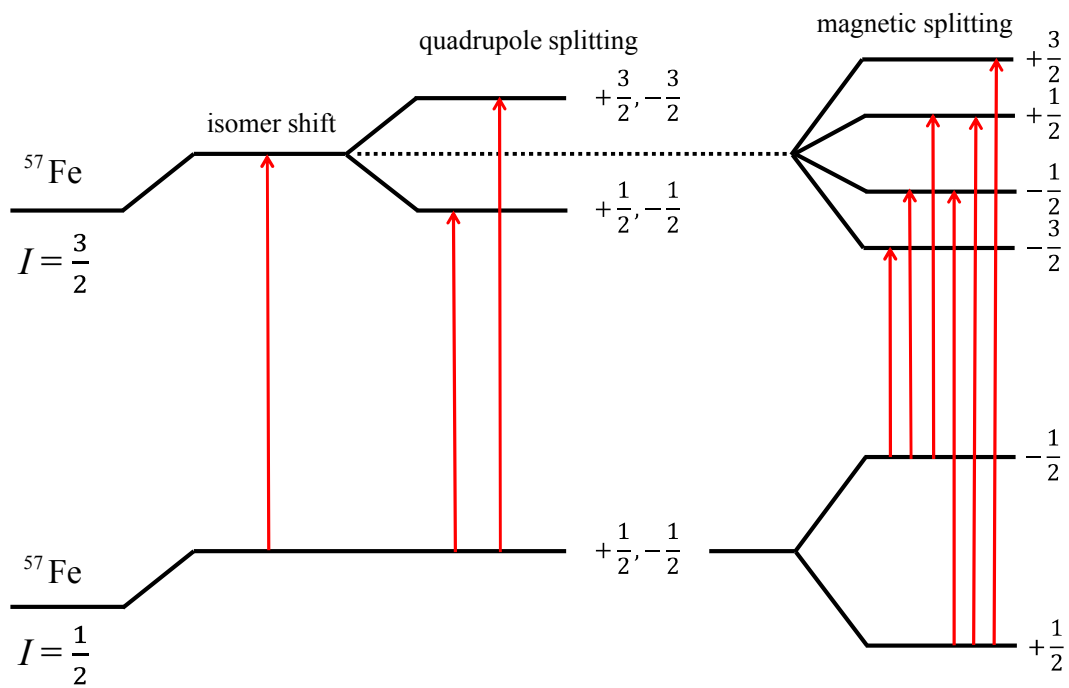


Figure 2.5: The effect of chemical shift, quadrupole splitting and magnetic splitting on the nuclear energy levels of ^{57}Fe .

principles of the Mössbauer effect. The detector measures the transmission of γ - ray through the compound which can be used to deduce the absorption.

The resonant absorption of γ - ray by the second nucleus may not occur when the source is stationary, however, it may occur when the source is moving at a particular velocity. This change in the velocity can be quantified using isomer shift arises due to slight change in the coulomb interaction between the nuclear and electric charge distributions which are associated with change in size of ^{57}Fe nucleus in $I = 3/2$ state and $I = 1/2$ state. Furthermore, it is not necessary to observe only one resonant line as a function of source velocity, but perhaps a number of lines. This can be due to quadrupole splitting or magnetic splitting. The first effect is due to the electric quadrupole moment of the excited ^{57}Fe nucleus (the ground state with $I = 1/2$ of ^{57}Fe has no electric quadrupole moment), when the nucleus is subjected to an electric field gradient, which leads to splitting of $I = 3/2$ state into a doublet. On the other hand, the second effect is due to the local magnetic fields. All these shifts and splittings are illustrated schematically in Fig. 2.5.

The recorded Mössbauer spectra were analyzed with NORMOS-DIST/SITE program for the estimation of hyperfine parameters.

2.6 Magnetization measurement techniques

2.6.1 Vibrating sample magnetometer (VSM)

Vibrating sample magnetometer (VSM) is a versatile and very sensitive technique, which has been using widely to measure the magnetic properties of variety of magnetic materials. VSM is referred to as Foner magnetometer which has originally developed by S. Foner [149]. This instrument works based on Faraday's law of electromagnetic induction. When a magnetic material is placed in a DC magnetic field and is simultaneously subjected to sinusoidal motion in a direction perpendicular to the field, the oscillatory flux due to the induced magnetic moments in the sample induce an e.m.f in a coil kept in the vicinity of the compound. This e.m.f is a measure of the magnetic moment of the compound. Using this instrument one can detect the magnetization of the sample (powder, thin film or single crystal)

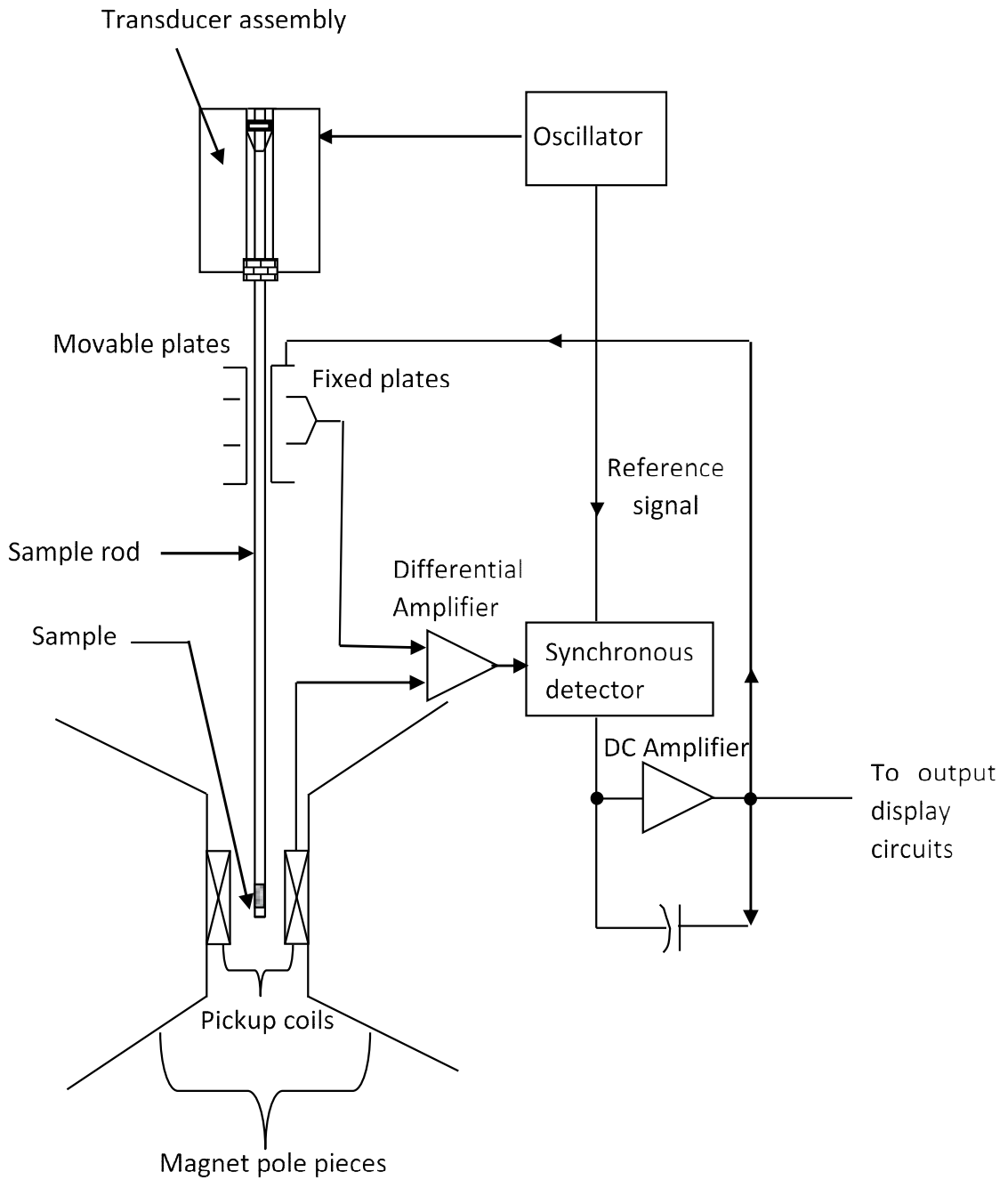


Figure 2.6: Schematic diagram of vibrating sample magnetometer (VSM).

which vibrates in a uniform magnetic field. This instrument allows to measure magnetization in a precise way as a function of temperature, magnetic field strength and crystallographic orientation. VSM can be used for both weak and strong magnetic substances with a sensitivity of about 10^{-5} emu.

The schematic diagram of the VSM is shown in Fig. 2.6. The main part is a vibrating head, which consists of a transducer assembly. The sample was attached to the bottom of a sample holder, which consists of three parts. The top part is a brass tube, whose top end can be attached to the transducer assembly. A detachable quartz rod, which can be attached to the bottom of the brass tube, is the second part. The third part is the sample container, which is attached to the bottom end of the quartz rod. The sample was made to vibrate in the vertical direction whereas the dc magnetic field was applied in the horizontal direction.

When sample was placed in an uniform magnetic field, a magnetic moment was induced. The induced magnetic moment was measured in the following way. The vibrating head makes the sample to vibrate at a fixed frequency. This vibration generates an alternating electromotive force (e.m.f) in the pickup coils, whose magnitude is not only proportional to the magnetic moment of the sample but also to the amplitude and the frequency of vibrations. This electrical signal (e.m.f) is detected and using a differential amplifier. In order to separate the contribution to the pick-up voltage from the magnetic moment, the pick-up voltage is fed to one of the inputs of a differential amplifier. The other input to the differential amplifier is the voltage output from a parallel-plate capacitor, one set of the plates of which is attached to the vibrating part of the transducer assembly, the other set being immovable. The output signal of the differential amplifier – thus proportional to magnetic moment of the sample and was comparable with a reference signal taken from the same oscillator, which essentially used to energize the transducer drive using a synchronous detector. A dc signal proportional to the magnetic moment of the sample was produced at the output of the detector. This signal was then amplified and two outputs are taken. One output was used to provide the feedback to the moving plate of the capacitor so that the capacitor output level is

always maintained equal to the pick-up coil signal amplitude. The second output was applied to the output display circuits so as to read the magnetic moment directly in electromagnetic units. A cylindrical piece of Ni of known mass was used as the standard sample for calibrating the VSM.

2.6.2 Magnetic property measurement system (MPMS)

Magnetic property measurement system (MPMS) (Quantum Design) is an advanced Superconducting Quantum Interference Device (SQUID) magnetometer used for the effective and sensitive measurement of the magnetic moments of small samples over a wide range of temperatures and magnetic fields. The SQUID magnetometer works based on the tunnelling of superconducting electrons across a Josephson junction (junction of two superconductors separated by an insulating gap) [150]. The central element of SQUID is a superconducting ring with one or more Josephson Junctions. The schematic illustration of the SQUID is shown in Fig. 2.7. The superconducting measuring current that flows through the ring can be divided in two and equal currents pass through each of Josephson junction. According of Faraday's law, a changing magnetic flux through the ring generates a voltage and a current in the ring. The interference concept is used in the SQUID, which is basically the modulation of the supercurrent by an applied magnetic field passing through the loop. This occurs because the magnetic field changes the phases of the wave functions across the junctions, and hence the current through them. The flux through the loop is modulated by a 100 kHz flux from the feedback coil with a magnitude less than ϕ_0 . The lock-in amplifier amplifies the difference between the SQUID loop's signal and the 100 kHz signal and this is fed back to the feedback coil. The feedback loop adjusts until the feedback flux cancels the input flux. This can be seen by considering how the system would respond if the feedback flux does not cancel the input flux. In this case, the voltage across the SQUID loop will be modulated and the feedback will be increased until it does cancel. Fractions of a flux quantum can be measured by the feedback flux.

Schematic diagram of SQUID magnetometer in MPMS is shown in Fig. 2.8 [151]. In the SQUID, the detection coil (pick-up coil) consists a set of three coils. Among the

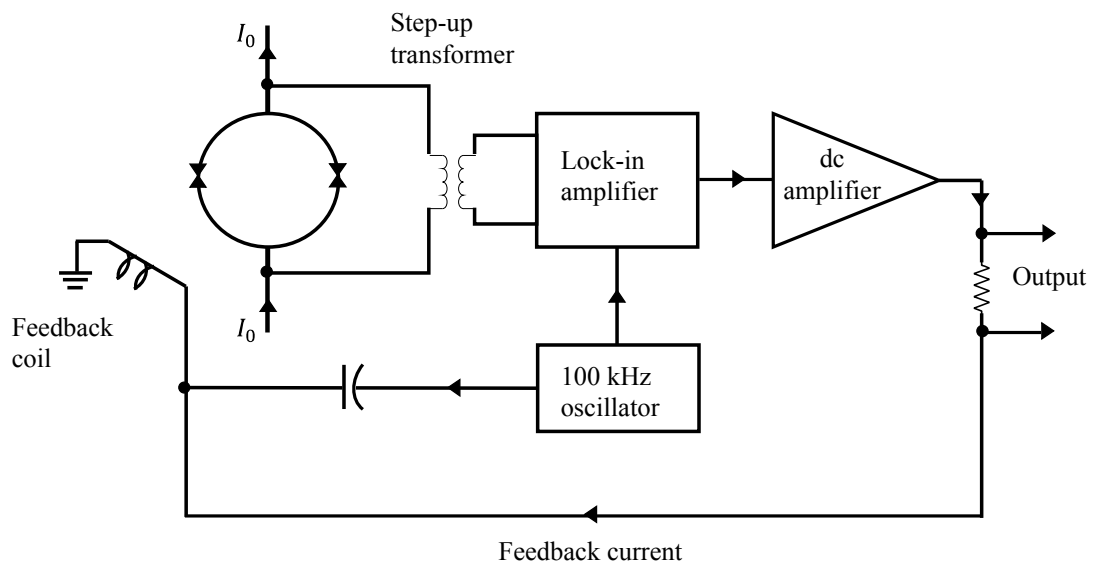


Figure 2.7: Schematic diagram of DC SQUID (superconducting quantum interference device) [150].

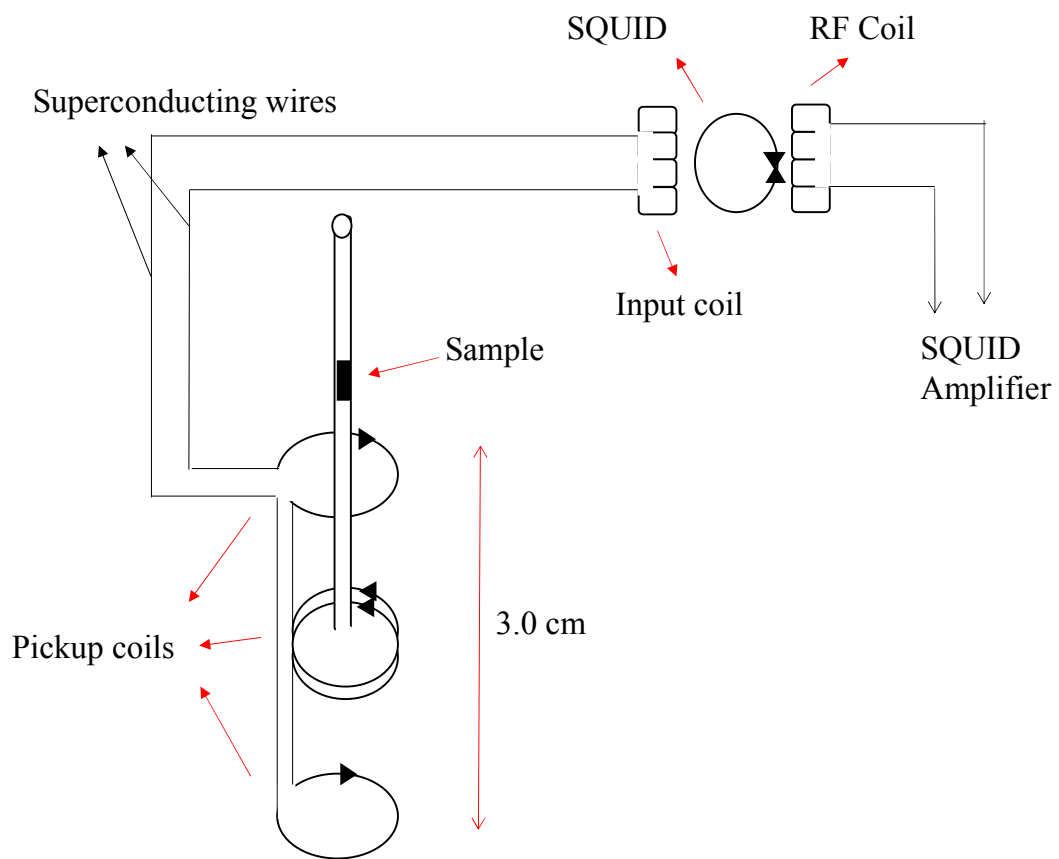


Figure 2.8: Schematic diagram of DC SQUID system in the magnetic property measurement system (MPMS) [151].

three coils, the upper and the bottom coils are a single turn wound clockwise whereas the central coil is a two-turn wound counter clockwise. This detection coil is connected to the input coil through the superconducting wires as shown in Fig. 2.8. When the sample moves through the pick-up coil, an induced current will be produced in the coil which is proportional to the magnetization of the sample in the SQUID. The SQUID produces the output voltage which is then amplified and read out by the magnetometer's electronics. Monitoring the output voltage of the SQUID as a function of the sample temperature enables to track changes in the sample magnetization with the temperature.

In this thesis, VSM equipped with a Quantum Design Magnetic Property Measurement System (MPMS) and Lakeshore VSM 7400 was used for the magnetization measurements of $\text{HoFe}_{1-x}\text{Cr}_x\text{O}_3$ compounds at low temperatures and high temperatures respectively.

2.6.3 Physical property measurement system (PPMS)

The Quantum Design physical property measurement system (PPMS) magnetometer is an advanced instrument uniquely designed for the characterization of materials with an ability to perform a variety of properties including AC/DC magnetization, resistivity, heat capacity and thermal transport. This systems is capable to operate at the temperatures range of 1.9 K to 400 K over a wide range of magnetic fields.

The heat capacity holder used in PPMS consists a copper puck frame, a sample platform and a copper cap to cover the sample platform with the sample on it, which is shown in Fig. 2.9 [152]. The eight platinum wires connect the sample platform to the frame. There is a platform heater and a platform thermometer, attached to the bottom side of the sample platform. The small sample is weighed and located on the platform by using a thin layer of Apiezon grease, providing the required thermal contact to the platform.

The Quantum Design Heat Capacity option in PPMS measures the heat capacity of the solid at constant pressure, using the relaxation time technique. The relaxation

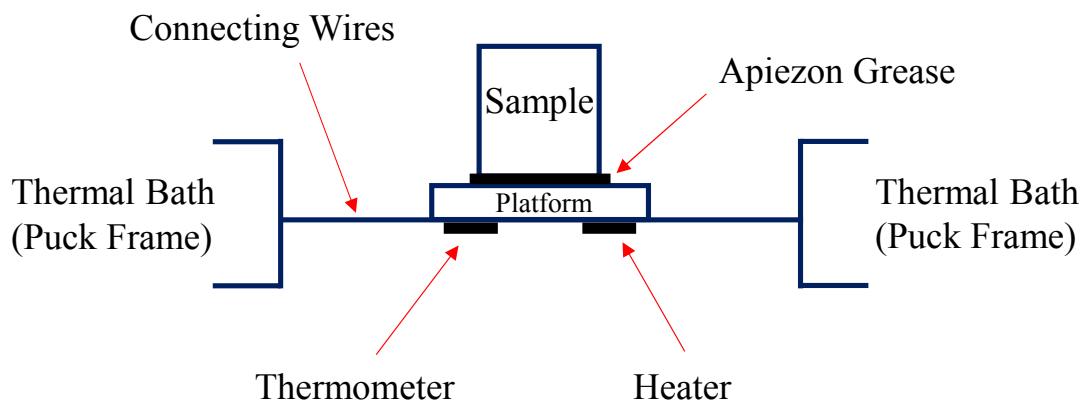


Figure 2.9: Thermal connections to sample and sample platform in PPMS Heat Capacity Option [152].

technique used here involves a cyclic process of supply and removal of controlled amount of heat, while monitoring the temperature change of the sample. The heat is supplied at a constant power for a fixed time and cooling of the sample would be done for the same duration. After the measurement of each cycle, heat capacity option fits the response of the sample platform over entire temperature range to a model that accounts for both the thermal relaxation between the platform and the sample itself. The effect of the relaxation between the platform and sample must be considered when there is a poor thermal contact between them. Heat capacity measurements were performed in the high vacuum so that the thermal conductance between the sample platform and thermal bath is dominated by the conductance of the metallic wires.

In order to perform the heat capacity measurement of each sample, first the heat capacity of the addenda, i.e., the sample holder with the small amount of the thermal grease on it, was measured and second the sample was mounted and the heat capacity of the sample plus the addenda (total heat capacity) was carried out. The heat capacity of the sample was determined by subtracting the heat capacity of the addenda from the total heat capacity.

In this thesis, Quantum Design Physical Property Measurement System (PPMS) was used to measure temperature dependent heat capacity of $\text{HoFe}_{0.25}\text{Cr}_{0.75}\text{O}_3$ compound under various magnetic fields.

Chapter 3

Structural and optical properties of $\text{HoFe}_{1-x}\text{Cr}_x\text{O}_3$ ($0 \leq x \leq 1$) compounds

This chapter deals with the structural and optical properties of $\text{HoFe}_{1-x}\text{Cr}_x\text{O}_3$ ($0 \leq x \leq 1$) compounds. The characterization of $\text{HoFe}_{1-x}\text{Cr}_x\text{O}_3$ ($0 \leq x \leq 1$) compounds and the analysis of the results obtained are presented.

3.1 Experimental details

Polycrystalline $\text{HoFe}_{1-x}\text{Cr}_x\text{O}_3$ ($0 \leq x \leq 1$) compounds were prepared by conventional solid state reaction method. High purity oxide powders of Ho_2O_3 , Fe_2O_3 , and Cr_2O_3 (purity > 99.9%) (Sigma-Aldrich Chemicals India) were used as starting raw materials and were mixed together in stoichiometric ratio. The mixture thus obtained was thoroughly and repeatedly ground in the isopropanol alcohol using the agate mortar and pestle to ensure homogeneity. Pellets were prepared using the resultant powder and sintered sequentially at 1000°C for 12 h, 1200°C for 12 h and 1250°C for 24 h respectively. The phase purity or structural analysis was carried out at room temperature using the powder x - ray diffraction (XRD) (PANalytical x - ray diffractometer) with Cu K_α radiation ($\lambda = 1.5406 \text{ \AA}$) and with a step size of 0.017° in the wide range of the Bragg angles 2θ (200 - 800). Raman spectra was measured at room temperature using a Laser Micro Raman spectrometer (Bruker, Senterra) with an excitation source of 535 nm with a power of 10 mW. Optical absorbance of the compounds were measured at room temperature using the Perkin Elmer Lambda 1050 UV-Vis-NIR spectrophotometer in the wavelength range of 200 – 800 nm.

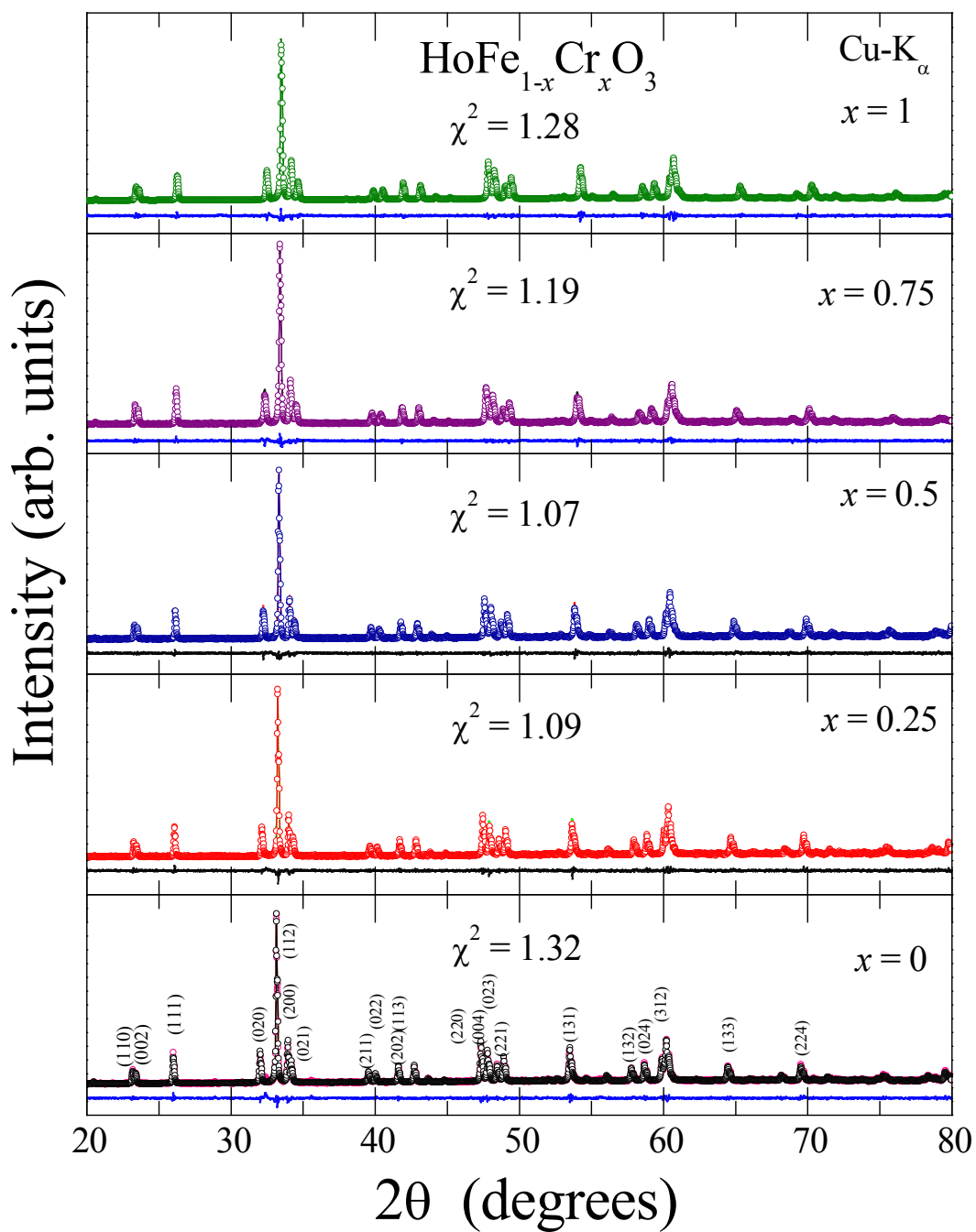


Figure 3.1: Powder x-ray diffraction patterns of $\text{HoFe}_{1-x}\text{Cr}_x\text{O}_3$ ($0 \leq x \leq 1$). It is evident that all the compounds are formed in single phase.

Table 3.1: Lattice parameter, cell volume, selected bond lengths, bond angles from Rietveld refinement pertinent to $\text{HoFe}_{1-x}\text{Cr}_x\text{O}_3$ ($0 \leq x \leq 1$) compounds.

Compounds	HoFeO_3	$\text{HoFe}_{0.75}\text{Cr}_{0.25}\text{O}_3$	$\text{HoFe}_{0.5}\text{Cr}_{0.5}\text{O}_3$	$\text{HoFe}_{0.25}\text{Cr}_{0.75}\text{O}_3$	HoCrO_3
Space group	Pbnm	Pbnm	Pbnm	Pbnm	Pbnm
Lattice Parameters					
a (Å)	5.283(6)	5.274(6)	5.266(6)	5.256(7)	5.250(8)
b (Å)	5.591(6)	5.574(6)	5.555(6)	5.537(7)	5.516(8)
c (Å)	7.609(8)	7.592(8)	7.575(8)	7.557(10)	7.543(11)
Cell Volume (Å ³)	224.7909	223.2507	221.6610	219.9814	218.4764
Selected bond angles (°)					
Fe(Cr) – O1 – Fe(Cr)	144.2(5)	144.0(5)	145.3(4)	145.8(4)	146.2(4)
Fe(Cr) – O2 – Fe(Cr)	144.7(4)	145.5(4)	144.45(33)	145.47(31)	146.13(34)
Selected bond lengths (Å)					
Fe(Cr) – O1	1.9990(30)	1.9959(28)	1.9840(23)	1.9767(21)	1.9708(23)
Fe(Cr) – O2	2.037(9)	2.033(8)	2.035(8)	2.015(6)	2.005(7)

3.2 Structural properties

Phase purity of the $\text{HoFe}_{1-x}\text{Cr}_x\text{O}_3$ ($0 \leq x \leq 1$) compounds is confirmed with the room temperature powder XRD. Intense reflections that are present in XRD (Fig. 3.1) are allowed reflections for a GdFeO_3 type distorted perovskite structure described by orthorhombic with a space group of Pbnm. For $x = 0$ compound, in addition to the parent phase of HoFeO_3 , indeed there exists a small peak corresponding to iron garnet ($\text{Ho}_3\text{Fe}_5\text{O}_{12}$) phase at around 32° and 35° [153]. As shown in Fig. 3.1, we do not see any impurity phase when Cr^{3+} substituted ($x = 0.25, 0.5, 0.75$ and 1) to Fe^{3+} within the detectable limits of the XRD.

It has been identified that the rare earth iron garnet ($\text{R}_3\text{Fe}_5\text{O}_{12}$) phase is stable compared to orthoferrites (RFeO_3) at high temperature [154]. The percentage of observed garnet phase ($\text{Ho}_3\text{Fe}_5\text{O}_{12}$) is around 5 - 6 %. In order to get more insights about the structural aspects, we also have performed the Rietveld refinement using the General Structural Analysis System (GSAS) [155]. Information extracted from the refinement is depicted in the Table 3.1.

From the Rietveld refinement data, small χ^2 values of all the compounds infer that there exists good agreement between the observed and the calculated diffraction patterns. It is evident from Fig. 3.2 (a) that extracted lattice parameter decreases and is consistent with the fact that ionic radius of Fe^{3+} (0.645 \AA) is larger than that of Cr^{3+} (0.615 \AA) [156]. It is worth noting that the change in the position and the shape of the diffraction peaks with Cr^{3+} concentration is minimal, hinting that there exists no structural transformation as a result of the Cr^{3+} dopants. The mismatch in ionic radii of Cr^{3+} and Fe^{3+} may lead to lattice distortion and such distortion can be quantified using the Goldschmidt's tolerance factor (GTF). In general, the GTF can be defined as

$$t = \frac{r_A + r_O}{\sqrt{2}(r_B + r_O)} \quad \dots\dots (3.1)$$

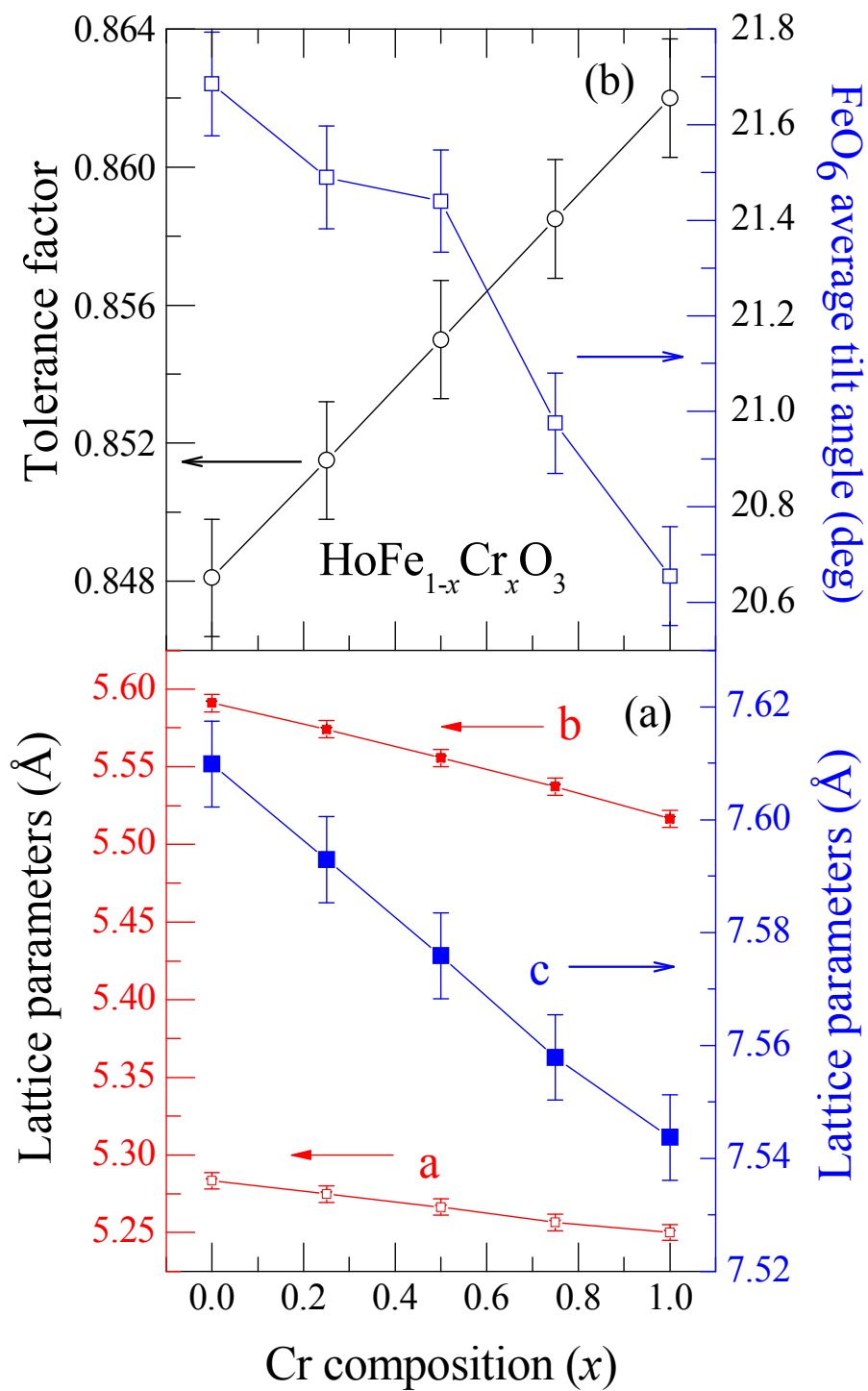


Figure 3.2: (a) Variation of lattice parameter with Cr composition. (b) Variation of tolerance factor (circle symbol) and FeO_6 average tilt angle (square symbol) with Cr composition.

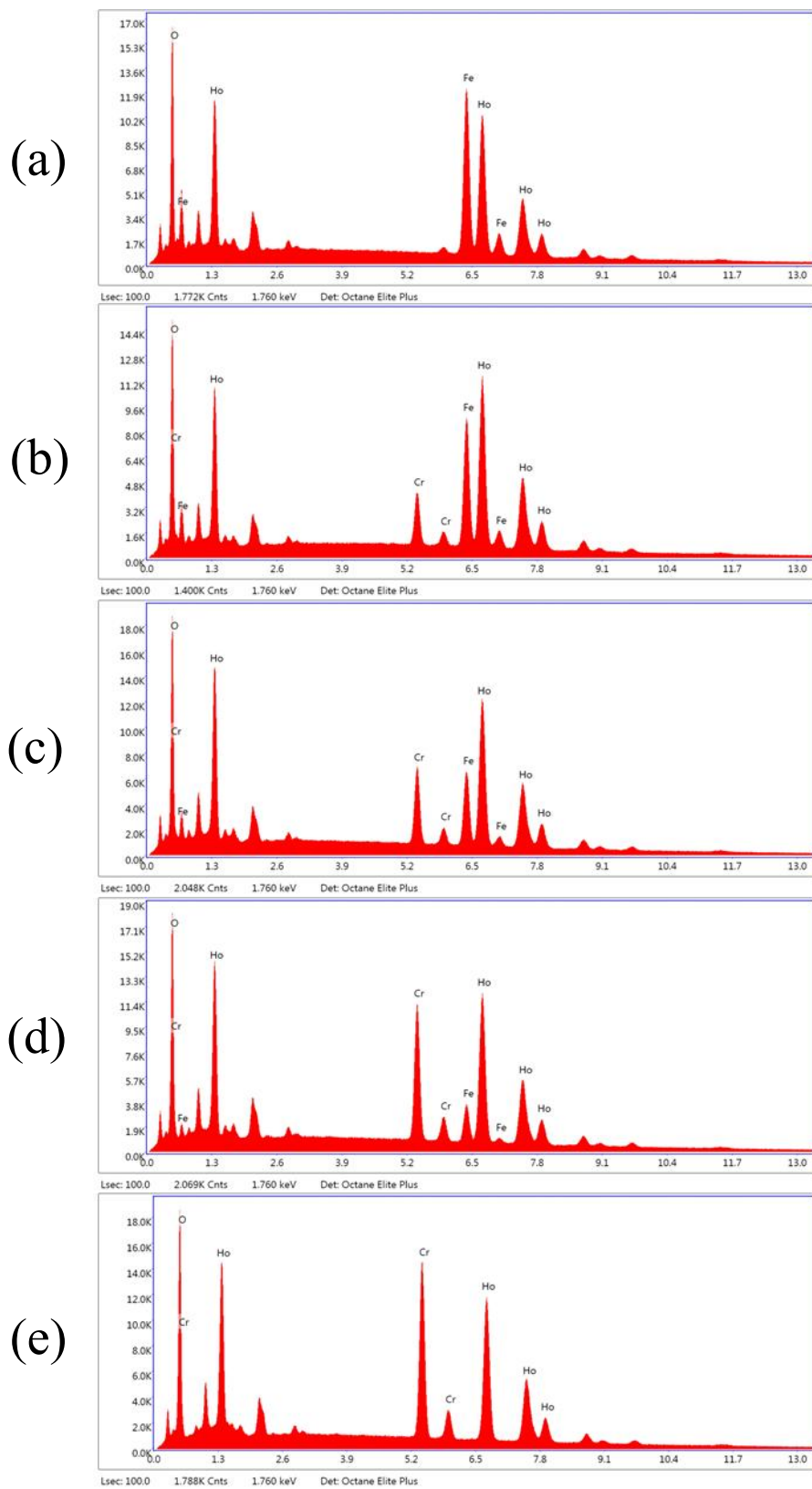


Figure 3.3: Energy Dispersive X-ray Spectroscopy of $\text{HoFe}_{1-x}\text{Cr}_x\text{O}_3$ compounds with (a) $x = 0$, (b) $x = 0.25$, (c) $x = 0.5$, (d) $x = 0.75$ and (e) $x = 1$ compositions.

Table 3.2: Atomic percentage (%) of $\text{HoFe}_{1-x}\text{Cr}_x\text{O}_3$ compounds obtained from EDAX results.

$\text{HoFe}_{1-x}\text{Cr}_x\text{O}_3$	$x = 0$	$x = 0.25$	$x = 0.5$	$x = 0.75$	$x = 1$
Ho	23.82	27.86	27.12	26.71	25.82
Fe	29.45	22.46	14.48	7.12	0
Cr	0	8.84	12.27	21.17	27.37

where r_A , r_B , and r_O are the radii of Ho^{3+} , $\text{Fe}^{3+}/\text{Cr}^{3+}$, and O^{2-} respectively, where $r_B = (1-x)r_{\text{Fe}} + xr_{\text{Cr}}$. GTF for all the compounds in the present investigation are found to be in the range of 0.848 – 0.868, which is in the range for a compound to be in an orthorhombic structure.

The variation of the GTF with respect to the Cr^{3+} composition is depicted in Fig. 3.2 (b). Upon closer observation, the GTF is found to increase as a function of the chromium content, hinting that the increase in stability and tendency towards the cubic structure upon Cr^{3+} doping. We have also calculated the average tilt angle $\langle\varphi\rangle$ of FeO_6 octahedral around the pseudo cubic [112] direction using the geometric relation that has been proposed by O’Keefe and Hyde [157] and two super exchange angles $\theta_1 = \text{Fe}(\text{Cr})\text{-O1-Fe}(\text{Cr})$, $\theta_2 = \text{Fe}(\text{Cr})\text{-O2-Fe}(\text{Cr})$. Both the above angles $\text{Fe}(\text{Cr})\text{-O1-Fe}(\text{Cr})$ and $\text{Fe}(\text{Cr})\text{-O2-Fe}(\text{Cr})$ are extracted from the structural refinement. From Fig. 3.2 (b), it is evident that average tilt angle $\langle\varphi\rangle$ of FeO_6 octahedral decreases with the increase of Cr^{3+} content. In summary, the tolerance factor increases while the tilt angle diminishes, hinting that the internal stress as a result of chemical pressure (via Cr^{3+} doping) leads to lattice distortion.

In order to confirm the composition of the synthesized powders, Energy Dispersive X-ray Spectroscopy (EDAX) analysis was carried out and the corresponding spectrum is shown in Fig. 3.3 (a-e). The EDAX measurements will be useful to confirm the atomic ratio of components. However, it is not expected to get exact atomic ratio of the metal oxides due to some oxygen contribution on the surface. From Fig. 3.3 (a-e), it is evident that the EDAX spectrum shows the presence of Ho, Fe, Cr and O elements in the $\text{HoFe}_{1-x}\text{Cr}_x\text{O}_3$ ($0 \leq x \leq 1$) compounds with no other impurities. Gold and palladium peaks are seen as we have coated the compounds with gold-palladium alloy in order to prevent charging of the specimen. Table 3.2 presents the atomic percentage of cations in $\text{HoFe}_{1-x}\text{Cr}_x\text{O}_3$ ($0 \leq x \leq 1$) compounds. The results of EDAX analysis indicates that the atomic ratio of Fe/Cr and Ho is as per the intended stoichiometric composition of the $\text{HoFe}_{1-x}\text{Cr}_x\text{O}_3$ ($0 \leq x \leq 1$) compounds.

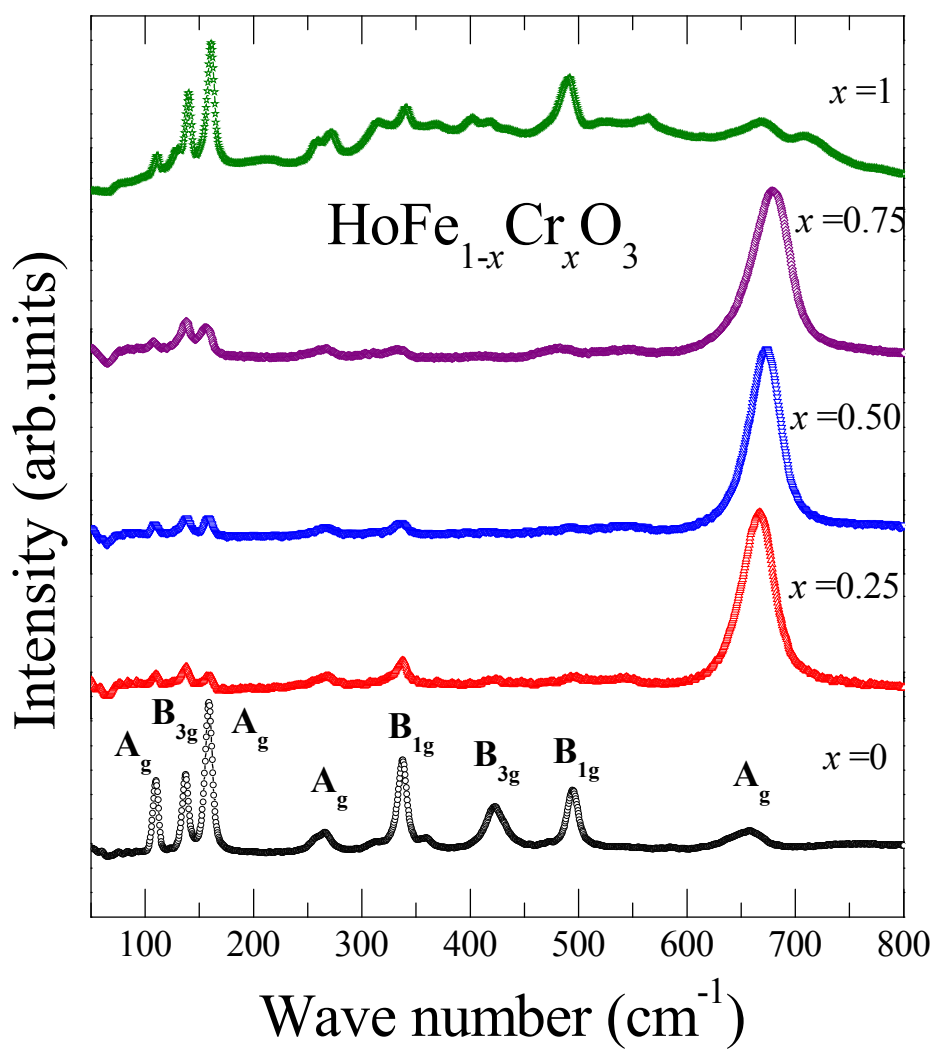


Figure 3.4: Room temperature Raman spectra of $\text{HoFe}_{1-x}\text{Cr}_x\text{O}_3$ ($0 \leq x \leq 1$) compounds with an excitation of 532 nm.

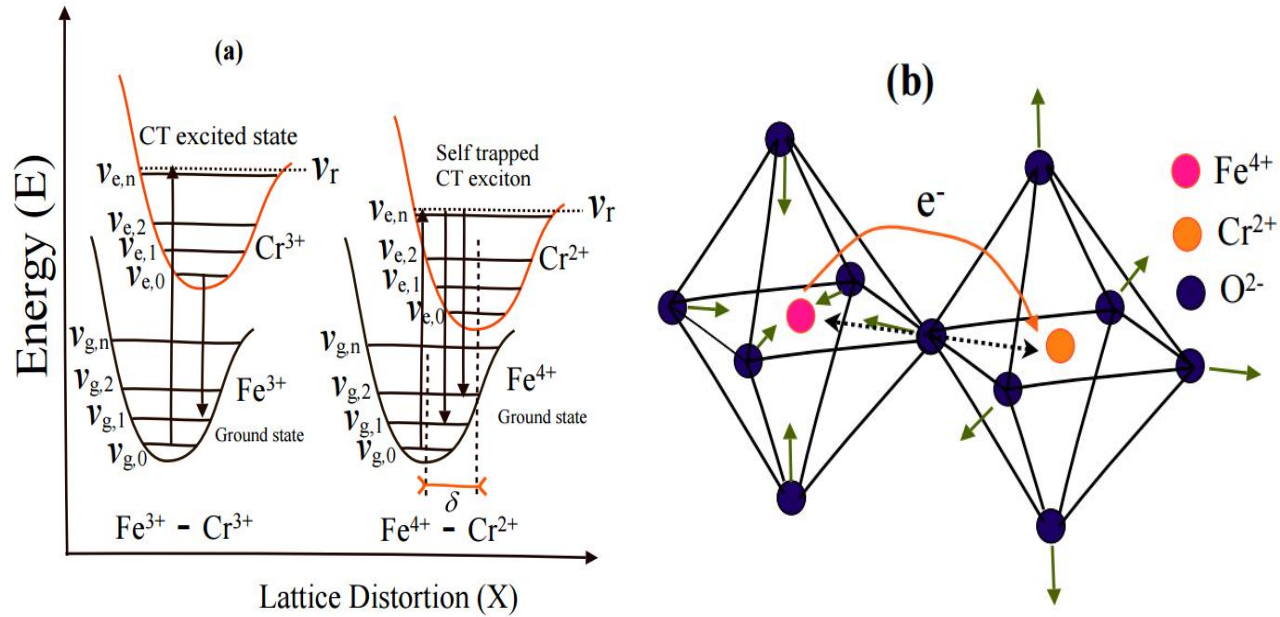


Figure 3.5: (a) Franck-Condon (FC) mechanism for Jahn-Teller active perovskites. $v_{g,0}, v_{g,1}, v_{g,2}, \dots, v_{g,n}$ and $v_{e,0}, v_{e,1}, v_{e,2}, \dots, v_{e,n}$ represents the vibrational states of Fe^{3+} and Cr^{3+} respectively. For FC mechanism to happen for a vibrational mode, the virtual state $|v_r\rangle$ of Raman process must coincide with any vibrational state of electronically excited state. δ indicates lattice distortion due to Jahn - Teller effect as a result of charge transfer mechanism (b) Octahedral sites of Fe^{4+} and Cr^{2+} respectively. Dotted arrow in the figure indicates charge transfer mechanism and lattice relaxation.

Now we discuss the results pertinent to the Raman scattering which essentially gives the local structure, shift and distortion of the modes as a result of the chemical pressure (here Cr^{3+} doping). In addition, we also would like to correlate our structural information with the Raman data that we obtained. For this purpose the room temperature Raman spectroscopy was performed on $\text{HoFe}_{1-x}\text{Cr}_x\text{O}_3$ ($0 \leq x \leq 1$) compounds to understand aforesaid properties. It has been observed that in an ideal perovskite (ABO_3), the B-site transition metal cation locates at the centre of the oxygen octahedral and A-site cation locates at the corners of the cube [158]. However, due to the displacement of the crystallographic sites from the ideal cubic positions, most perovskites show the symmetry breaking which results the appearance of the Raman active modes in the Raman spectra. The rare earth orthoferrite HoFeO_3 is an orthorhombically distorted perovskite with a space group of D_{2h}^{16} (Pbnm).

The irreducible representations corresponding to the phonon modes at the Brillouin zone center [159] can be defined as follows

$$7A_g + 7B_{1g} + 5B_{2g} + 5B_{3g} + 8A_u + 8B_{1u} + 10B_{2u} + 10B_{3u}$$

Here, A_g , B_{1g} , B_{2g} , B_{3g} are the Raman active mode species, B_{1u} , B_{2u} , B_{3u} are the infrared mode species and A_u is the inactive mode. Among them the modes which are above 300 cm^{-1} are related to the vibrations of oxygen and the modes below the wave number 300 cm^{-1} are associated with the rare earth ions [160]. However, the Raman vibrational modes corresponding to an orthorhombic structure are: $A_g + B_{1g}$ and $2B_{2g} + 2B_{3g}$, which are symmetric and antisymmetric modes respectively; In contrast, $A_g + 2B_{1g} + B_{3g}$, $2A_g + 2B_{2g} + B_{1g} + B_{3g}$, and $3A_g + B_{2g} + 3B_{1g} + B_{2g}$ are associated with the bending modes, rotation and tilt mode of octahedral and for the changes in the rare earth movements respectively [161].

Figure 3.4 shows results pertinent to the Raman Spectra of $\text{HoFe}_{1-x}\text{Cr}_x\text{O}_3$ ($0 \leq x \leq 1$) compounds recorded at room temperature and in the wavenumber range of 50 to 800 cm^{-1} . Peaks with the high intensities are evident at 109 , 137 , 158 , 337 , 423 and 494 cm^{-1} which is normal for a typical orthoferrite [159]. Apart from

aforesaid modes, a mode around 670 cm^{-1} prevailed in the compounds with a Cr^{3+} ion. However, the peak which is evident around 670 cm^{-1} consists very less intensity in parent HoFeO_3 and HoCrO_3 compounds spectra. Basically, such peak picks intensity whenever there exists a combination of both the Fe^{3+} and Cr^{3+} at B-site. Such intriguing phenomenon may be correlated to the orbital mediated electron – phonon coupling like in case of $\text{LaFe}_{1-x}\text{Cr}_x\text{O}_3$ [120]. The Raman active modes of the compounds are designated according to the method proposed by Gupta [162] *et. al.*. The appearance of an A_g like mode with observable intensity at high frequency of around 670 cm^{-1} can be attributed to an in-phase stretching (breathing) mode of oxygen in the close vicinity of the substituted Cr^{3+} ion. Essentially the oxygen breathing mode is activated by the charge transfer between Fe^{3+} and Cr^{3+} through an orbital mediated electron-phonon coupling mechanism [120].

In $\text{HoFe}_{1-x}\text{Cr}_x\text{O}_3$ compounds, the ground state electron configuration of Fe^{3+} does not support orbital mediated electron-phonon coupling due to the lack of strongly interacting half-filled e_g levels in both Fe^{3+} (d^5) and Cr^{3+} (d^3). To facilitate such an orbital mediated electron-phonon coupling, the electronic configuration of Fe^{3+} must contain partially filled e_g orbital (like Fe^{4+}) such that d^4 electron of the Fe^{4+} ion can move to upper e_g levels of Cr^{2+} to create electronic excitation as reported in LaMnO_3 [163].

Figure 3.5 explains the mechanism for orbital mediated electron-phonon coupling. The left part of Fig. 3.5 (a) shows electronic states of Fe^{3+} and Cr^{3+} ions. $v_{g,0}, v_{g,1}, v_{g,2}, \dots, v_{g,n}$ and $v_{e,0}, v_{e,1}, v_{e,2}, \dots, v_{e,n}$ represents the vibrational states of Fe^{3+} and Cr^{3+} respectively. Right part of the Fig. 3.5 (a) reveals electronic states of the Fe^{4+} and Cr^{2+} ions. Arrows on both Fig. 3.5 (a) and 3.5 (b) represents various transitions between $\text{Fe}^{3+} \rightarrow \text{Cr}^{3+}$ and $\text{Fe}^{4+} \rightarrow \text{Cr}^{2+}$ respectively.

It has been reported that a photon mediated charge transfer can takes place between Fe^{3+} and Cr^{3+} ions upon irradiation with a laser of wavelength 532 nm [120, 164]. In this process, the overlap between the d-orbitals of Cr^{2+} and p -orbitals of oxygen couples through a lattice distortion, causing a self-trapping motion.

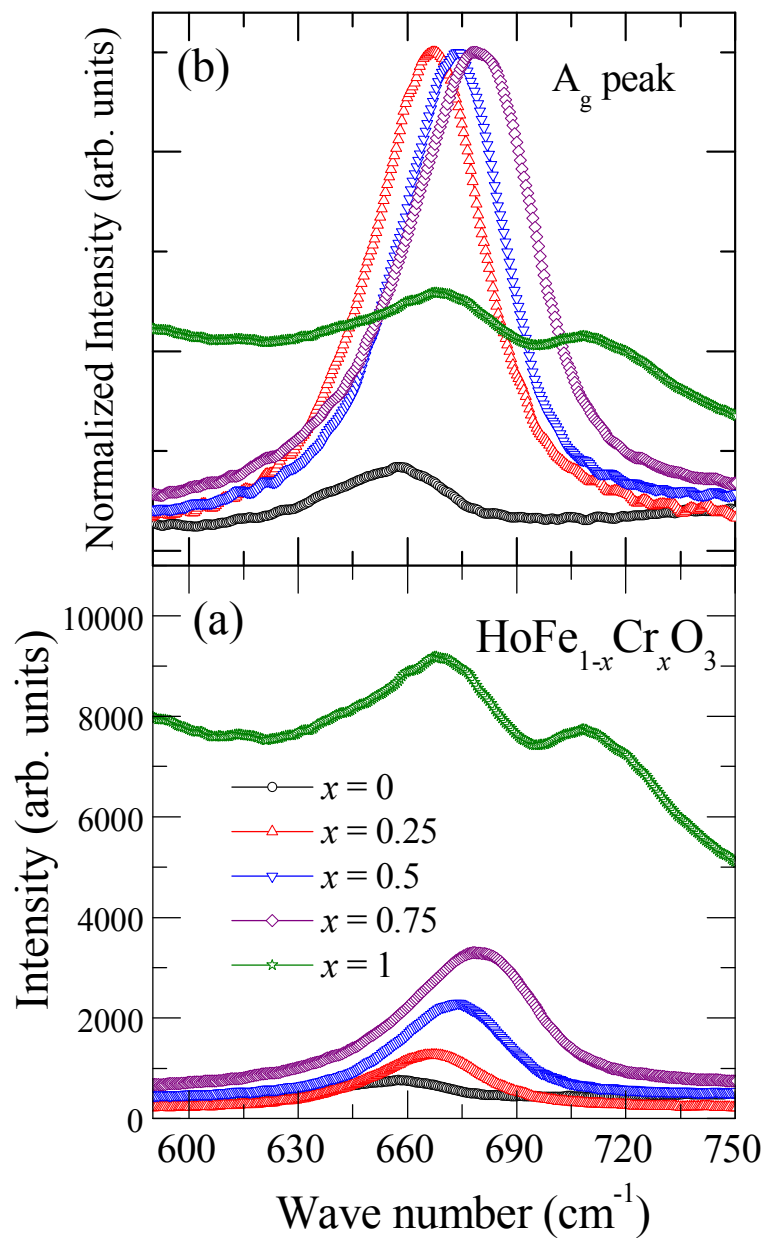


Figure 3.6: (a) Intensity variation of A_g peak and (b) wave number shift of A_g peak for the $\text{HoFe}_{1-x}\text{Cr}_x\text{O}_3$ ($0 \leq x \leq 1$) compounds.

Evidently, this motion increases the lifetime of excited Cr^{2+} electronic ground state long enough to interact with the intrinsic phonon mode.

Essentially, during the charge transfer mechanism (CT), when the photon energy equals to the CT energy gap between the two transition metal ions Fe^{3+} and Cr^{3+} , electrons in Fe^{3+} excite to Cr^{3+} ion and leaves them in a strongly coupled d^4 - d^4 configuration with half-filled bands. The change in the charge density of e_g orbital of transition metal surrounded by the oxygen octahedral activates a breathing distortion of O_6 around the transition metal cation which appears in the Raman spectrum at around 670 cm^{-1} . This configuration is Jahn-Teller active, hence, that it leads to a volume preserving lattice distortion (δ), involves a stretching of Fe (Cr)-O bonds along z direction and compression in x-y plane.

As a result of the Jahn - Teller effect, an electron in e_g orbital collapse into the lower energy state which produces a potential minimum. This minimum potential traps the electron in that orbital (self-trapping) and increases its life time in the excited Cr^{2+} state long enough for it to interact with intrinsic phonon mode/lattice distortion. In the perturbed state, indeed there exists a contraction of the oxygen octahedral surrounding to Fe^{4+} ion and leads to an expansion in adjacent octahedron surrounding to Cr^{2+} ion as shown in Fig. 3.5 (b). The oxygen lattice relaxes back to its unperturbed state when the electron transfers back to Fe^{3+} state. In this fashion, the charge transfer of an electron from Fe^{3+} to the Cr^{3+} ion activates an oxygen breathing mode of A_g symmetry through orbital mediated electron-lattice coupling.

The increase in the intensity of the peak at around 670 cm^{-1} is observed only in doped compounds as shown in Fig. 3.6 (a). Essentially, upon adding the Cr^{3+} to Fe^{3+} , indeed there is an enhancement in the intensity of the Raman peak at around 670 cm^{-1} , which has been ascribed to an increase in the degree of disorder. As the Cr^{3+} content increases, there would indeed be an increase in degree of disorder, which may enhance the interaction between lattice distortion and the charges transferred between Fe^{3+} - Cr^{3+} . Eventually as a result of this there would be an

enhancement in the electron-phonon coupling which leads to increase in the intensity of peak around 670 cm^{-1} . The broadening of the peak around 670 cm^{-1} with increase in the amount of Cr^{3+} ions at Fe^{3+} site can correlate with the structural disorder. This is confirmed by the observed change in the lattice parameters by substitution of Cr^{3+} ions at Fe^{3+} site. The observed shift in the wave number towards higher values (Blue shift) in the doped compounds shown in Fig. 3.6 (b), this can be attributed to the compressive strain produced in the material by incorporating the Cr^{3+} ion at iron site. This effect is supported by the change in Fe (Cr) – O bond lengths as well as FeO_6 octahedral tilt angle with respect to the chromium content at Fe^{3+} site as shown in the Table 3.1.

3.3 Optical properties

The optical absorbance of the $\text{HoFe}_{1-x}\text{Cr}_x\text{O}_3$ ($0 \leq x \leq 1$) compounds were recorded at room temperature and are shown in Fig. 3.7. Indeed there exists a direct band gap and the value of gap is determined using the Tauc's equation [147]. Essentially this equation relates the optical absorption coefficient (α), photon energy ($h\nu$) and the energy gap E_g as given below

$$\alpha h\nu = (h\nu - E_g)^{1/2} \quad \dots\dots (3.2)$$

Optical band gaps of the $\text{HoFe}_{1-x}\text{Cr}_x\text{O}_3$ ($0 \leq x \leq 1$) compounds are obtained using the above equation and by extrapolating the linear region of the curve to zero in $h\nu$ vs. $(\alpha h\nu)^2$ as shown in Fig. 3.8 (a).

The origin of the prominent peak in the Tauc's plot in the case of $x = 1$ (HoCrO_3) compound can be explained as follows. The optical absorption bands commonly observed in orthochromites arising from $d-d$ transitions of Cr^{3+} ions. The mechanism responsible for these bands has been explained by the crystal field splitting [165]. Cr^{3+} ion has a d^3 electronic configuration and a strong octahedral site preference. In the ground state, these electrons occupy the t_{2g} orbitals. The two e_g orbitals are empty, providing two holes into which the electrons can be promoted. The three unpaired electrons give rise to the free ion terms 4F , 4P , 2G and several other doublet states of which 4F is the ground state. In the octahedral

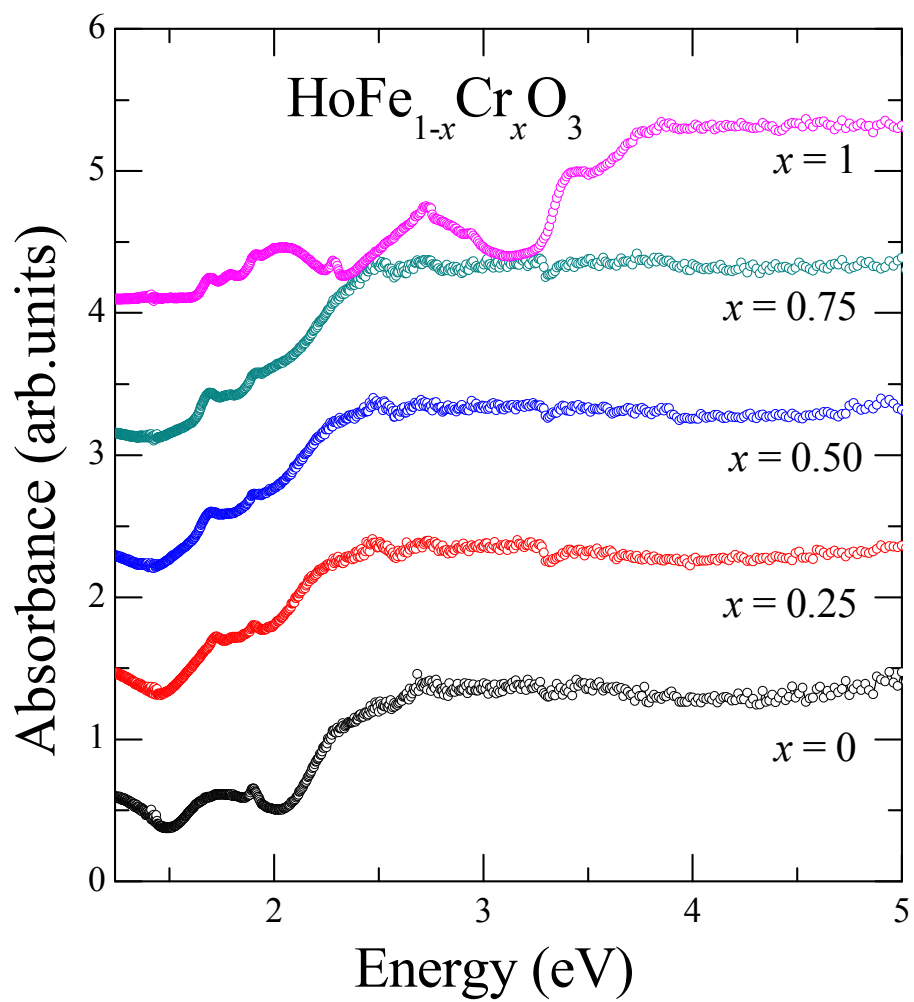


Figure 3.7: Absorption spectra of $\text{HoFe}_{1-x}\text{Cr}_x\text{O}_3$ ($0 \leq x \leq 1$) compounds.

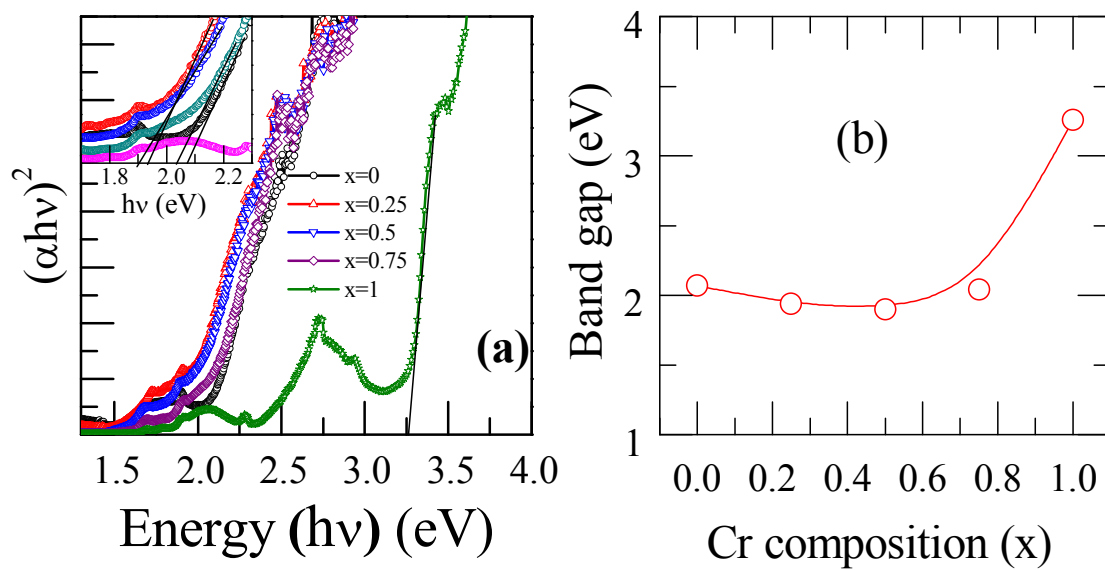


Figure 3.8: (a) Tauc's plots to determine the band gap values of $\text{HoFe}_{1-x}\text{Cr}_x\text{O}_3$ ($0 \leq x \leq 1$) compounds. (b) Variation of the band gap with respect to Cr composition.

field, the 4F state splits into $^4A_{2g}(F)$, $^4T_{2g}(F)$ and $^4T_{1g}(F)$ states, the 4P state does not split but transforms into a $^4T_{1g}(P)$ state and the 2G state splits into $^2A_{1g}(G)$, $^2T_{1g}(G)$, $^2T_{2g}(G)$ and $^2E_g(G)$. The ground state for Cr^{3+} ions is $^4A_{2g}(F)$ at all strengths of the crystal field. The prominent peak in the forbidden gap region in the case of $HoCrO_3$ compound is corresponding to $d-d$ transition from $^4A_{2g} \rightarrow ^4T_{1g}$ state.

The direct band gap value for $HoFeO_3$ and $HoCrO_3$ is calculated as 2.07 eV and 3.26 eV respectively. From the Fig. 3.8 (b) and for the compounds with the combination of Fe^{3+} and Cr^{3+} , it is evident that the band gap decreases with Cr^{3+} content, and reached a minimum value of 1.94 eV at $x = 0.5$. Further increase in Cr^{3+} content results in increase of the band gap value and a reached a maximum value of 3.26 eV at $x = 1$. In order to explain the observed band gap variation we would like to propose a possible mechanism using energy diagram of $HoFeO_3$, $HoCrO_3$ and $HoFe_{1-x}Cr_xO_3$. Figure 3.9 (a) shows the energy diagram of $HoFeO_3$ with the band gap value of 2.07 eV (b) the energy diagram of $HoCrO_3$ with the band gap value of 3.26 eV and (c) probable energy diagram for $HoFe_{1-x}Cr_xO_3$ for which the band gap varies between 2.07 and 3.26 eV. The variation of band gap with Cr^{3+} concentration could be due to a complex interplay between Fe^{3+} and Cr^{3+} electronic levels mediated by oxygen through superexchange interaction. From the Fig. 3.9 (c), it is evident that when $x < 0.5$, the valance band maxima (VBM) and conduction band minima (CBM) shifts to higher energy (dark red colour). The shift in VBM may be explained on the basis of hybridization of d - orbitals of Fe^{3+} and Cr^{3+} with p - orbitals of oxygen in the valance band. Essentially, the ferrimagnetically [164] coupled Fe^{3+} and Cr^{3+} induce a spin disorder on oxygen which can enhance the broadening of oxygen p - orbitals and valance band edges of

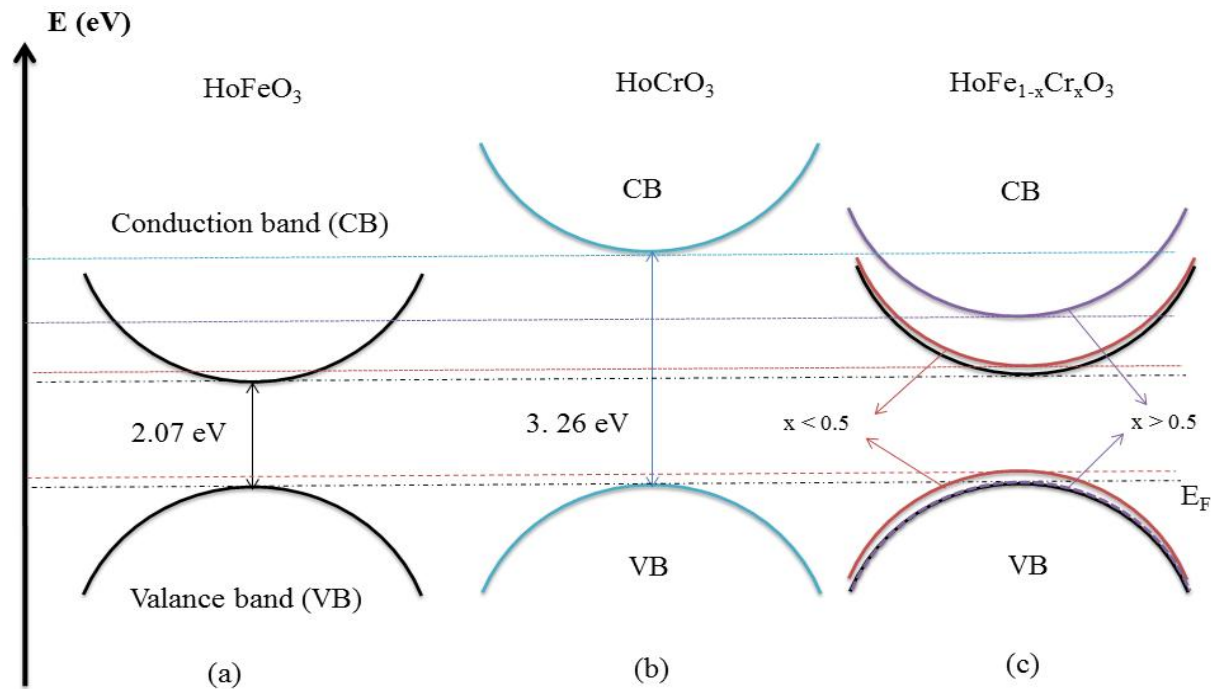


Figure 3.9: (a) Shows the energy diagram of HoFeO₃ (b) Energy diagram of HoCrO₃ (c) probable energy diagram for HoFe_{1-x}Cr_xO₃. It is evident from the frame (c) that when $x < 0.5$, the valance band maxima (VBM) and conduction band minima (CBM) shifts to higher energy (dark red color). However, the shift in VBM is due to strong hybridization of d orbitals of Fe and Cr with p - orbitals of oxygen in valance band. When $x > 0.5$, band gap is dominated by unoccupied d - orbitals of Cr in conduction band which leads to increase in band gap (purple color).

Fe³⁺ and Cr³⁺ [166-167], hinting a smaller band gap until $x = 0.5$. When $x > 0.5$, width of available un occupied d - orbitals of Fe³⁺ at conduction band reduces, which can leads to a shift of the conduction band minima to higher energies (as shown in Fig. 3.9 (c) (purple colour)). As a result, the band gap in HoFe_{1-x}Cr_xO₃ increases above $x = 0.5$ and reaches maximum value of 3.26 eV at $x = 1$. From the above results, indeed it is possible to tune the band gap in rare earth orthoferrites and other compounds with similar structure by controlling the Fe³⁺/Cr³⁺ ratio.

3.4 Conclusions

In summary, we have explored the orbital mediated electron – phonon coupling mechanism in the compounds pertinent to HoFe_{1-x}Cr_xO₃ ($0 \leq x \leq 1$). There is a striking coincidence between our structural and Raman studies. Raman studies infer that, A_g like symmetric oxygen breathing mode at around 670 cm⁻¹ in the compounds with both the Fe³⁺ and Cr³⁺. The decrease in optical band gap is ascribed to the induced spin disorder due to Fe³⁺ and Cr³⁺ on oxygen, which can leads to broadening of oxygen p -orbitals. On the other hand, increase in band gap value explained on the basis of the reduction in the available unoccupied d -orbitals of Fe³⁺ at conduction band. The present results would indeed be helpful in understanding and to develop optoelectronic devices based on orthoferrites.

Chapter 4

Magnetic and magnetocaloric properties of $\text{HoFe}_{1-x}\text{Cr}_x\text{O}_3$ ($0 \leq x \leq 1$) compounds

In this chapter we demonstrate our efforts in realizing the magnetic, hyperfine and magnetocaloric properties of $\text{HoFe}_{1-x}\text{Cr}_x\text{O}_3$ ($0 \leq x \leq 1$) compounds. Essentially, we discuss physics related with various magnetic transitions, isomer shift, quadrupole splitting and hyperfine interactions.

4.1 Experimental details

The temperature (T) dependent magnetization (M) (M vs. T) measurements were performed using a Quantum Design magnetic property measurement system (MPMS) in the temperature range of 5 – 300 K. M vs. T measurements were performed in zero field cooling (ZFC) as well as in field cooling (FC) conditions. Essentially, in ZFC conditions, the compound was cooled from 300 K to 5 K without application of any magnetic field. However, in case of FC condition, the compound was cooled from 300 K in the presence of 1000 Oe up to a desired temperature, 5 K. Magnetization measurements in the temperature range of 300 – 900 K were carried out using a high temperature vibrating sample magnetometer (HT-VSM) (LakeShore make). ^{57}Fe Mössbauer measurements were carried out in transmission mode with a ^{57}Co (Rh) radioactive source in constant acceleration mode using a standard PC-based Mössbauer spectrometer equipped with a WissEl velocity drive. Quantum Design physical property measurement system (PPMS) was used for the specific heat (C_p) measurement (Relaxation method).

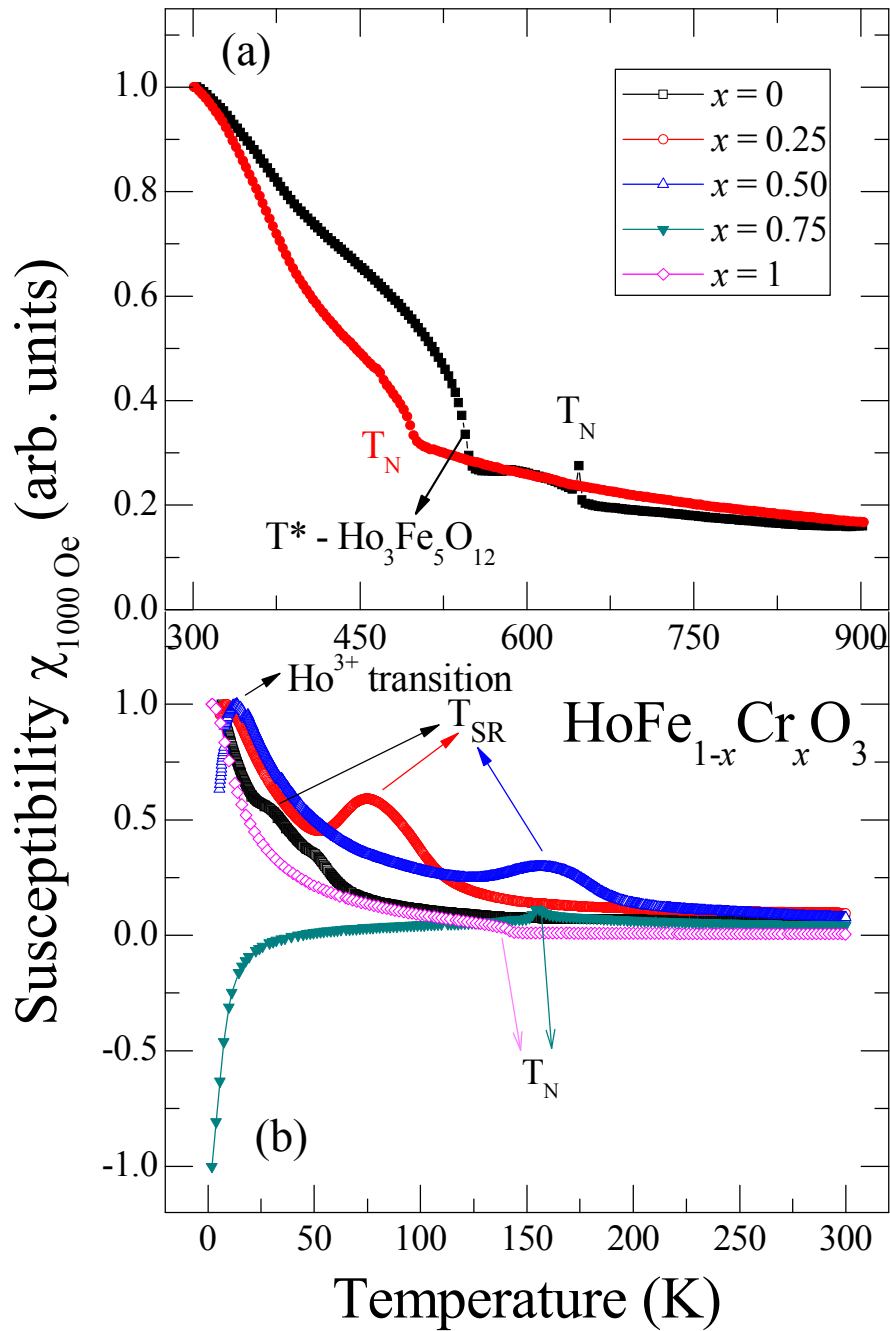


Figure 4.1: Temperature (T) dependence of susceptibility (χ) pertinent to normalized magnetization (M) at (a) high temperature and (b) low temperature region for $\text{HoFe}_{1-x}\text{Cr}_x\text{O}_3$ ($0 \leq x \leq 1$) compounds.

4.2 Magnetic and Hyperfine interactions in $\text{HoFe}_{1-x}\text{Cr}_x\text{O}_3$ ($0 \leq x \leq 1$) compounds

In this section, initially we shall discuss magnetization behaviour of $\text{HoFe}_{1-x}\text{Cr}_x\text{O}_3$ ($0 \leq x \leq 1$) compounds at high temperatures and subsequently explore the low temperature magnetization behaviour. Figure 4.1 (a) and Fig. 4.1 (b) depicts the ZFC curves pertinent to susceptibility χ of $\text{HoFe}_{1-x}\text{Cr}_x\text{O}_3$ ($0 \leq x \leq 1$) compounds at high temperatures (300-900 K) and at low temperatures (5-300 K) respectively with a magnetic field strength of 1000 Oe. From χ vs. T graph (Fig. 4.1) it is evident that indeed there exist various transitions pertinent to antiferromagnetic coupling (AFM), spin re-orientation transition (SR) and Ho^{3+} ordering. However, above transitions exists at various temperature ranges. Below we discuss physical significance, variation and origin of such transitions in a detailed way.

Initially we discuss about the evidenced antiferromagnetic transition and its variation in $\text{HoFe}_{1-x}\text{Cr}_x\text{O}_3$ ($0 \leq x \leq 1$) compounds with respect to temperature. From figure 4.1 (a), it is evident that a sudden jump prevails at 647 K for $x = 0$ compound, which can be attributed to the antiferromagnetic ordering of Fe^{3+} moments in HoFeO_3 compound [76]. The increase in the magnetization below this transition indicates a weak ferromagnetic moment (WFM) which arises due to a canted nature of Fe^{3+} moments. Apart from the above transition, another transition is evident for $x = 0$ compound at around 550 K, which corresponds to Fe^{3+} ordering in the rare earth iron garnet phase, $\text{Ho}_3\text{Fe}_5\text{O}_{12}$ [153].

We do not see any transition pertinent to iron garnet phase in the compounds other than parent compound. With Cr^{3+} , the Néel temperature (T_N) is varied in the range of 647 K ($x = 0$) to 142 K ($x = 1$) for $\text{HoFe}_{1-x}\text{Cr}_x\text{O}_3$ ($0 \leq x \leq 1$) compounds. Figure 4.2 depicts the variation of T_N pertinent to $\text{HoFe}_{1-x}\text{Cr}_x\text{O}_3$ compounds which were obtained from χ vs. T graphs. Essentially χ vs. T graphs demonstrated an antiferromagnetic transition at 647 K, 495 K, 273 K, 157 K, and 142 K for $x = 0, 0.25, 0.50, 0.75$ and 1 compounds respectively. Indeed, this indicates a decrease in the value of T_N with Cr^{3+} addition. Such a variation of T_N with Cr^{3+} could be due

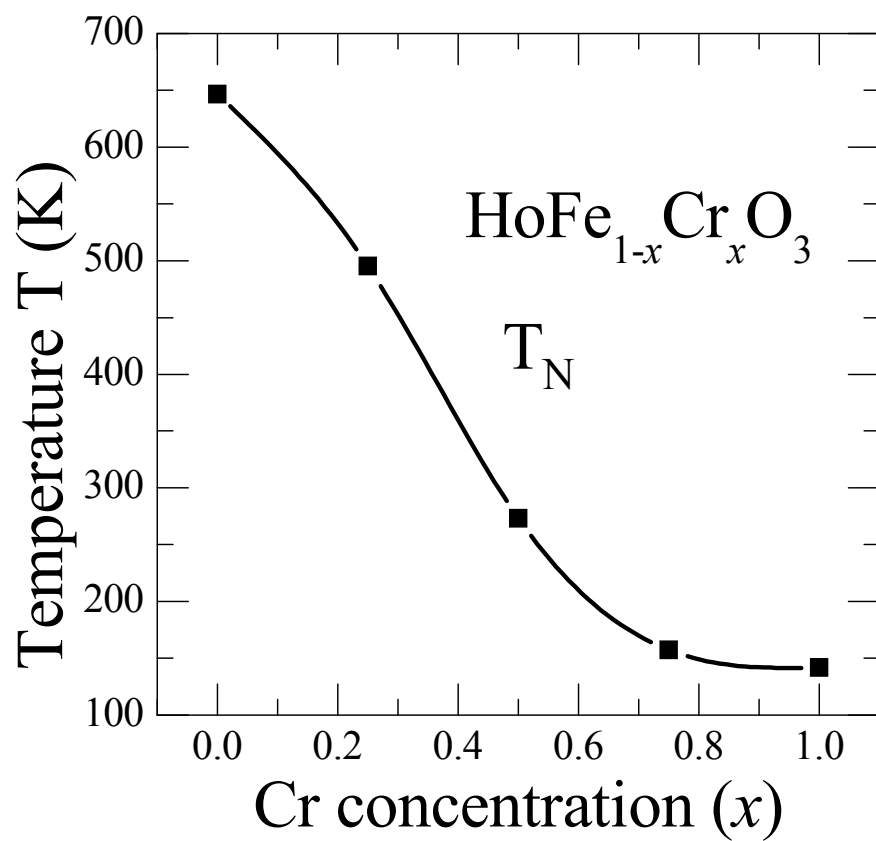


Figure 4.2: Variation of Néel temperature T_N of $\text{HoFe}_{1-x}\text{Cr}_x\text{O}_3$ ($0 \leq x \leq 1$) compounds with Cr^{3+} concentration.

to the larger ionic radius of Fe^{3+} (0.645 Å) in comparison with Cr^{3+} (0.615 Å). In our work, since we substituted Cr^{3+} to Fe^{3+} , there is a contraction of the lattice and hence the distortion in the crystal structure. Variation of lattice parameter with Cr^{3+} addition has been discussed in chapter 3.2. It has been reported that the structural distortion is closely related to the super exchange interaction and may influence T_N in orthorhombic rare-earth orthoferrites (RFeO_3) [168] and orthochromites (RCrO_3) [169].

According to Goodenough-Kanamori rule [39, 41], two adjacent transition metal ions interact through the superexchange interaction via a virtual charge transfer. The outer shell electron configuration for Fe^{3+} and Cr^{3+} are t^3e^2 and t^3e^0 respectively. In case of RFeO_3 , the π bonding of half-filled $t^3\text{-O-}t^3$ orbitals and σ - bonding of half-filled $e^2\text{-O-}e^2$ orbitals interact through superexchange interaction and are antiferromagnetic (AFM) in nature, which satisfies the Hund's rule. From this it can be inferred that the hybridization of t - e orbitals doesn't give any extra magnetic phase component to the overall superexchange interaction. On the other hand, in RCrO_3 , t - e hybridization gives a ferromagnetic (FM) component in addition to the existing AFM interaction in $t^3\text{-O-}t^3$ orbitals though the superexchange interaction [169]. As there exists both FM and AFM competing interactions through t - e hybridization in Cr rich compounds, by the substitution of Cr^{3+} to Fe^{3+} , the strength of FM interaction increases and AFM interaction diminishes, which may results in decrease of T_N .

From the above, we believe that the decrease in T_N with Cr^{3+} is not only due to the weakening of $\text{Fe}(\text{Cr})\text{-O-Fe}(\text{Cr})$ AFM exchange interaction, but also due to the enhancement in FM interaction between adjacent Cr^{3+} moments through t - e hybridization as a result of the structural distortion. In addition, we also used molecular field theory to quantify the values of T_N up on Cr^{3+} addition using the following relation. Essentially the relation between J and T_N has been defined as [170]:

$$J/k_B = \frac{3T_N}{2zS(S+1)} \quad \dots\dots (4.1)$$

where ‘z’ represents the number of nearest neighbours and its value is 6 for orthoferrites, ‘k_B’ denotes the Boltzmann’s constant (8.617 x 10⁻⁵ eV/K), S = 5/2 and 3/2 are the values pertinent to the spins of Fe³⁺ and Cr³⁺ ions respectively. Physically, *J* signifies the strength of the exchange interaction between a pair of nearest magnetic ions in the orthoferrites. Estimated values of *J* using equation 4.1 for HoFeO₃ and HoCrO₃ compounds are 18.4 K (1.5 meV) and 9.4 K (0.8 meV) respectively, which is in striking coincidence with the higher value of T_N for HoFeO₃ (647 K) in comparison with the value pertinent to HoCrO₃ (142 K).

Now we discuss about shift in SR transition with Cr³⁺ in HoFe_{1-x}Cr_xO₃ (0 ≤ *x* ≤ 1) compounds. From figure 4.1(b), it is evident that apart from a prominent peak pertinent to T_N, there exists a peak which corresponds to SR transition (T_{SR}) for the compounds with composition *x* = 0 (T_{SR} = 30 K and 50 K), *x* = 0.25 (T_{SR} = 75 K) and *x* = 0.5 (T_{SR} = 150 K) [116]. We ascribe such T_{SR} in HoFe_{1-x}Cr_xO₃ (0 ≤ *x* ≤ 1) compounds to complex exchange interaction between the Fe³⁺ and the Ho³⁺ ions [159]. For instance, in case of *x* = 0 compound, multiple SR transitions are evident at 50 K and 30 K, the former one at around 50 K is a typical transition in rare earth orthoferrites and is consistent with literature [116]. The latter one around 30 K may be due to competing Zeeman and Van Vleck mechanism [171], which vanishes up on replacing the Fe³⁺ ions with the Cr³⁺ ions. From Fig. 4.1(b), it is clear that the χ decreases below the T_{SR} for all the compositions (*x* = 0, 0.25 and 0.5), which demonstrates the rotation of Fe³⁺ moments from one crystal axis to another. The shift in the T_{SR} towards higher temperatures for the *x* = 0.25 and 0.5 compound may be ascribed to complex exchange interaction between the Fe³⁺/Cr³⁺ and the Ho³⁺ ions [159]. The T_{SR} takes place at 50 K, for *x* = 0 compound due to the domination of Ho³⁺- Fe³⁺ interaction over the Fe³⁺- Fe³⁺ interaction. As we substituted the Cr³⁺ ion at the Fe³⁺ site, this may weakens the Fe³⁺-Fe³⁺ interaction and may demand a shift in the T_{SR} to a higher temperature.

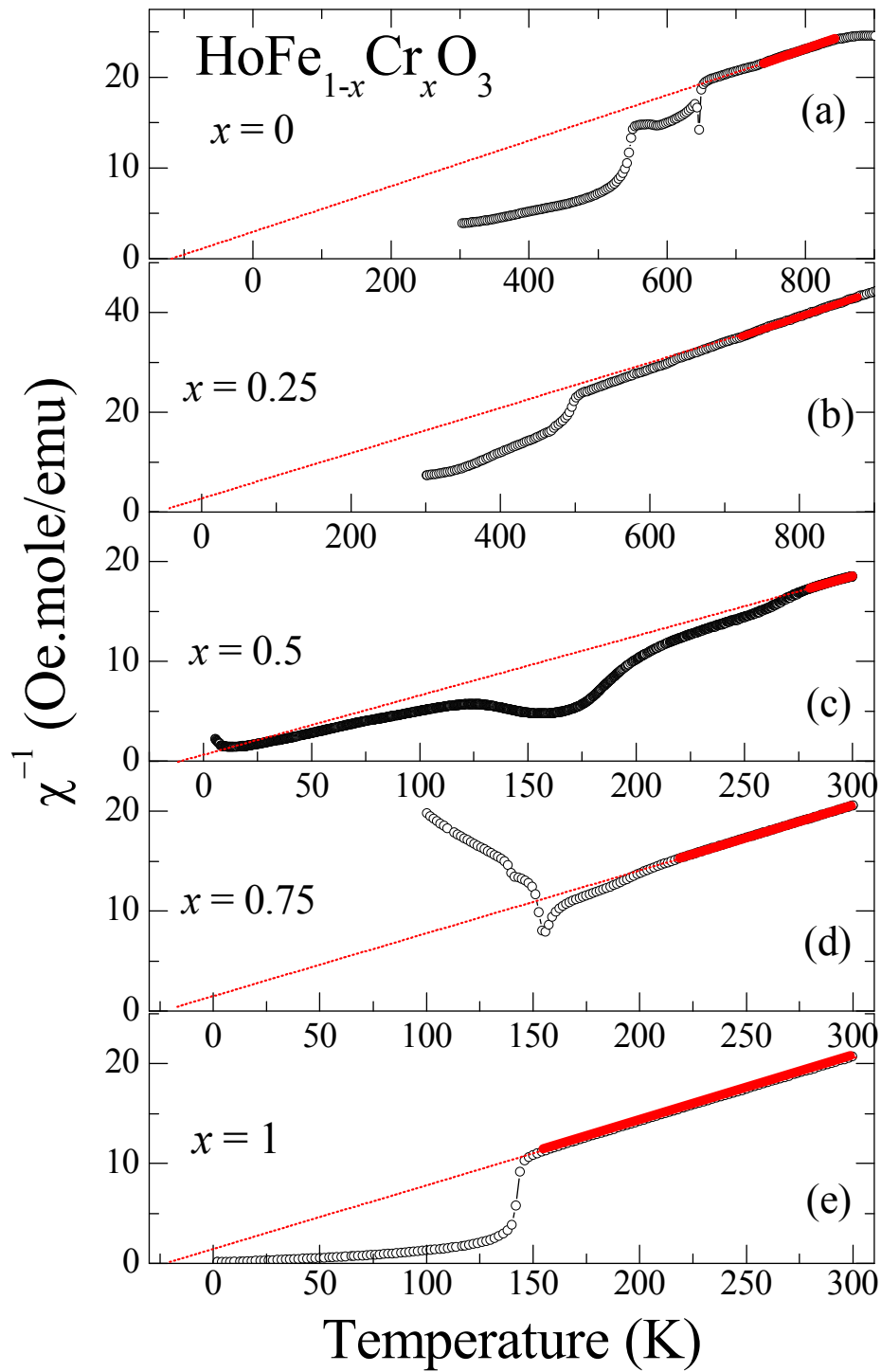


Figure 4.3: Temperature dependence of inverse molar susceptibility of $\text{HoFe}_{1-x}\text{Cr}_x\text{O}_3$ ($0 \leq x \leq 1$) compounds measured at 1000 Oe in the range of 5 – 300 K. Small dots represents the best fit of Curie-Weiss law.

Table 4.1: Effective magnetic moment μ_{eff} , paramagnetic Curie temperature θ of $\text{HoFe}_{1-x}\text{Cr}_x\text{O}_3$ ($0 \leq x \leq 1$) compounds obtained from the best fit of χ^{-1} vs. T by Curie-Weiss law.

Compound	μ_{eff} (experimental)	μ_{theory} (theoretical)	Paramagnetic curie temperature (θ)
$\text{HoFe}_{1-x}\text{Cr}_x\text{O}_3$	(μ_B)	(μ_B)	(K)
$x = 0$	16.59	12.14	-118.5
$x = 0.25$	11.80	11.93	-41
$x = 0.5$	11.62	11.72	-10
$x = 0.75$	11.15	11.50	-16.84
$x = 1$	11.13	11.28	-19

The possible reason can be explained as follows. In HoFeO_3 , the energy levels related with Ho^{3+} ions lie in the orthorhombic crystal field and molecular field formed by the sublattices of Fe^{3+} and Ho^{3+} ions. The degeneracy of the ground state multiplet $^5\text{I}_8$ of free non-Kramer Ho^{3+} ion essentially be lifted by the crystalline field and gives various singlets states. In particular, it has been observed that the ground state singlets (accidental doublet) are isolated from the other crystal field splitting states with an energy difference of more than 80 cm^{-1} [172]. Highly anisotropic nature of g-factor pertinent to accidental doublet states would play a predominant role in the magnetism of Ho^{3+} in HoFeO_3 and the same has been well demonstrated by Griffith [173]. It also has been established that at low temperatures in case of HoFeO_3 , aforementioned anisotropic nature of g – factor leads to an ‘Ising’ axis for the Ho^{3+} moments in the ab-plane at an angle $\pm 63^\circ$ with respect to the orthorhombic a-axis [174]. Thus a magnetic field parallel to ab - plane will split (Zeeman splitting) the accidental doublet and increases the energy of the system. Hence, the origin of SR transition in HoFeO_3 can be discussed on the basis of minimum energy configuration of spins which involves the complex magnetic interactions. Essentially, SR transition occurs due to the transformation of the high temperature Γ_4 ($G_x A_y F_z$) phase [high energy due to Zeeman splitting of accidental doublet] to Γ_2 ($F_x C_y G_z$) phase [low energy due to rotation of Fe^{3+} moments towards c – axis by 90°] at low temperatures. As a result of $\Gamma_4 \rightarrow \Gamma_2$ phase transition, we do see a SR transition in HoFeO_3 compound at around 50 K. On the other hand, the SR transition strongly depends on the exchange interaction strength of Ho-Fe(Cr) and Fe(Cr)-Fe(Cr). We do see an increase in T_{SR} with Cr^{3+} composition. We believe that as we substitute Cr^{3+} to Fe^{3+} , $\text{Fe}^{3+} - \text{Fe}^{3+}$ exchange interaction diminishes and $\text{Ho}^{3+} - \text{Fe}^{3+}$ interaction enhances, which may lead to enhanced T_{SR} with Cr^{3+} addition.

In addition to the AFM and SR transitions, we also could see a transition at low temperatures for $x = 0.25$ (8.5 K), $x = 0.5$ (13 K) and $x = 1$ (8 K) compounds, which can be attributed to Ho^{3+} ordering (Fig. 4.1 (b)) [175]. χ behaviour for $x = 0.75$ is quite different and the “diamagnetism” like negative magnetization is

observed. Earlier, negative magnetization has been observed in the HoCrO_3 compound for a cooling field of 100 Oe, however, such behaviour is absent for 1000 Oe. This intriguing phenomenon has been explained on the basis of competing WFM-AFM interactions [176]. In contrast, negative magnetization has been reported in ferro/ferri/antiferromagnetic materials and such fascinating phenomena has been explained on the basis of small negative trapping fields in the sample space [177]. Nevertheless, neutron diffraction data on $\text{HoFe}_{1-x}\text{Cr}_x\text{O}_3$ solid solutions reveal no signature of negative magnetization [178]. Hence, we believe that the observed negative magnetization for $x = 0.75$ compound could be due to trapped fields.

To investigate the paramagnetic behaviour of $\text{HoFe}_{1-x}\text{Cr}_x\text{O}_3$ compounds, we have plotted $1/\chi$ vs. T from the ZFC magnetization curves. Figure 4.3 depicts the temperature dependence of inverse susceptibility obtained for $\text{HoFe}_{1-x}\text{Cr}_x\text{O}_3$ ($0 \leq x \leq 1$) compounds. From Fig. 4.3, almost the linear behaviour is evident for the inverse molar magnetic susceptibility above the T_N . The total effective magnetic moment μ_{eff} of $\text{HoFe}_{1-x}\text{Cr}_x\text{O}_3$ compounds is obtained by fitting the paramagnetic region of χ^{-1} vs. T to Curie-Weiss law:

$$\chi = \frac{C}{T - \theta} \quad \text{..... (4.2)}$$

where $C = \frac{N_A \mu_{\text{eff}}^2}{3k_B}$ is Curie constant, N_A is the Avogadro's number, μ_B is the Bohr magneton, μ_{eff} is the effective magnetic moment, k_B is the Boltzmann constant and θ is the paramagnetic Weiss temperature.

After fitting the linear region above T_N with equation 4.2, from the slope μ_{eff} is obtained and is found to be 16.59 μ_B , 11.80 μ_B , 11.62 μ_B , 11.15 μ_B , 11.13 μ_B for $x = 0, 0.25, 0.5, 0.75$ and 1 compounds respectively. Except for the compound with $x = 0$, the estimated value of μ_{eff} is found to be close to the theoretical values 11.93 μ_B ($x = 0.25$), 11.72 μ_B ($x = 0.5$), 11.50 μ_B ($x = 0.75$), 11.28 μ_B ($x = 1$) which are calculated from the free ion values of Ho^{3+} (10.60 μ_B), Fe^{3+} (5.92 μ_B) and

Cr³⁺ (3.87 μ_B) (spin only values of Fe³⁺ and Cr³⁺) using the relation [177/179] $\mu_{theory} = [\mu_{Ho^{3+}}^2 + (1-x)\mu_{Fe^{3+}}^2 + x\mu_{Cr^{3+}}^2]^{1/2}$ and by assuming their randomness in the paramagnetic phase. The equation $\mu_{Fe^{3+}/Cr^{3+}} = 2[S(S+1)]^{1/2}$ is used to calculate $\mu_{Fe^{3+}}/\mu_{Cr^{3+}}$ moments and the formula $\mu_{Ho^{3+}} = |g_J|[J(J+1)]^{1/2}$ is used to calculate $\mu_{Ho^{3+}}$ moments. In the above equations S is the spin state of $\mu_{Fe^{3+}}/\mu_{Cr^{3+}}$ and J represents the total angular momentum and g_J represents the Landè g-factor respectively. The large value of $\mu_{eff} = 16.59 \mu_B$ for $x = 0$ compared to its theoretical value 12.14 μ_B can be ascribed to the secondary iron garnet (Ho₃Fe₅O₁₂) phase formed along with the parent HoFeO₃ phase. For all the compounds, the paramagnetic Curie temperature (θ) is estimated by extrapolating the high temperature linear region of $1/\chi$ vs. T graph to x - axis and it is found to be negative as shown in Table 4.1. According to Goodenough-Kanamori rule [39, 41], in order to observe FM ground state in HoFe_{1-x}Cr_xO₃ compounds, interaction between Fe³⁺ and Cr³⁺ should be of type Fe³⁺ (d^5) - O - Cr³⁺ (d^3) - O - Fe³⁺ (d^5). However, from $1/\chi$ vs. T graph, we do observe negative values for θ , which suggests AFM ground state. Hence, we believe that Fe³⁺ - O - Fe³⁺, Cr³⁺ - O - Cr³⁺ and Fe³⁺ - O - Cr³⁺ superexchange interactions are present at B - site [180-181].

It has been reported that the magnetic properties of orthoferrites depend on the oxidation state as well as the spin configuration of the transition metal cations [182]. Brinks et al. [183] observed a decrease in the T_N in Pr_{1-x}Sr_xFeO₃ compounds due to an enhancement in the oxidation state of Fe from Fe³⁺ to Fe⁴⁺. In our present investigation, T_N decreases with Cr³⁺ in HoFe_{1-x}Cr_xO₃ compounds from 647 K ($x = 0$) to 142 K ($x = 1$). In general, the variation of T_N could be due to (a) structural distortion (b) change in oxidation state. From our phase purity investigation, structural distortions have been realized in HoFe_{1-x}Cr_xO₃ compounds. However, the oxidation state of Fe in the present compounds is ambiguous. In this scenario, it is essential to know the knowledge of oxidation state of the transition metal, and its implications on the magnetic properties of HoFe_{1-x}Cr_xO₃ compounds.

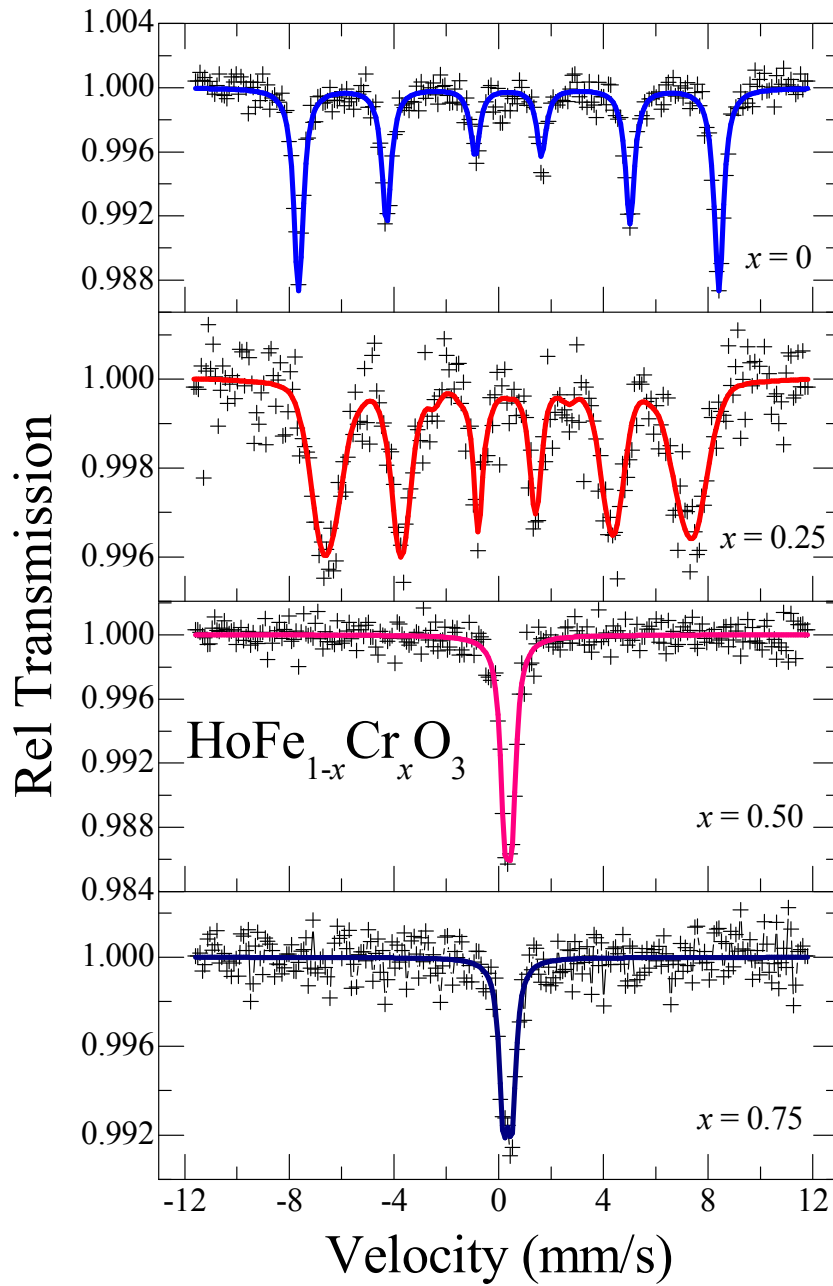


Figure 4.4: Room temperature ^{57}Fe Mössbauer spectrum of polycrystalline $\text{HoFe}_{1-x}\text{Cr}_x\text{O}_3$ ($0 \leq x \leq 1$) compounds. The experimental data is represented by the plus “+” symbol and the solid line is the best fit of the data.

Table 4.2: Parameters obtained from Mössbauer spectroscopy for $\text{HoFe}_{1-x}\text{Cr}_x\text{O}_3$ ($0 \leq x \leq 1$) compounds at 300 K.

compound $\text{HoFe}_{1-x}\text{Cr}_x\text{O}_3$	FWHM (mm/s)	IS (mm/s)	QS (mm/s)	H_{hf} (kOe)
$x = 0$	0.430 ± 0.018	0.373 ± 0.005	0.015 ± 0.010	497.6 ± 0.4
$x = 0.25$	0.45	--	--	415.3 (Avg)
$x = 0.50$	0.408 ± 0.019	0.368 ± 0.009	0.26 ± 0.01	---
$x = 0.75$	0.388 ± 0.049	0.342 ± 0.018	0.32 ± 0.03	---

Hence, we performed ^{57}Fe Mössbauer spectroscopy measurements on $\text{HoFe}_{1-x}\text{Cr}_x\text{O}_3$ compounds. Figure 4.4 depicts the room temperature ^{57}Fe Mössbauer measurements carried out on polycrystalline $\text{HoFe}_{1-x}\text{Cr}_x\text{O}_3$ ($0 \leq x \leq 1$) compounds. Experimentally recorded data is represented by the plus “+” symbol, while the least square fit of the spectrum is represented by a solid line. At 300 K, fitting results indicates a single sextet for $x = 0$ compound while doublet for $x = 0.5$ and 0.75 compounds respectively. Since the hyperfine field of the garnet $\text{Ho}_3\text{Fe}_5\text{O}_{12}$ [184] and the parent compound HoFeO_3 are very close, we are not able to fit the Mössbauer data with garnet phase which is only about 5-6%. On the other hand, distribution of fields match reasonably well with experimental data points in the case of $x = 0.25$ compound with an average hyperfine field value of 415.3 kOe. The fitted parameters are listed in the Table 4.2. Oxidation state of ‘+3’ for Fe in HoFeO_3 is confirmed by realizing the six line spectra and corresponding values pertinent to hyperfine field (H_{hf}), isomer shift (IS) and quadrupole splitting (QS) are 497.6 kOe, 0.373 mm/s and 0.015 mm/s respectively.

Indeed, observed H_{hf} , IS and QS are within the range for an element to have ‘+3’ oxidation state and is in accordance with the literature [185]. Since there is no change in oxidation state, we believe that variation of T_N in $\text{HoFe}_{1-x}\text{Cr}_x\text{O}_3$ ($0 \leq x \leq 1$) compounds is due to structural distortion.

In general H_{hf} , IS and QS are very crucial and sensitive for a change in local environment of Fe^{3+} particularly in orthoferrites. In the present work, we modified the local environment of Fe^{3+} by substituting Cr^{3+} . In subsequent section, we discuss about the variation of H_{hf} , IS and QS parameters and related physical mechanism with Cr^{3+} addition in $\text{HoFe}_{1-x}\text{Cr}_x\text{O}_3$ compounds at 300 K.

From Table 4.2 it is evident that IS decreases with Cr^{3+} . The decrease in IS is due to decrease in radial part of $3d$ wave function with Cr^{3+} substitution [186]. On the other hand, quadrupole splitting is a parameter which gives the information about the lifting of the degeneracy of a nuclear state with $I > \frac{1}{2}$ by experiencing the electric field gradient (EFG) due to its interaction with an asymmetric electronic

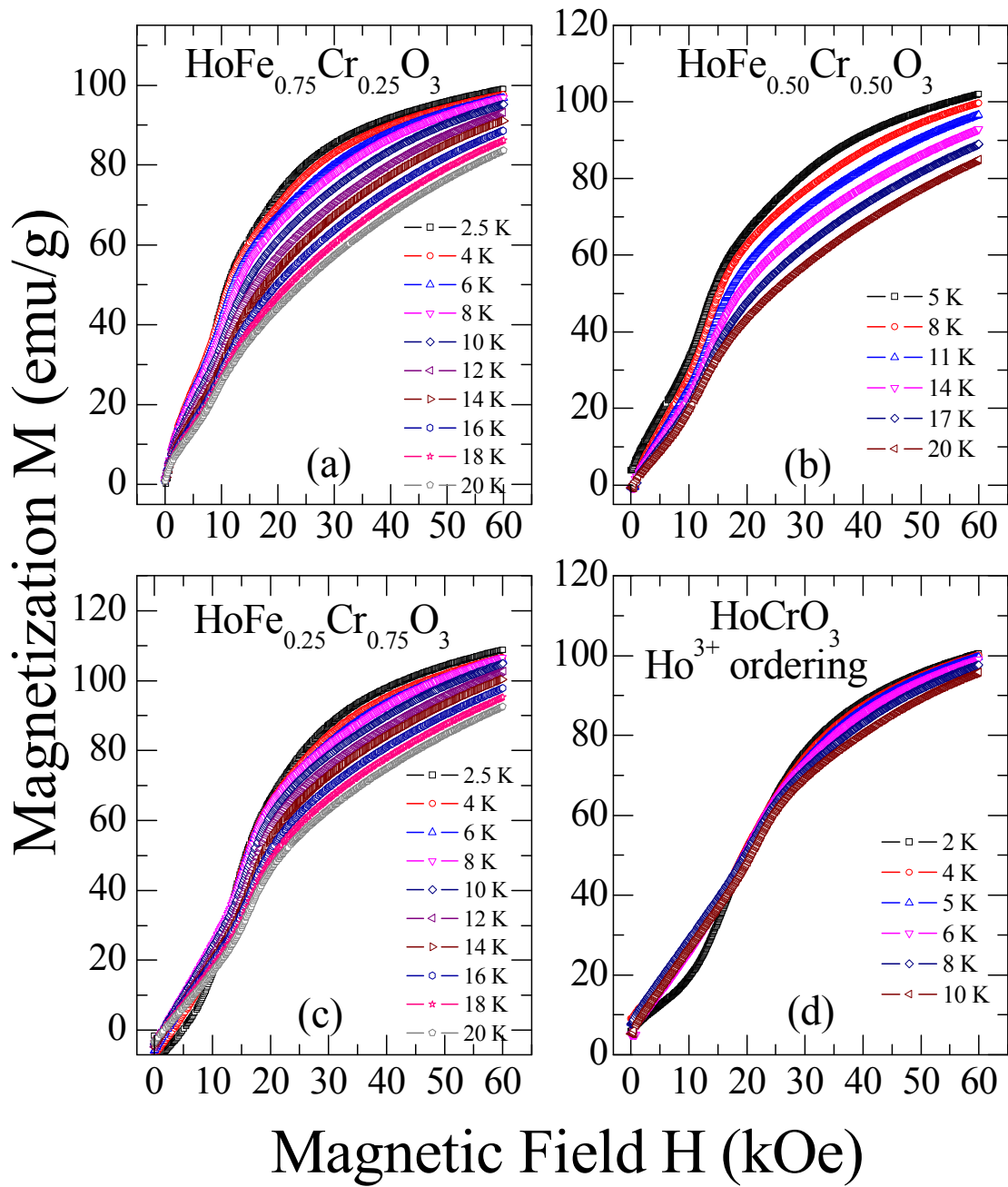


Figure 4.5: (a – d) First quadrant magnetization isotherms around Ho^{3+} ordering temperature with an applied field up to 60 kOe for $\text{HoFe}_{1-x}\text{Cr}_x\text{O}_3$ ($0.25 \leq x \leq 1$) compounds.

environment surrounding to it. The small value of QS ~ 0.015 mm/s observed for HoFeO₃ suggests that Fe is almost in octahedral environment (cubic electric field gradient) [187]. The value of QS increases with an increase in Cr composition, and is quite appreciable for $x \geq 0.5$ compounds. This increase in QS may be ascribed to the distortion in FeO₆ octahedra by substituting Cr³⁺ ions at Fe site, due to which the Fe atom experience a non-cubic electric field and leads to an increase in QS.

The six resonance lines observed in Mössbauer spectrum for HoFeO₃ at room temperature indicates that the Fe³⁺ ions experience an internal magnetic field. It has been reported that HoFeO₃ is antiferromagnetically ordered below 641 K [76]. In orthoferrites, antiferromagnetically aligned iron ions with small canting angle with respect to the AFM axis results a small net ferromagnetic moment. The value of the calculated hyperfine field (H_{hf}) for HoFeO₃ at room temperature is 497.6 kOe (typical value for Fe³⁺ ion), which is in agreement with previously reported value [185]. With an increase in the concentration of Cr³⁺, the strength of AFM interaction decreases, resulting in a decrease of the internal magnetic field experienced by the Fe³⁺ ion at 300 K. As the compounds with composition $x \geq 0.5$ consists ordering temperatures below 300 K, disappearance of six line spectra is evident which may be due to vanishing of internal magnetic fields at 300 K.

4.3 Magnetocaloric properties and nature of magnetic phase transition

As there are multiple transitions in HoFe_{1-x}Cr_xO₃ ($0 \leq x \leq 1$) compounds, we do expect a large change in entropy around these transitions. Hence, in order to quantify change in entropy we performed M vs. H measurements in the vicinity of the magnetic transitions pertinent to HoFe_{1-x}Cr_xO₃ ($0.25 \leq x \leq 1$) compounds. We have excluded HoFeO₃ compound in this study as it consists a secondary iron garnet phase (Ho₃Fe₅O₁₂).

Figure 4.5 (a - d) shows first quadrant magnetization isotherms corresponding to HoFe_{1-x}Cr_xO₃ ($0.25 \leq x \leq 1$) compounds recorded around Ho³⁺ ordering with a maximum magnetic field of 60 kOe. A field induced metamagnetic transition is evident in the low magnetic field region for all M vs. H graphs as shown in Fig. 4.5 (a - d). Now we define the critical field (H_C) of metamagnetic transition as field

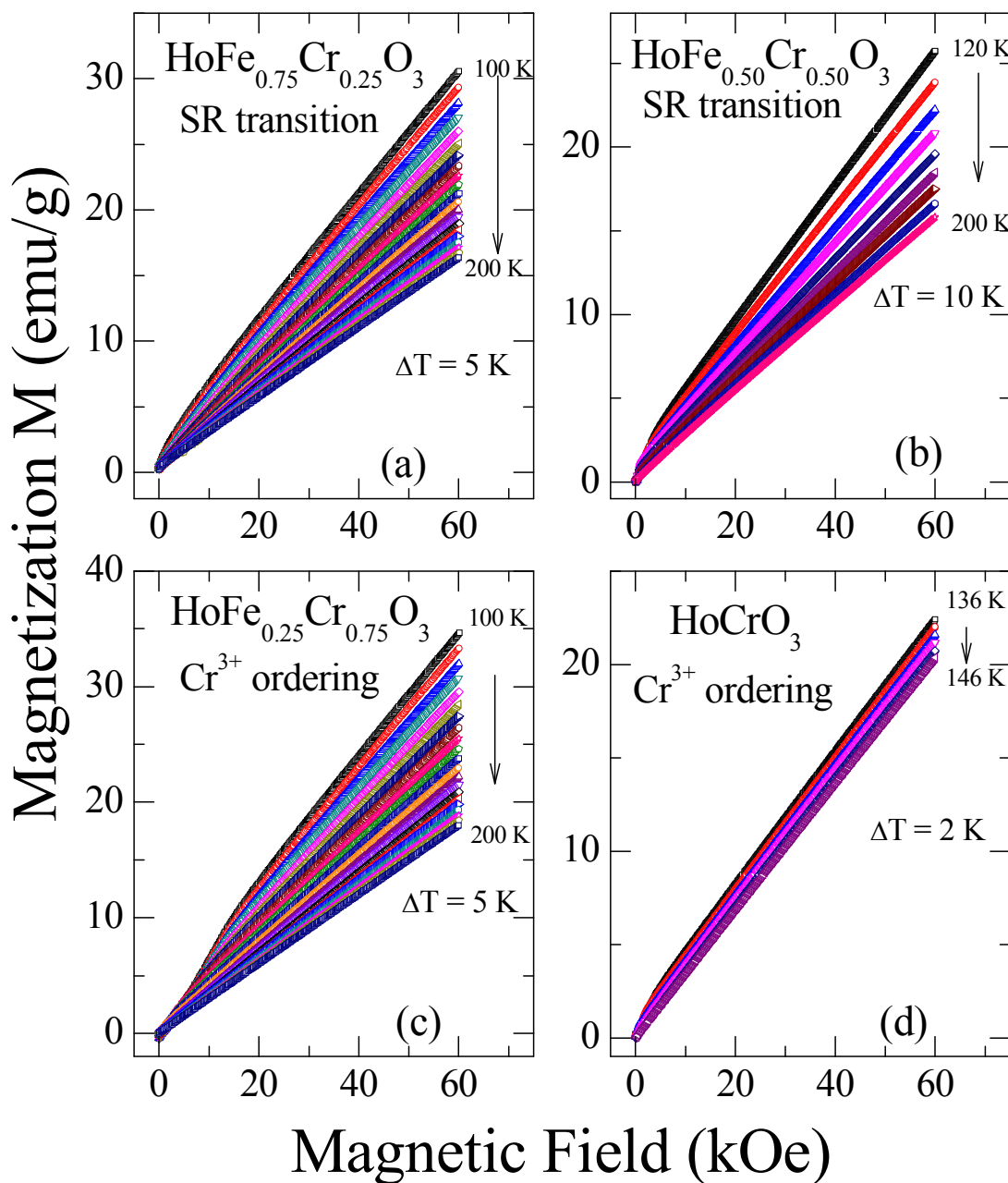


Figure 4.6: First quadrant magnetization isotherms around (a – b) SR transition related to $x = 0.25$ and $x = 0.50$ compounds, (c – d) Cr^{3+} ordering temperature pertinent to $x = 0.75$ and $x = 1$ compounds with an applied field up to 60 kOe for $\text{HoFe}_{1-x}\text{Cr}_x\text{O}_3$ ($0.25 \leq x \leq 1$) compounds.

below which the material shows AFM behaviour and exhibits ferromagnetic (FM) behaviour above this field. Such a field induced transition in low field region can be ascribed to the onset of a first order metamagnetic transition (from original AFM state to FM state). Evidenced metamagnetic transition may be due to the magnetization reversal of those ions whose magnetic moments are directed opposite to the applied magnetic field and the similar behaviour has been observed in the single crystals of DyCrO₃ as the rotation of Dy³⁺ and Cr³⁺ moments [188]. From Fig. 4.5 (c) and Fig. 4.5 (d), it is evident that there is a magnetization crossover around the AFM→ FM transition, which can be ascribed as a result of the competition between the Zeeman energy due to the applied external field and the strong magneto-crystalline anisotropy energy around the metamagnetic transition [189].

Figure 4.6 (a – b) shows the first quadrant isothermal magnetization curves (M vs. H) around the spin reorientation transition corresponding $x = 0.25$ and $x = 0.50$ compounds, whereas Fig. 4.6 (c – d) represents M vs. H curves around T_N (Cr³⁺ ordering) in $x = 0.75$ and $x = 1$ compounds. It is evident from the Fig. 4.6 (c – d) that low field nonlinearity is due to weak ferromagnetic (WFM) component which arises due to canting of Cr³⁺ moments. Apart from that, an increase in linearity of M vs. H curves is evident with an increase in temperature from 100 K up to T_N (155 K for $x = 0.75$ and 142 K for $x = 1$ compound) due to decrease in strength of WFM component. The disappearance of nonlinearity for M vs. H curves above T_N indicates the paramagnetic phase.

As there are multiple transitions in HoFe_{1-x}Cr_xO₃ ($0.25 \leq x \leq 1$) compounds, we do expect a large change in entropy around these transitions. Hence, we calculated magnetic entropy change ($-\Delta S_M$) from isothermal magnetization curves using well known Maxwell's equation as follows

$$\Delta S_M(T, H) = \int_0^{H_{\max}} \left(\frac{\partial M}{\partial T} \right)_H dH \quad \dots (4.3)$$

where H_{\max} is the maximum value of external applied field. From the above equation 4.3, it can be noticed that the value of $-\Delta S_M$ depends on both the values of magnetization (M) and $\left(\frac{\partial M}{\partial T}\right)_H$. The larger values of $-\Delta S_M$ can be obtained when the values of M and $\left(\frac{\partial M}{\partial T}\right)_H$ are large in the magnitude [190].

Quantified values of $-\Delta S_M$ at various magnetic transitions in $\text{HoFe}_{1-x}\text{Cr}_x\text{O}_3$ ($0.25 \leq x \leq 1$) compounds and its temperature variation is shown in Fig. 4.7 (a – d) and Fig. 4.8 (a – d). Here, Fig. 4.7 (a – d) depicts the $-\Delta S_M$ vs. T around Ho^{3+} ordering for $\text{HoFe}_{0.75}\text{Cr}_{0.25}\text{O}_3$ ($-\Delta S_M \sim 8.63$ J/kg-K at 9 K), $\text{HoFe}_{0.5}\text{Cr}_{0.5}\text{O}_3$ ($-\Delta S_M \sim 8.18$ J/kg-K at 12.5 K), $\text{HoFe}_{0.25}\text{Cr}_{0.75}\text{O}_3$ ($-\Delta S_M \sim 8.08$ J/kg-K at 11 K) and HoCrO_3 ($-\Delta S_M \sim 6.99$ J/kg-K at 9 K) compounds respectively with a maximum magnetic field of 60 kOe. Large values of $-\Delta S_M$ in all the compounds can be ascribed to evidenced metamagnetic transition and the Ho^{3+} ordering. Reason for the enhancement in the value of $-\Delta S_M$ in $\text{HoFe}_{0.75}\text{Cr}_{0.25}\text{O}_3$ compound compared to that of the HoCrO_3 compound can be explained as follows. Essentially, HoCrO_3 is distorted type perovskite material and crystallizes in orthorhombic structure with a space group of Pbnm [191]. For an ideal perovskite Cr-O1-Cr bond angle must be 180° . However, due to the distortion as a result of tilting of CrO_6 octahedra in HoCrO_3 , there would be a change in Cr-O1-Cr bond angle (146.2°) [in the present study from refinement], which is distinctly different from an ideal perovskite. This distortion decreases the orbital overlap and leads to non collinear antiferromagnetic structure of Cr^{3+} ions with a weak ferromagnetic component. Obtained bond angle value from Rietveld refinement pertinent to Fe(Cr)-O1-Fe(Cr) is smaller for $\text{HoFe}_{0.75}\text{Cr}_{0.25}\text{O}_3$ (144.0°) in comparison with the HoCrO_3 (146.2°) compound. This indicates an increase in canting of spins and hence an enhancement in $-\Delta S_M$ value for $\text{HoFe}_{0.75}\text{Cr}_{0.25}\text{O}_3$ compound in comparison with HoCrO_3 . The increase in canting angle of $\text{Fe}^{3+}/\text{Cr}^{3+}$ sublattice with AFM axis for $\text{HoFe}_{0.75}\text{Cr}_{0.25}\text{O}_3$ has been evident from the neutron diffraction data on $\text{HoFe}_{1-x}\text{Cr}_x\text{O}_3$ solid solutions [178].

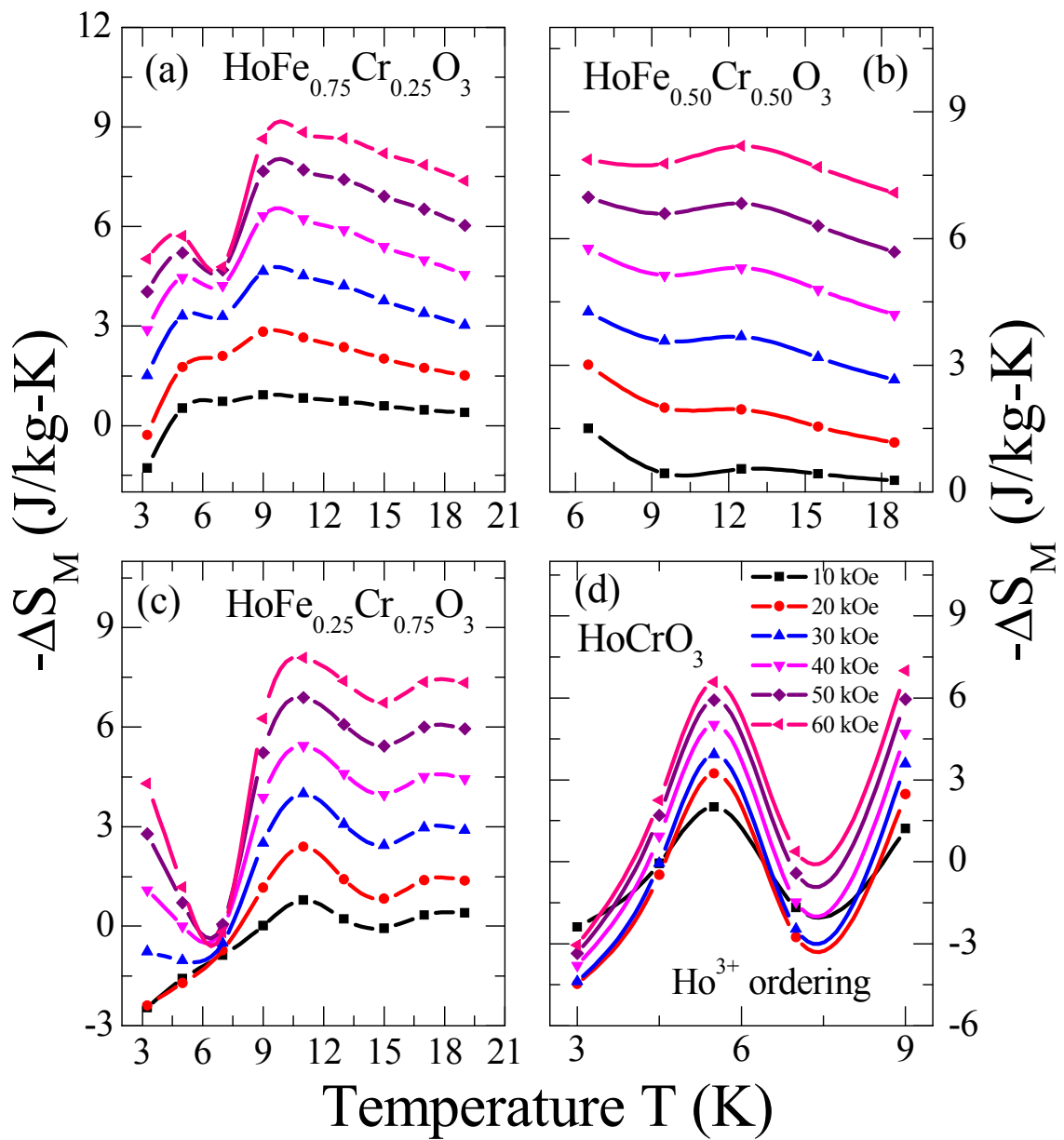


Figure 4.7 : (a – d) Temperature dependence of the magnetic entropy $-\Delta S_M$ obtained from isothermal M vs. H data corresponding to Fig. 4.5 (a – d) for $\text{HoFe}_{1-x}\text{Cr}_x\text{O}_3$ ($0.25 \leq x \leq 1$) compounds.

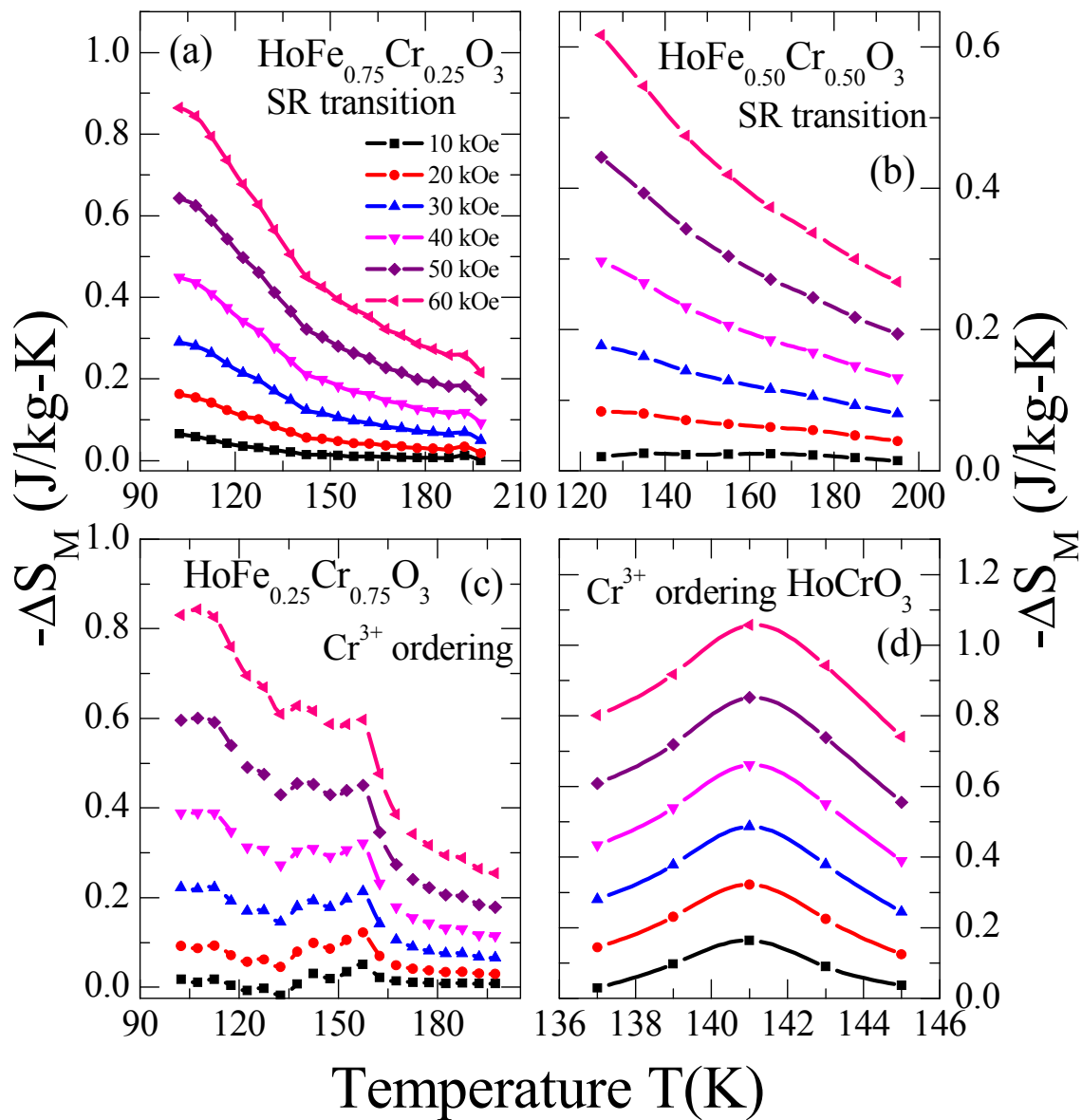


Figure 4.8: (a – d) Temperature dependence of the magnetic entropy $-\Delta S_M$ obtained from isothermal M vs. H data corresponding to Fig. 4.6 (a – d) for $\text{HoFe}_{1-x}\text{Cr}_x\text{O}_3$ ($0.25 \leq x \leq 1$) compounds.

The values of MCE obtained for $\text{HoFe}_{1-x}\text{Cr}_x\text{O}_3$ ($0.25 \leq x \leq 1$) compounds in the vicinity of Ho^{3+} ordering temperature are large when compared to DyMnO_3 ($-\Delta S_M \sim 6.8$ J/kg-K at 7 T and 10 K) [192], $\text{SmFe}_{0.5}\text{Mn}_{0.5}\text{O}_3$ (5.6 J/kg-K at 18 K and with 7 T) [193] and $\text{HoFe}_{0.3}\text{Cr}_{0.7}\text{O}_3$ (6.83 J/kg-K at 20 K and with 7 T) [194]. However, the values of $-\Delta S_M$ obtained in the present study are smaller compared to giant MCE material such as TmZn [195], ErMn_2Si_2 [196], $\text{Tm}_2\text{Cu}_2\text{In}$ [197], HoPdIn [198] and $\text{RE}_2\text{Cu}_2\text{O}_5$ (RE = Dy and Ho) [199] in the low temperature region.

From the Fig. 4.7 (a), Fig. 4.7(c) and Fig. 4.7(d), it is evident that $-\Delta S_M$ values shows both positive and negative values as though there exists re-entrant magnetocaloric effect. Such an unusual nature of re-entrant inverse MCE in $\text{HoFe}_{0.3}\text{Cr}_{0.7}\text{O}_3$ [194] as well as un-doped HoCrO_3 [200] compound has been not observed earlier. The reason for such an intriguing phenomenon may be due to the subtle changes in relative orientations of Ho^{3+} and $\text{Fe}^{3+}/\text{Cr}^{3+}$ moments occurs with a variation of temperature and/or magnetic field [201]. Earlier inverse magnetocaloric effect has been observed around SR transition in single crystals of HoFeO_3 [128]. We conceive from our observation that magnetization crossover and complex interaction between FM and AFM phases might be a reason for re-entrant MCE behaviour in the present compound.

Figure 4.8 (a) and Fig. 4.8 (b) depicts $-\Delta S_M$ vs. T around SR transition for $\text{HoFe}_{0.75}\text{Cr}_{0.25}\text{O}_3$ ($-\Delta S_M \sim 0.86$ J/kg-K at 102.5 K), $\text{HoCr}_{0.5}\text{Fe}_{0.5}\text{O}_3$ ($-\Delta S_M \sim 0.61$ J/kg-K at 125 K) compounds respectively with a magnetic field of 60 kOe. On the other hand, Fig. 4.8 (c) and Fig. 4.8 (d) depicts $-\Delta S_M$ vs. T around T_N (Cr^{3+} ordering) for $\text{HoFe}_{0.25}\text{Cr}_{0.75}\text{O}_3$ ($-\Delta S_M \sim 0.59$ J/kg-K at 157.5 K) and HoCrO_3 ($-\Delta S_M \sim 1.05$ J/kg-K at 141 K) compounds respectively at a maximum magnetic field of 60 kOe. The value of $-\Delta S_M \sim 0.85$ J/kg-K at T_N with 50 kOe pertinent to HoCrO_3 compound is large compared to other orthochromites such as YbCrO_3 (0.41 J/kg-K) [202], YCrO_3 (0.36 J/kg-K) [202] and SmCrO_3 (0.15 J/kg-K) [202]. A maximum $-\Delta S_M$ value of 0.84 J/kg-K is obtained at around 107.5 K, which is below T_N with a magnetic field of 60 kOe in $\text{HoFe}_{0.25}\text{Cr}_{0.75}\text{O}_3$ compound. At Néel temperature, Cr^{3+} moments order antiferromagnetically. As the temperature goes below T_N , the

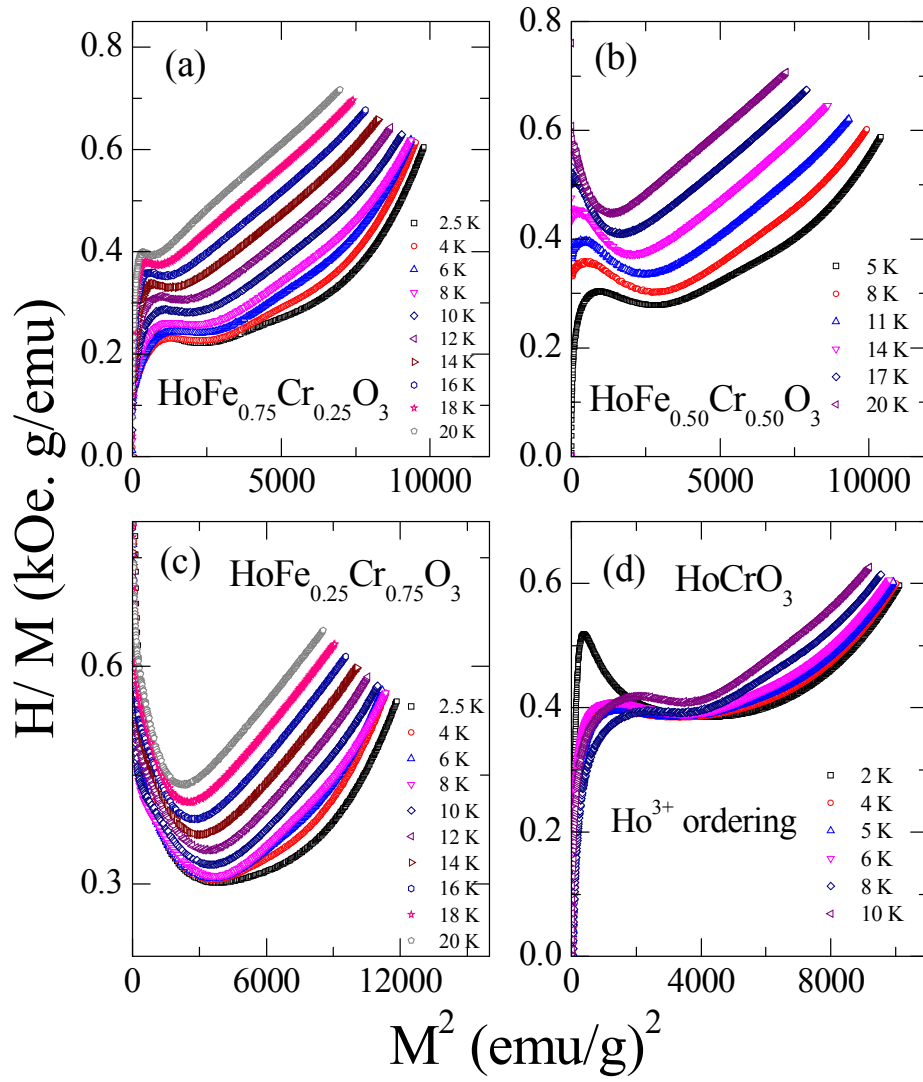


Figure 4.9: (a – d) Arrott plots deduced from magnetization isotherms corresponding to Fig. 4.5 (a – d) for $\text{HoFe}_{1-x}\text{Cr}_x\text{O}_3$ ($0.25 \leq x \leq 1$) compounds.

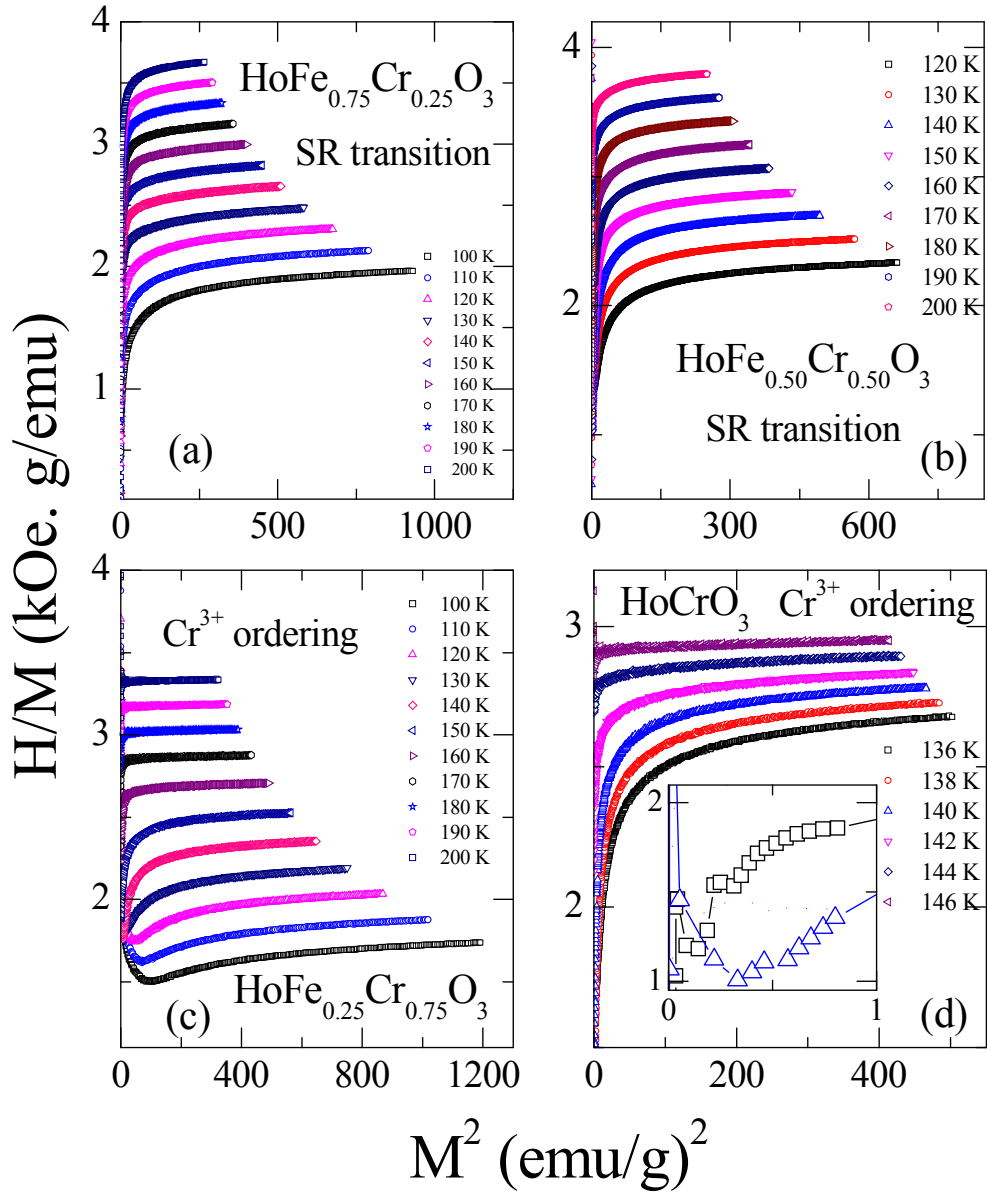


Figure 4.10: (a – d) Arrott plots deduced from magnetization isotherms corresponding to Fig. 4.6 (a – d) for $\text{HoFe}_{1-x}\text{Cr}_x\text{O}_3$ ($0.25 \leq x \leq 1$) compounds.

molecular field of Cr^{3+} moments will try to order the Ho^{3+} moments and thus the magnetization increases. This leads to an increase in magnetic entropy change up to ordering temperature of Ho^{3+} moments and reaches a maximum value.

It is believed that the magnitude of the magnetic entropy change at a particular magnetic phase transition and its dependence on temperature and magnetic field strongly depend upon the nature of the corresponding phase transition [203], hence, it is essential to determine the nature of magnetic phase transitions in these compounds. To do this, the first quadrant magnetization isotherms are plotted in the form of Arrott plots (H/M vs. M^2) [204], which can be deduced from Ginzburg-Landau theory in the close vicinity of the magnetic transition.

The thermodynamic potential with Ginzburg-Landau type expansion which includes the magnetostatic field energy (MH) near the magnetic transition is as follows:

$$G(T, M) = G_0 + \alpha M^2 + \beta M^4 + \dots - MH \quad \dots (4.4)$$

where α, β are the Landau coefficients dependent on temperature. In the equilibrium condition, $\frac{\partial G}{\partial M} = 0$, the equation 4.4 reduces to $\frac{H}{M} = \beta M^2 + \alpha$. According to Banerjee's criterion [205], a negative slope of H/M vs. M^2 at some point indicates the first order magnetic transition. On the other hand a positive slope of H/M vs. M^2 indicates the second order magnetic transition.

Figure 4.9 (a – d) and Fig. 4.10 (a – d) shows the Arrott plots corresponding to magnetization isotherms shown in Fig. 4.5 (a – d) and Fig. 4.6 (a – d) respectively. The negative slope of H/M vs. M^2 for the Fig. 4.9 (a – d) corresponding to $\text{HoFe}_{1-x}\text{Cr}_x\text{O}_3$ ($0.25 \leq x \leq 1$) compounds indicates that the Ho^{3+} ordering is a first order magnetic phase transition. The positive slope of H/M vs. M^2 for Fig. 4.10 (a) and Fig. 4.10 (b) corresponding to $x = 0.25$ and $x = 0.5$ compounds indicates the spin reorientation transition is a second order magnetic phase transition which is in agreement with the literature [206]. On the other hand, the negative slope of Arrott plot for the Fig. 4.10 (c) and Fig. 4.10 (d) related to $x = 0.75$ and $x = 1$ compounds

indicating that the Cr^{3+} ordering (AFM transition) is a first order magnetic phase transition.

4.4 Specific heat studies on $\text{HoFe}_{0.25}\text{Cr}_{0.75}\text{O}_3$ compound

As discussed in introduction chapter, a magnetic material with a large change of magnetic entropy $\Delta S_M(T, H)$, adiabatic temperature change (ΔT_{ad}) and a sufficiently large value of refrigeration capacity (RC) has been promising candidate for magnetic refrigeration [100/101]. The perovskite oxides with a general formula ABO_3 have been studied for the MCE properties using three methods, (a) calculation of $-\Delta S_M$ from the isothermal magnetization using Maxwell's relation [207-208] (b) heat capacity C_p measurements [209-211] and (c) direct measurement of the adiabatic temperature change by exposing thermally insulated sample to the magnetic field [212-214]. Magnetic contribution to the specific heat (C_p) can be obtained from the total C_p after subtracting the electronic and phonon contribution [215]. In general, the materials with smaller C_p values are desirable for the refrigeration application as ΔT_{ad} is inversely proportional to C_p [216]. Rare earth orthochromites with chemical formula RCrO_3 , show smaller C_p values (~ 95 - 109 J/mol-K) and consequently larger ΔT_{ad} values, these compounds have been of great interest for the MCE applications [210]. In the present thesis, we have studied the specific heat studies of $\text{HoFe}_{0.25}\text{Cr}_{0.75}\text{O}_3$ compound.

The variation of the specific heat (C_p) of $\text{HoFe}_{0.25}\text{Cr}_{0.75}\text{O}_3$ compound in the temperature range between 100 - 200 K was recorded with zero magnetic field and by varying magnetic field strengths of 30 kOe, 50 kOe and 70 kOe respectively (Fig. 4.11 (a)). The shape of C_p vs. T is generally consistent with the results of prior work on orthochromites such as NdCrO_3 [217] and YbCrO_3 [218]. It has been observed from the Fig. 4.11 (a) that C_p decreases with a decrease in temperature and a λ -shape anomaly is evident at around $T_N \sim 155$ K in the case of $\text{HoFe}_{0.25}\text{Cr}_{0.75}\text{O}_3$ compound. This anomaly is associated with a paramagnetic to canted antiferromagnetic (AFM) phase transition [175]. The value of C_p is found to be 83.8 J/mol-K at 200 K from the C_p vs. T data recorded under zero magnetic

field (0 Oe), which is almost equal to the reported value of C_p pertinent to HoCrO_3 (83.3 J/mol-K at 200 K) compound [210].

To extract the magnetic heat capacity C_{mag} pertinent to AFM ordering, a third order polynomial background is subtracted from the experimental C_p vs. T data which is obtained at 0 Oe in order to exclude the electron and phonon contribution as shown in Fig. 4.11 (b). Similar treatment is done for the data (C_p vs. T) under different magnetic field strengths of 30 kOe, 50 kOe and 70 kOe respectively. The excess heat capacity due to AFM transition at different magnetic fields (0 Oe, 30 kOe, 50 kOe and 70 kOe) in the temperature range between 100 - 200 K is plotted as C_{mag} vs. T and is presented in Fig. 4.11 (c). Significant change in the value of C_p (H, T) is not evident up to the maximum magnetic field of 70 kOe.

The magnetic heat capacity C_{mag}/T vs. T data at 0 Oe is used to calculate the magnetic entropy associated with magnetic transition using the equation

$$S_{\text{mag}} = \int_{T_1}^{T_2} \left(\frac{C_{\text{mag}}}{T} \right) dT \quad \dots\dots (4.5)$$

and is shown in Fig. 4.11 (d). The calculated S_{mag} is 1.21 J/mol-K and is well below the expected full spin entropy, $S_{\text{mag}} = R \ln(2S+1)$ where S (3/2) is the spin of Cr^{3+} ions in the compounds, and R is the molar gas constant.

It is well known that magnetic materials with large value of $-\Delta S_M$ and ΔT_{ad} are needed for refrigeration application [101]. It is well known that under adiabatic conditions magnetic material will cool down by inducing an adiabatic temperature change ΔT_{ad} . According to Maxwell's relation, ΔT_{ad} associated with magnetic transition and can be calculated using the following equation:

$$\Delta T_{\text{ad}} = - \int_0^H \frac{T}{C_p(T, H)} \left(\frac{\partial M}{\partial T} \right)_H dH = -\Delta S_M \left(\frac{T}{C_p(T, H)} \right) \quad \dots\dots (4.6)$$

where $-\Delta S_M$ is magnetic entropy change deduced from the isothermal magnetic measurements and C_p is the specific heat.

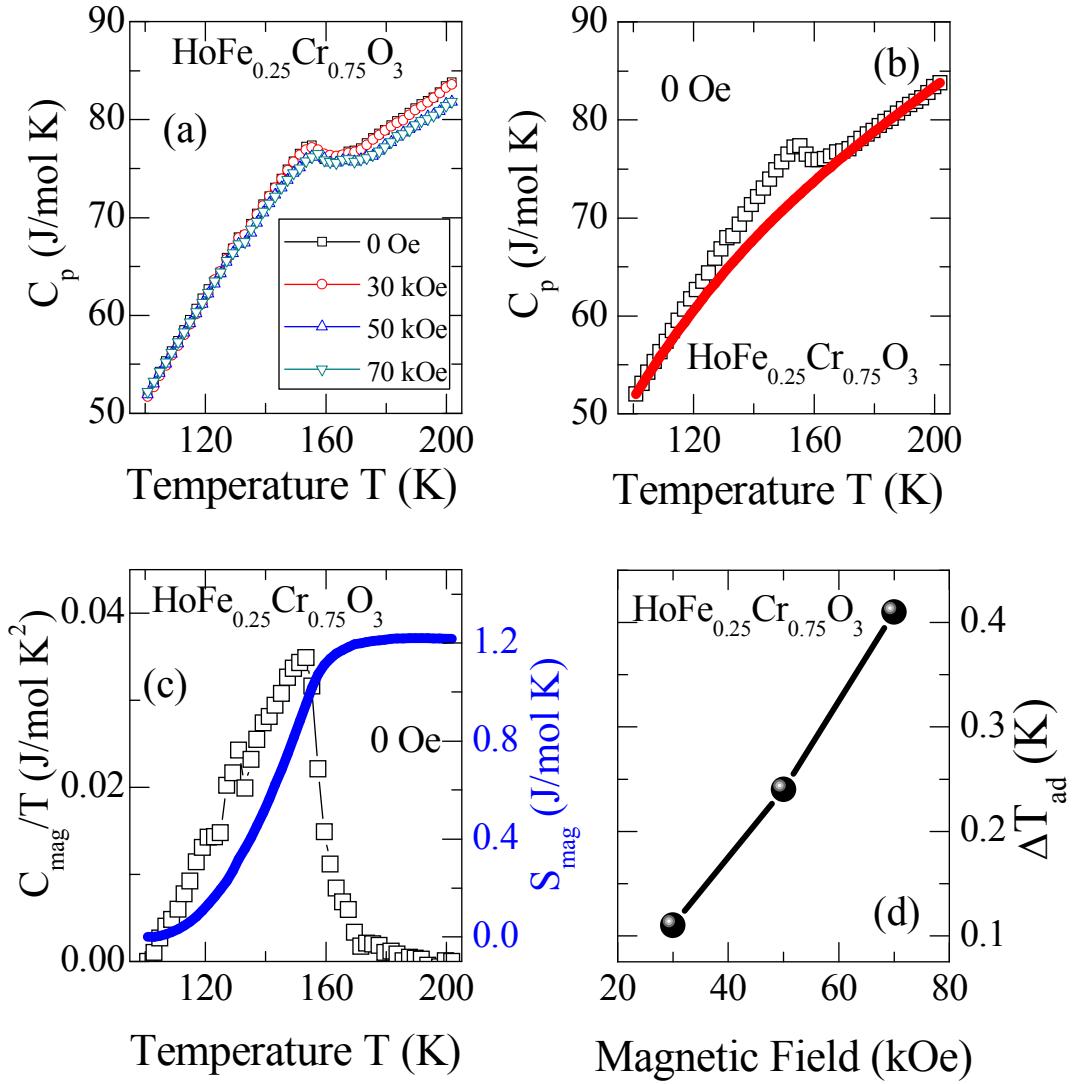


Figure 4.11: (a) Variation of specific heat C_p with temperature (T) at different magnetic fields (b) subtraction of phonon and electron contribution using third order polynomial from the specific heat data. Fitted data is shown as red line and experimental data is shown as black square symbol (c) variation of C_{mag}/T and S_{mag} with temperature (d) variation of adiabatic temperature change ΔT_{ad} with magnetic field for $\text{HoFe}_{0.25}\text{Cr}_{0.75}\text{O}_3$ compound.

According to equation 4.6, a large value of ΔT_{ad} can be expected to occur around PM - AFM transition since the rate of change of magnetization is large with temperature. However, the magnitude of C_p at that transition also plays a crucial role in determining the cooling efficiency of the material, as it varies significantly from one magnetocaloric material family to other. For example, the heat capacity of Gd-based alloy system is much smaller than that of a manganite type material system [84]. Therefore, a reliable comparison of the efficiency of different magnetocaloric materials should be based on evaluating ΔT_{ad} instead of $-\Delta S_M$. The variation of ΔT_{ad} with respect to the magnetic field (H) around AFM ordering (T_N) is shown in Fig. 4.11 (d). It is evident that the value of ΔT_{ad} increases with increase of applied magnetic field, and reaches a maximum value of 0.41 K around T_N . The value of ΔT_{ad} for the present compound (0.11 K at $T_N \sim 155$ K with 30 kOe) is found larger in comparison with SmCrO_3 ($\Delta T_{ad} = 0.03$ K at $T_N \sim 192$ K with 30 kOe) compound [219].

4.5 Conclusions

In summary, we have explored the magnetic, Mössbauer and magnetocaloric properties of polycrystalline $\text{HoFe}_{1-x}\text{Cr}_x\text{O}_3$ ($0 \leq x \leq 1$) compounds. A perfect correlation between the results of structural, magnetic and magnetocaloric properties are obtained. The observed decrease of T_N and increase of T_{SR} with Cr doping is attributed to the dilution of Ho^{3+} - Fe^{3+} and Fe^{3+} - Fe^{3+} interactions in the entire temperature region and the enhancement of ferromagnetic interaction of adjacent Cr^{3+} moments through t - e hybridization as a result of the structural distortion. The observed decrease in IS with Cr content infers the increase of the interaction between the effective nuclear charge with the 3s electrons. The small QS value observed for HoFeO_3 indicates the local environment remains octahedral at the unit cell. Increase in a value of QS with Cr doping is due to the non-cubical electric field gradient acting on Fe atom arising from the distortion in FeO_6 octahedra by substituting Cr^{3+} ions at Fe site. The decrease in hyperfine field was ascribed to a decrease in Fe^{3+} - Fe^{3+} AFM interaction with the addition of Cr. The disappearance of six line Mössbauer spectra for $x \geq 0.5$ infers the compounds are in

paramagnetic in nature at 300 K. M vs. H graph infer that the metamagnetic transitions are prevailed in the low field regime of M vs. H graph around Ho^{3+} ordering in $\text{HoFe}_{1-x}\text{Cr}_x\text{O}_3$ ($0.25 \leq x \leq 1$) compounds. Re-entrant magnetocaloric effect is evident in $\text{HoFe}_{1-x}\text{Cr}_x\text{O}_3$ (0.25, 0.75 and 1) compounds, which may be due to magnetization crossover and complex interactions. We trust that the large values of MCE obtained for $\text{HoFe}_{1-x}\text{Cr}_x\text{O}_3$ ($0.25 \leq x \leq 1$) compounds makes them promising candidates for magnetic refrigeration applications below 30 K.

Chapter 5

Spin-phonon coupling in $\text{HoCr}_{1-x}\text{Fe}_x\text{O}_3$ ($x = 0$ and 0.5) compounds

In this chapter we discuss about evidenced spin-phonon coupling in $\text{HoCr}_{1-x}\text{Fe}_x\text{O}_3$ compounds through temperature dependent Raman spectroscopy.

5.1 Experimental details

Polycrystalline $\text{HoCr}_{1-x}\text{Fe}_x\text{O}_3$ ($x = 0$ and 0.5) compounds were prepared by conventional solid state reaction route using high purity oxides of Ho_2O_3 , Fe_2O_3 and Cr_2O_3 as starting materials. Temperature dependent Raman spectra were recorded with a LabRam-HR800 micro Raman spectrometer equipped with a Peltier cooled charge-coupled device detector, and an Ar^+ ion laser excitation source with a wavelength of 488 nm. The overall spectral resolution was 1 cm^{-1} .

5.2 Room temperature Raman spectroscopic studies

Apart from the global structural changes obtained through XRD (**chapter 3.2**), it is essential to get more insights about local structural changes due to doping. In the present investigation, we used Raman spectroscopy to get precise information about local structure as Raman is more sensitive for local crystal symmetry. Figure 5.1 (a) and Fig. 5.1 (b) depict the room temperature Raman spectrum for HoCrO_3 and $\text{HoCr}_{0.5}\text{Fe}_{0.5}\text{O}_3$ compounds respectively. The ideal perovskite (ABO_3) consists simple cubic structure in which B-cations locate at the centre of the oxygen octahedra (BO_6), whereas the A-cations locate at the corners of the cube [158]. Essentially, rare earth orthochromites (RCrO_3) are distorted perovskites with a space group

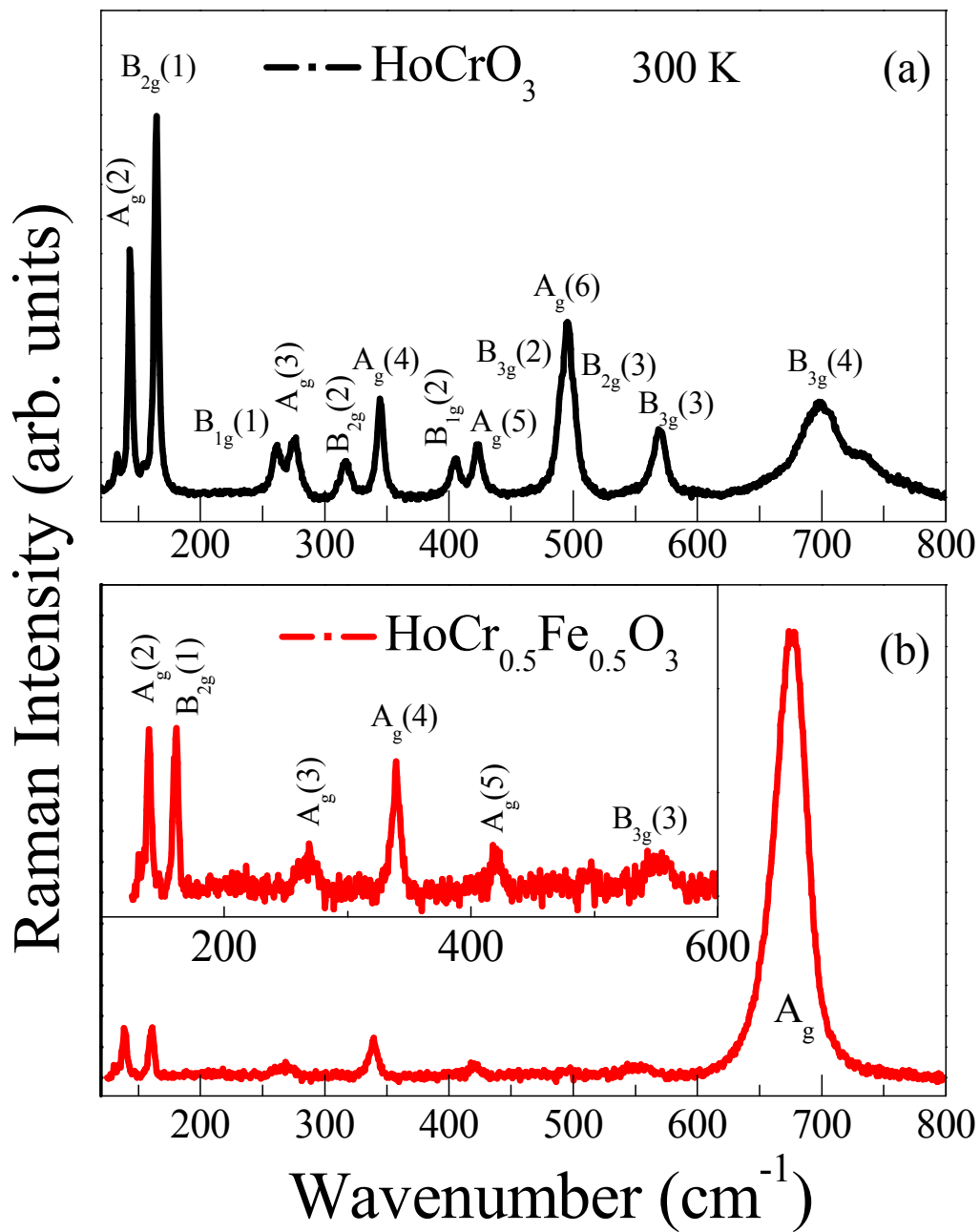


Figure 5.1: Room temperature Raman spectrum pertinent to (a) HoCrO_3 and (b) $\text{HoCr}_{0.5}\text{Fe}_{0.5}\text{O}_3$ compounds.

Table 5.1: The symmetry analysis of the Raman modes in $\text{HoCr}_{1-x}\text{Fe}_x\text{O}_3$ ($x = 0$ and 0.5) compounds recorded at room temperature. The activating distortion and the main atomic motions which corresponds to each phonon mode are assigned based on Ref. [136-137], [159], [222]. This table also reveals comparison between reported results and present ones.

Ref. 136-137, 159, 222	HoCrO_3	$\text{HoCr}_{0.5}\text{Fe}_{0.5}\text{O}_3$	Symmetry	Activating distortion	Main atomic motion
141.2	143.3	138.9	$A_g(2)$	rot [101]	A(z) out of plane
162.1	164.3	160.5	$B_{2g}(1)$	rot [101]	A(x)
260.3	261.3	259.2	$B_{1g}(1)$		
274.3	275.4	269.4	$A_g(3)$	rot [010], JT	BO_6 in phase rotations
315.2	316.8		$B_{2g}(2)$	A shift	A(z), O1(z)
341.3	344.6	339.1	$A_g(4)$	A shift	O1(x), A(-x)
401.6	404.8		$B_{1g}(2)$	A shift	A(z), O1(-z)
419.6	423.1	420.1	$A_g(5)$	rot [101]	BO_6 out-of-phase x rotations
486.9	489.4		$B_{3g}(2)$	rot [101]	Out-of-Phase O2 scissors like
493.3	495.6	495.5	$A_g(6)$	rot [101]	BO_6 bendings
502.0	501.3		$B_{2g}(3)$	rot [101]	BO_6 out-of-phase bendings
562.9	569.3	552.1	$B_{3g}(3)$	rot [101]	O2, O1 antistretching
		675.1	A_g		BO_6 In-phase stretching
693	697.9		$B_{3g}(4)$		

Pbnm. This orthorhombic Pbnm structure is obtained by two structural distortions from the ideal cubic structure, namely (i) rotation (tilt) of CrO₆ octahedra around [101] & [010] and (ii) displacement of rare-earth (R³⁺) ion. These structural distortions lead to lowering the symmetry which result the activation of Raman modes.

According to group theory analysis [161], twenty four (24) Raman active modes are possible for the orthorhombic Pbnm structure with four formula units per unit cell:

$$7A_g + 5B_{1g} + 7B_{2g} + 5B_{3g}$$

The assignment of these modes are done by following recent reports on orthorhombic RMnO₃ [220-221] and RCrO₃ systems [222, 194].

In case of the HoCrO₃ compound, twelve phonon modes have been observed as shown in Fig. 5.1 (a). On the other hand, the intensity of most of the Raman modes in the case of HoCr_{0.5}Fe_{0.5}O₃ compound appear to be suppressed as shown in Fig. 5.1 (b), which might be due to doping effect and high intensity of phonon mode observed around 670 cm⁻¹. The phonon modes pertinent to HoCr_{0.5}Fe_{0.5}O₃ compound below 600 cm⁻¹ can clearly be seen from the inset of Fig. 5.1 (b). A similar mode in Raman spectra has been observed in the thin films of BiFeO₃ [223-225] grown on a substrate (LaAlO₃), where there exists a mismatch in the lattice parameter between substrate and film, which leads to structural transformation from rhombohedral to tetragonal. However, we rule out the possibility of above origin for the presence of Raman mode around 670 cm⁻¹ in the HoCr_{0.5}Fe_{0.5}O₃ compound due to the fact that there is no structural transformation which we evidenced from our detailed phase purity study (**chapter 3.2**).

The phonon mode that prevailed around 670 cm⁻¹ in HoCr_{0.5}Fe_{0.5}O₃ compound is attributed to the in-phase stretching (breathing) mode of FeO₆/CrO₆ octahedra, which is due to orbital mediated electron – phonon coupling [120]. The assignment of the A_g mode for the peak that prevailed around 670 cm⁻¹ in HoCr_{0.5}Fe_{0.5}O₃ compound has been done based on the earlier reports on LaFe_{1-x}Cr_xO₃ (x = 0, 0.1,

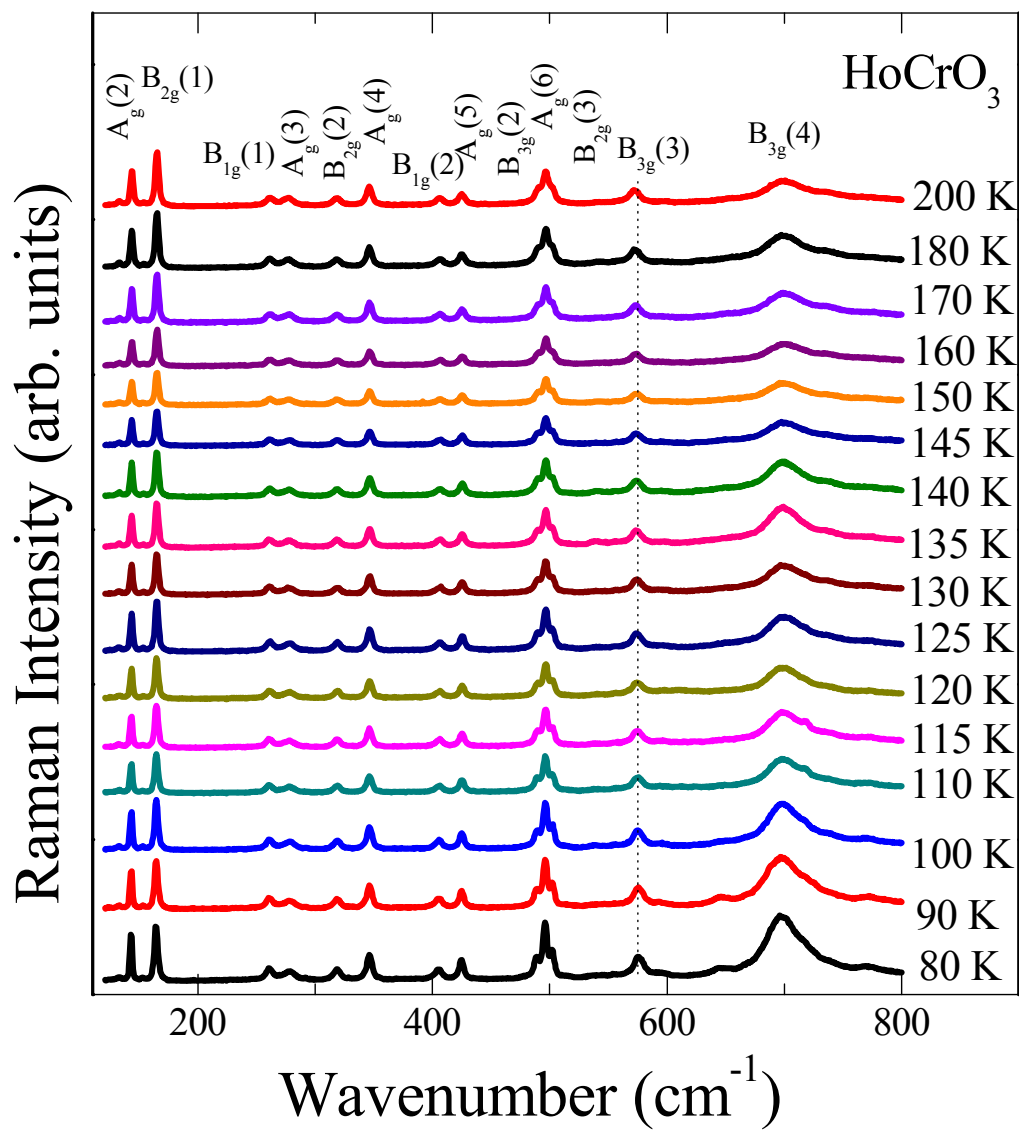


Figure 5.2: Raman spectrum of HoCrO₃ compound in the temperature range 80 – 200 K.

0.5, 0.9, 1.0) compounds [120]. Essentially, A_g -like symmetric oxygen mode is be activated through a charge transfer between Fe^{3+} and Cr^{3+} *via* an orbital mediated electron-phonon coupling mechanism, similar to the Franck-Condon effect observed in the Jahn-Teller active perovskite structured manganite, $LaMnO_3$ compounds [119-120, 163, 226].

The symmetry analysis of the observed phonon modes is done based on the recent study on $RCrO_3$ compounds, and comparison of the modes with the present study are summarised in Table 5.1. From the XRD studies (**chapter 3.2**), it is confirmed that $HoCrO_3$ and $HoCr_{0.5}Fe_{0.5}O_3$ are isostructural ($Pbnm$ symmetry) so that the lattice dynamics of these compounds may be similar. It has been found that Raman wavenumber is related to the bond length (l) by $1/\sqrt{l}$ [227], so that one can expect difference in Raman mode position if there is a change in bond length of the atoms. From the Table 5.1, it is evident that phonon modes in $HoCr_{0.5}Fe_{0.5}O_3$ compound lie in the lower wavenumber region when compared to $HoCrO_3$ compound, which might be due to an increase in bond length by the replacement of Cr^{3+} ions with Fe^{3+} ions.

5.3 Magnetic properties

As described in chapter 4.2, the temperature dependent magnetization measured for $HoCr_{1-x}Fe_xO_3$ ($x = 0$ and 0.5) compounds displays a distinct behaviour with multiple transition for both the compounds. It has been observed that Cr^{3+} moments and Ho^{3+} moments consist the magnetic ordering around 142 K (T_N) and 8 K (T_N^{Ho}) respectively in $HoCrO_3$ compound. With the addition of Fe^{3+} to Cr^{3+} in $HoCrO_3$, it is evident that there is shift of T_N from 142 - 273 K and T_N^{Ho} from 8 - 13 K. On the other hand, spin reorientation (SR) transition is observed around 150 K (T_{SR}) in $HoCr_{0.5}Fe_{0.5}O_3$ compound due to complex interplay between Ho^{3+} and Fe^{3+} moments [159].

5.4 Temperature dependent Raman scattering studies

To get more insights about the influence of magnetic ordering on phonon modes those prevail in $HoCr_{1-x}Fe_xO_3$ ($x = 0$ and 0.5) compounds, temperature dependent

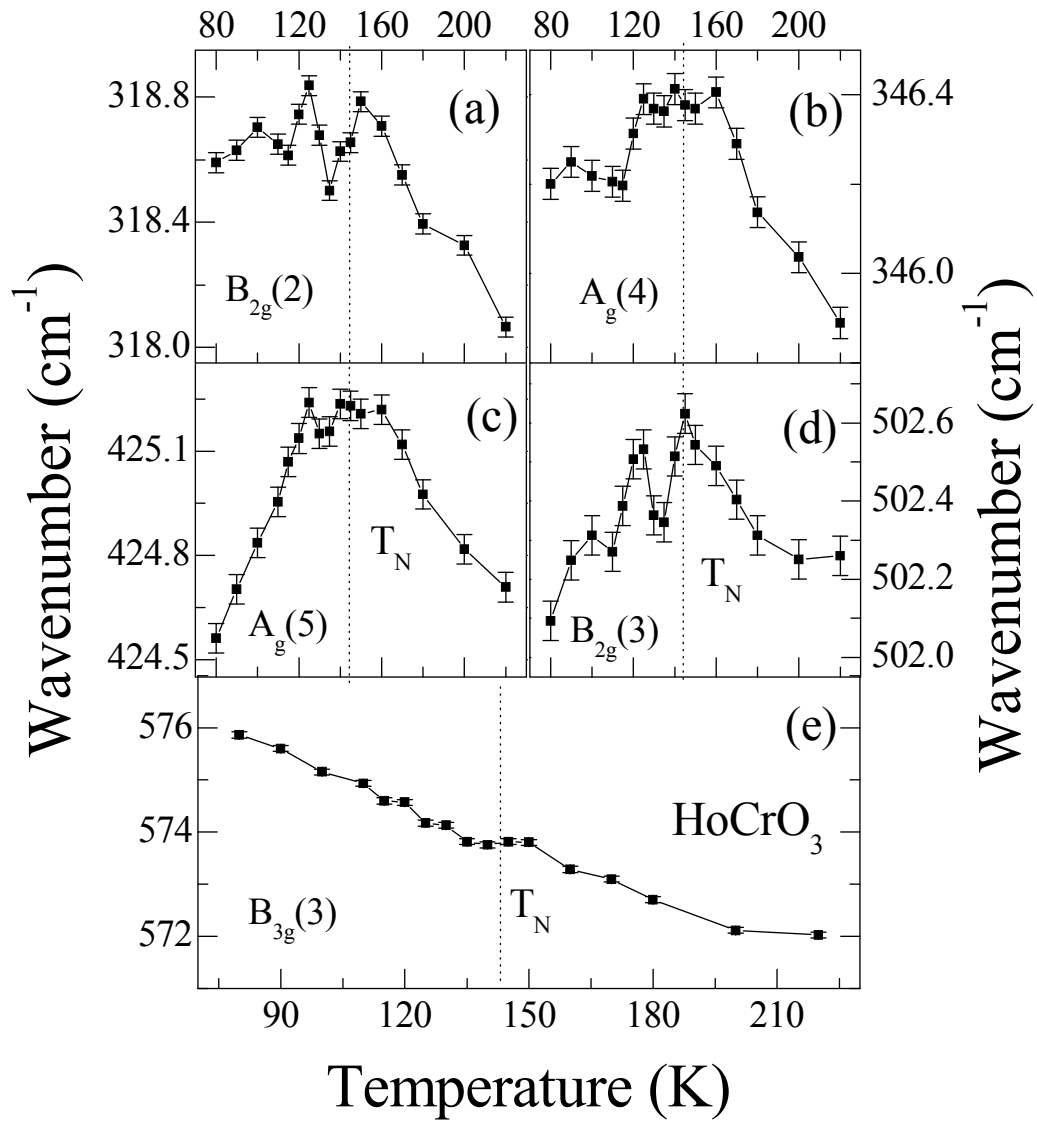


Figure 5.3: (a – e) variation of peak position pertinent to Raman modes of $B_{2g}(2)$, $A_g(4)$, $A_g(5)$, $B_{2g}(3)$ and $B_{3g}(3)$ respectively.

Raman spectrum were recorded above and below the Néel temperature for both the compounds. Temperature dependent Raman spectra pertinent to HoCrO_3 (120 - 800 cm^{-1} and 80 - 200 K) is shown in Fig. 5.2. In the temperature range that we investigated, we do not see any change in the Raman spectra associated with structural phase transition. The recorded spectrum are corrected by Bose-Einstein thermal factor [228]. To get the precise information about each phonon mode (viz. position, full width at half maxima (FWHM) and intensity), each spectrum is deconvoluted into Lorentzian profiles after baseline subtraction. Bhadram *et. al.*[136] have reported the softening of phonon modes in RCrO_3 compounds corresponding to magnetic rare earth ion, and the observed ferroelectricity has been explained on the basis of spin-phonon coupling.

In another study [139], anomalous behaviour of crystal field spectra and ferroelectricity have been observed in HoCrO_3 compound and correlated such intriguing phenomena to the possible distortion of Ho^{3+} ion due to Ho^{3+} - Cr^{3+} interaction [138]. However, through our temperature dependent Raman scattering study, no anomaly in the wavenumber as well as line width (FWHM) of the phonon modes corresponding Ho^{3+} ion below 200 cm^{-1} is evident around T_N , hinting that the displacement of Ho^{3+} ion may not be solely responsible for the observed ferroelectricity in HoCrO_3 compound [138].

From the Fig. 5.3 (a) – Fig. 5.3 (e), anomalous behaviour of the phonon modes centered around 316.8 cm^{-1} [$\text{B}_{2g}(2)$], 344.6 cm^{-1} [$\text{A}_g(4)$], 423.1 cm^{-1} [$\text{A}_g(5)$], 501.3 cm^{-1} [$\text{B}_{2g}(3)$], and 569.3 cm^{-1} [$\text{B}_{3g}(3)$] is evident across T_N . As the change in phonon wavenumber is large for $\text{B}_{3g}(3)$ mode compared with other modes, we restrict our discussion to $\text{B}_{3g}(3)$ mode in this work.

Figure 5.4 (a) depicts the temperature dependence of $\text{B}_{3g}(3)$ mode in HoCrO_3 compound. The expression for the temperature dependent wavenumber behaviour of a phonon mode in magnetic materials has been given as [50]

$$\omega(T) - \omega(0) = \Delta\omega_{\text{latt}} + \Delta\omega_{\text{ren}} + \Delta\omega_{\text{anh}} + \Delta\omega_{\text{sp-ph}} \quad \dots (5.1)$$

where $\omega(0)$ is the phonon wavenumber at 0 K. $\Delta\omega_{\text{latt}}$ represents the contribution from the lattice volume due to thermal excitation of atoms. $\Delta\omega_{\text{ren}}$ is the contribution from the renormalization of electronic states near the magnetic ordering temperature. $\Delta\omega_{\text{anh}}$ corresponds to the temperature dependent phonon wavenumber shift due to anharmonic vibrational potential at constant volume. $\Delta\omega_{\text{sp-ph}}$ is spin-phonon contribution towards the change in phonon wavenumber caused by the modulation of the exchange integral by lattice vibrations. The first term in equation 5.1 deals with isotropic change in volume and hence it is not applicable here. In the case of low carrier concentration, the second term can be neglected.

It has been proposed by Balkanski *et. al.* [229] that there can also be a contribution due to the anharmonicity for the phonon behaviour with temperature in the absence of structural phase transition [139]. From the Fig. 5.4 (a), it is evident that the phonon wavenumber increases as we go from high to low temperature up to T_N , this can be attributed to the anharmonic effect.

The experimental data above T_N was fitted with equation [229]:

$$\omega_{\text{anh}}(T) = \omega(0) - C \left(1 + 2 / (e^{\hbar\omega/kT} - 1) \right) \quad \dots\dots (5.2)$$

where $\omega(0)$ and C are adjustable parameters, and extrapolated for the temperature below T_N . The deviation of anharmonicity of $B_{3g}(3)$ mode below T_N is evident from the Fig. 5.4 (a), which suggests that there might be other factor apart from the anharmonicity which is responsible for the wavenumber shift of $B_{3g}(3)$ phonon mode in HoCrO_3 compound.

In a recent study on spin-phonon coupling in RCrO_3 compounds by Bhadram *et. al.*, [136], the hardening of the phonon mode below T_N has been reported and the behaviour is attributed to either direct spin-phonon coupling or coupling due to magnetostriction. Magnetostriction can produce a change in wavenumber of a phonon mode due to a volume change caused by the magnetic ordering of Cr^{3+} ions.

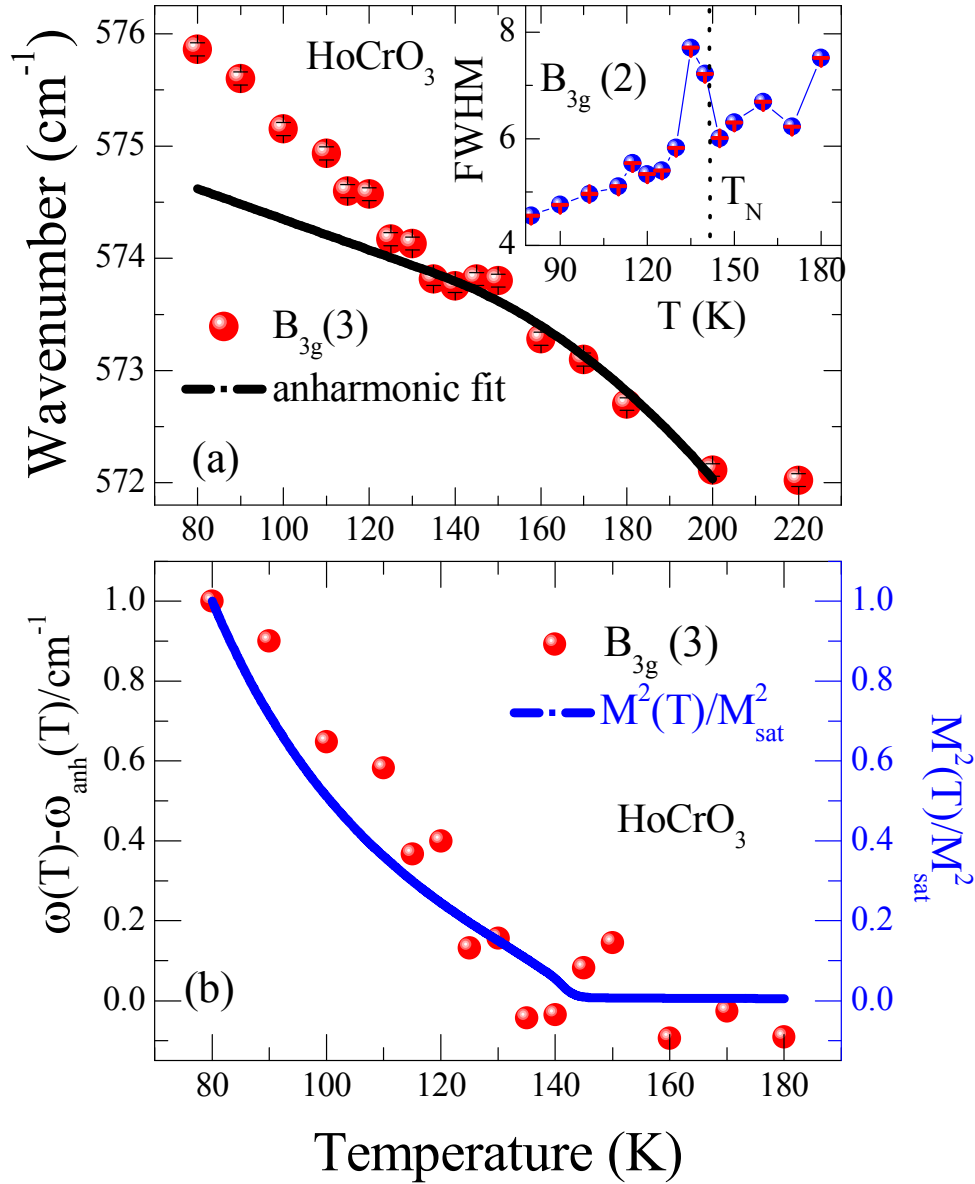


Figure 5.4: (a) Temperature dependence of phonon mode peak position for $B_{3g}(3)$ mode. Inset shows the variation of line width of $B_{3g}(2)$ mode. (b) Plot of $\Delta\omega(T)$ and $\frac{M^2(T)}{M_{\text{sat}}^2}$ as a function of temperature for $B_{3g}(3)$ mode pertinent to HoCrO_3 compound.

In that case, magnetostriction can't affect the FWHM of the phonon mode, which is related to phonon life time [230]. It has been reported [139] that magnetostriction could be the possible reason for anomalous behaviour of lattice parameters and volume below T_N in HoCrO_3 compound. To check the ambiguity whether the spin-phonon coupling is a direct coupling or mediated by magnetostriction, we plot the FWHM of phonon centered around 489.4 cm^{-1} [$B_{3g}(2)$] as shown in the inset of Fig. 5.4 (a). A clear anomaly is evident for temperature dependent FWHM of $B_{3g}(2)$ mode around T_N , which ruled out the magnetostriction effect on the phonon behaviour in HoCrO_3 compound.

The anomalous behaviour of the phonon wavenumber has been observed in other perovskites [231-233] with magnetic transition, which is associated with magnetic ordering induced renormalization of phonon modes and is proportional to spin-spin correlation function [50] $\langle S_i S_j \rangle$ for the nearest-neighbour spins localized at the i^{th} and j^{th} sites. Within the mean field approximation, phonon renormalization function is proportional to magnetization as follows

$$\Delta\omega(T) = \omega(T) - \omega_{\text{anh}}(T) \propto \frac{M^2(T)}{M_{\text{sat}}^2} \quad \dots (5.3)$$

where $M(T)$ is the temperature dependent magnetization. From the Fig. 5.4 (b), it is evident that phonon renormalization function $\Delta\omega$ scales well with square of the magnetization, which indicates the existence of spin-phonon coupling in HoCrO_3 compound.

Figure 5.5 shows the temperature dependent Raman spectrum pertinent to $\text{HoCr}_{0.5}\text{Fe}_{0.5}\text{O}_3$ ($120 - 800 \text{ cm}^{-1}$ and $200 - 300 \text{ K}$) compound. It is evident that indeed there is a shift for A_g phonon mode from $200 - 300 \text{ K}$ towards lower wave number. Figure 5.6 depicts the temperature evolution of A_g phonon mode position and corresponding line width (FWHM) for $\text{HoCr}_{0.5}\text{Fe}_{0.5}\text{O}_3$ compound. A clear deviation of the wavenumber of A_g mode from the anharmonic behaviour is demonstrated by fitting the graph with the equation 5.2 below T_N .

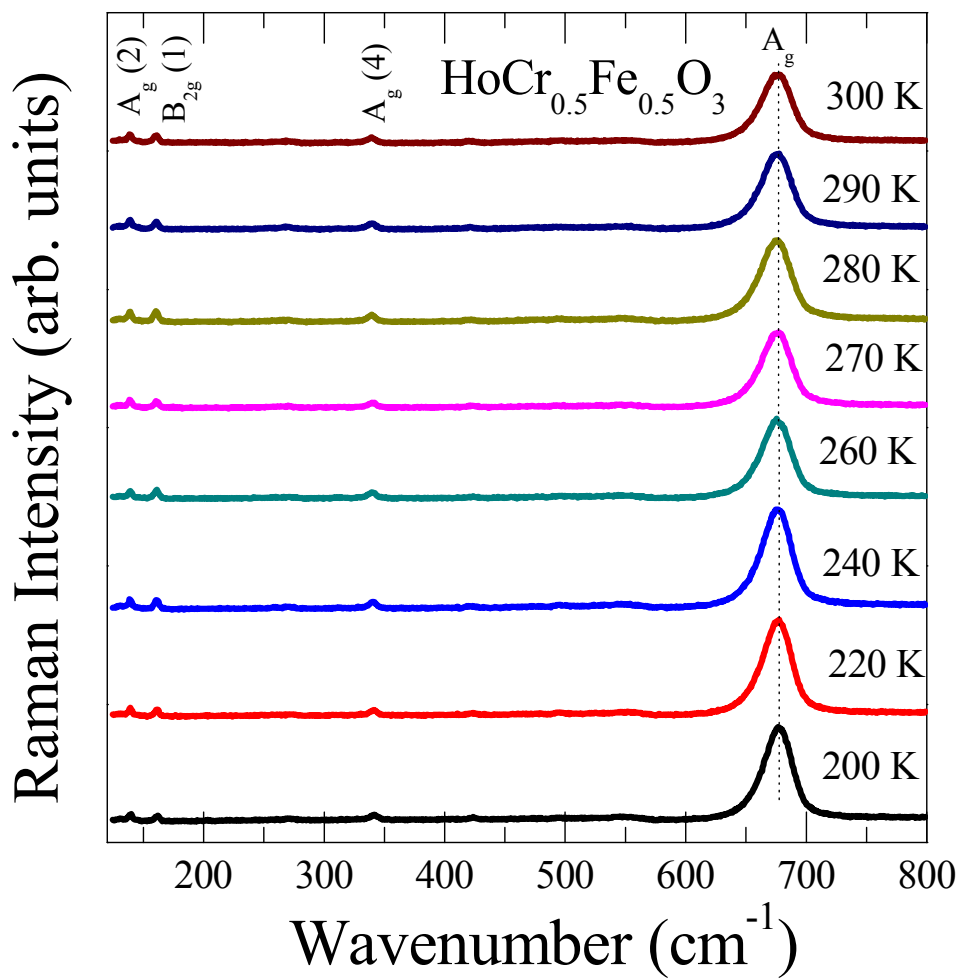


Figure 5.5: Temperature evolution (200 – 300 K) of Raman spectrum for $\text{HoCr}_{0.5}\text{Fe}_{0.5}\text{O}_3$ compound.

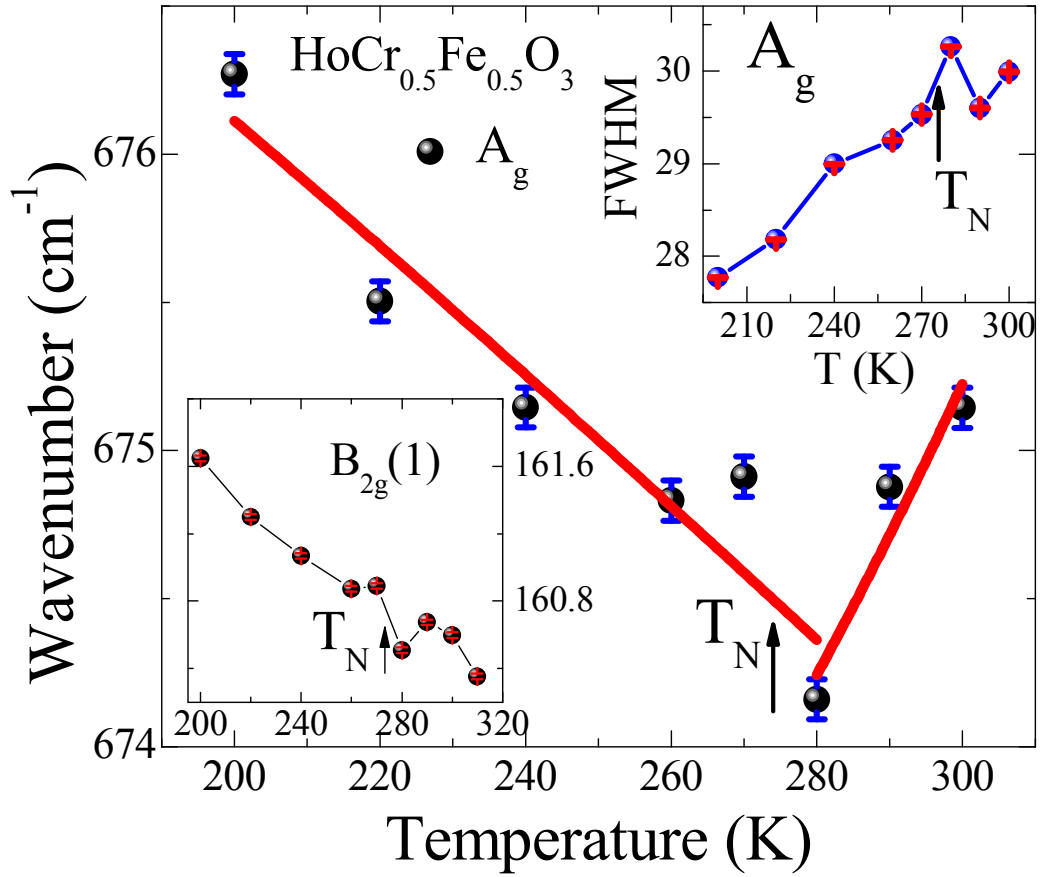


Figure 5.6: Temperature evolution (200 – 300 K) of the peak position of A_g mode in $\text{HoCr}_{0.5}\text{Fe}_{0.5}\text{O}_3$ compound, corresponding line width is shown in upper inset. Lower inset shows the temperature dependence of $B_{2g}(1)$ mode.

The deviation of wave number around the magnetic ordering in $\text{HoCr}_{0.5}\text{Fe}_{0.5}\text{O}_3$ might be due to spin-phonon coupling and quasi-harmonic effect due to change in lattice volume induced by magnetostriction [234]. The anomalous behaviour in the line width of A_g mode is observed around T_N as shown in the upper inset of Fig. 5.6. Since the line width is related to phonon life time and independent of lattice volume change, the sudden change in phonon wavenumber suggest the existence of spin-phonon coupling in $\text{HoCr}_{0.5}\text{Fe}_{0.5}\text{O}_3$. The changes in phonon life time suggests possible disorder in the system due to magnetic order at local level. Such a disorder can be influenced in the system around magnetic transition due to tilt or rotation of octahedral, ordering of $\text{Cr}^{3+}/\text{Fe}^{3+}$ ions in oxygen octahedral or displacement in the Ho^{3+} ion. Apart from that, there is a clear deviation in the wavenumber of phonon centered around 160.5 cm^{-1} [$B_{2g}(1)$], which is related to displacement of Ho^{3+} ion (lower inset of Fig. 5.6). Yin *et. al.*, reported the similar behaviour in $\text{DyCr}_{0.5}\text{Fe}_{0.5}\text{O}_3$ compound [114], and correlated to the observed ferroelectricity. This suggests that there is a possibility to observe the ferroelectricity in $\text{HoCr}_{0.5}\text{Fe}_{0.5}\text{O}_3$ compound, which may lead to multiferroicity near room temperature (below T_N).

5.5 Conclusions

In conclusion, temperature dependent Raman scattering studies on polycrystalline $\text{HoCr}_{1-x}\text{Fe}_x\text{O}_3$ ($x = 0$ and 0.5) compounds suggests no signature of structural phase transitions in the investigated temperature. In both the compounds, it is also evident that anomalous behaviour prevails for phonon modes around the magnetic transition temperature. The deviation of 569.3 cm^{-1} [$B_{3g}(3)$] phonon mode from the anharmonic behaviour below T_N scales well with square of the magnetization, hinting that a spin-phonon coupling in HoCrO_3 compound. Concurrently, we also attribute the evidenced spin – phonon coupling to the anomalous behaviour of A_g phonon mode and its line-width at T_N in $\text{HoCr}_{0.5}\text{Fe}_{0.5}\text{O}_3$ compound. Present results would be helpful in understanding and developing new multiferroic materials based on orthochromites.

Chapter 6

Summary and scope of future work

In this thesis, we essentially explored the correlation between the structural and magnetic properties of $\text{HoFe}_{1-x}\text{Cr}_x\text{O}_3$ ($0 \leq x \leq 1$) compounds. Based on the results that we presented in previous chapters, we summarize our results as follows

Structural and optical properties of $\text{HoFe}_{1-x}\text{Cr}_x\text{O}_3$ ($0 \leq x \leq 1$) compounds

- Room temperature x-ray diffraction (XRD) studies revealed that $\text{HoFe}_{1-x}\text{Cr}_x\text{O}_3$ compounds are crystallized in orthorhombically distorted perovskite structure with a space group of Pbnm.
- A decrease in lattice parameter is observed with Cr^{3+} doping, which is ascribed to the larger ionic radii of Fe^{3+} compared to that of Cr^{3+} .
- Indeed, there is an increase in tolerance factor and decrease in average tilt angle, hinting that the internal stress due to chemical pressure (Cr^{3+} doping), which leads to distortion of the lattice.
- There exists a mode with high intensity around 670 cm^{-1} with A_g like symmetry in the compounds having both Fe^{3+} and Cr^{3+} , which is attributed to the oxygen breathing mode due to the charge transfer between Fe^{3+} and Cr^{3+} through an orbital mediated electron-phonon coupling mechanism.
- The absorption spectra infer that there is a direct band gap for $\text{HoFe}_{1-x}\text{Cr}_x\text{O}_3$ compounds. A decrease in band gap from 2.07 eV ($x = 0$) to 1.94 eV ($x = 0.5$) and further increase up to 3.26 eV ($x = 1$) is observed in $\text{HoFe}_{1-x}\text{Cr}_x\text{O}_3$ compounds. The decrease in band gap is ascribed to broadening of oxygen p -orbital as a result of induced spin disorder due to

the Fe^{3+} and Cr^{3+} at B-site. On the other hand, an increase in band gap is explained on the basis of the reduction in the available unoccupied d -orbitals of Fe^{3+} at the conduction band.

Magnetic and magnetocaloric properties of $\text{HoFe}_{1-x}\text{Cr}_x\text{O}_3$ ($0 \leq x \leq 1$) compounds

- Temperature dependent magnetization studies on $\text{HoFe}_{1-x}\text{Cr}_x\text{O}_3$ compounds show various transitions such as antiferromagnetic (AFM) ordering of transition metal ion (T_N), spin reorientation transition (T_{SR}) and Ho^{3+} ordering.
- The observed decrease in T_N from 647 K ($x = 0$) to 142 K ($x = 1$) with Cr^{3+} doping is attributed to the dilution of Fe^{3+} - Fe^{3+} interaction as well as the enhancement of ferromagnetic interaction of adjacent Cr^{3+} moments through t - e hybridization as a result of the structural distortion.
- The evidenced increase in T_{SR} from 50 K ($x = 0$) to 150 K ($x = 0.5$) with Cr^{3+} doping is ascribed to the domination of Ho^{3+} - Fe^{3+} interaction over Fe^{3+} - Fe^{3+} at higher temperatures.
- The observed decrease in isomer shift (IS) with Cr^{3+} content has been correlated with a decrease in radial part of $3d$ wave function, which leads to an increase of the interaction between the effective nuclear charges and the $3s$ electrons.
- The small value for quadrupole splitting (QS) parameter for HoFeO_3 compound indicates the local environment remains octahedral at the unit cell. Increase in a value of QS with Cr^{3+} doping is due to the non-cubical electric field gradient acting on Fe atom, which arises from the distortion in FeO_6 octahedral by the substitution of Cr^{3+} ions at Fe site.
- The decrease in hyperfine field is ascribed to a decrease in strength of antiferromagnetic Fe^{3+} - Fe^{3+} interaction with the addition of Cr^{3+} at Fe-site.

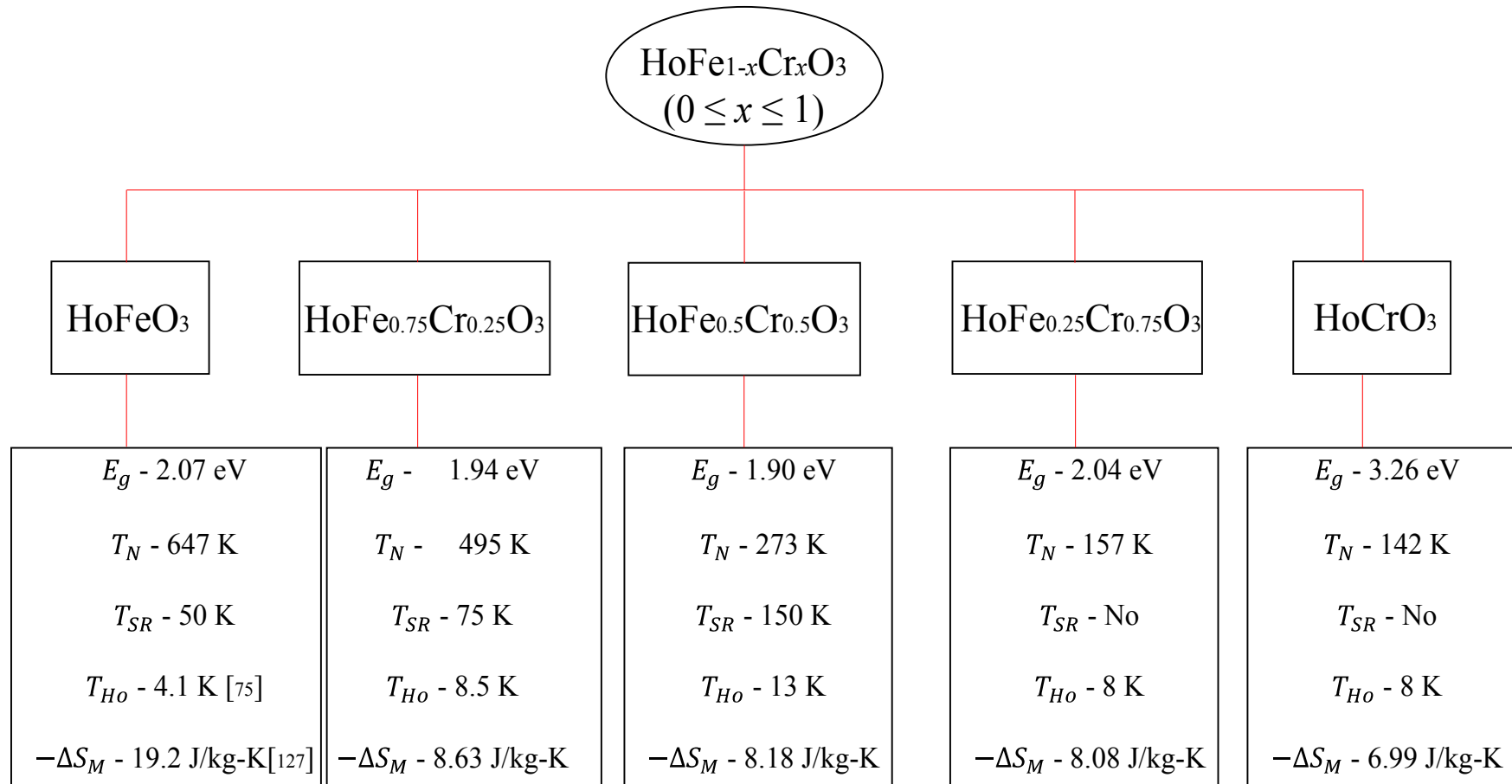
- The disappearance of six line Mössbauer spectra for $x \geq 0.5$ infers that the compounds are paramagnetic in nature at 300 K.
- M vs. H graph infer that the metamagnetic transitions are prevailed in the low field regime around Ho^{3+} ordering in $\text{HoFe}_{1-x}\text{Cr}_x\text{O}_3$ ($0.25 \leq x \leq 1$) compounds.
- Re-entrant magnetocaloric effect is evident in $\text{HoFe}_{1-x}\text{Cr}_x\text{O}_3$ (0.25, 0.75 and 1) compounds, which may be due to magnetization crossover and complex interactions.
- We trust that the large values of MCE obtained for $\text{HoFe}_{0.75}\text{Cr}_{0.25}\text{O}_3$ ($-\Delta S_M \sim 8.63$ J/kg-K at 9 K), $\text{HoFe}_{0.5}\text{Cr}_{0.5}\text{O}_3$ ($-\Delta S_M \sim 8.18$ J/kg-K at 12.5 K), $\text{HoFe}_{0.25}\text{Cr}_{0.75}\text{O}_3$ ($-\Delta S_M \sim 8.08$ J/kg-K at 11 K) and HoCrO_3 ($-\Delta S_M \sim 6.99$ J/kg-K at 9 K) compounds make them promising candidates for magnetic refrigeration applications below 30 K.

Spin-phonon coupling in $\text{HoCr}_{1-x}\text{Fe}_x\text{O}_3$ ($x = 0$ and 0.5) compounds

- Temperature dependent Raman scattering studies on $\text{HoCr}_{1-x}\text{Fe}_x\text{O}_3$ ($x = 0$ and 0.5) compounds suggest no signature of structural phase transitions in the investigated temperature range.
- In both the compounds, thermal evolution of phonon modes show anomalous behavior well above and below the magnetic transition temperature (T_N).
- The deviation of $B_{3g}(3)$ [569.3 cm^{-1}] mode from the expected anharmonic behaviour below T_N in HoCrO_3 compound is attributed to spin-phonon coupling caused by the modulation of super exchange integral by lattice vibration.
- On the other hand, the anomalous behavior of phonon frequency mode around 670 cm^{-1} (A_g) and its line-width around magnetic ordering is evident in $\text{HoCr}_{0.5}\text{Fe}_{0.5}\text{O}_3$ compound.
- Apart from that, a clear deviation of wavenumber of phonon around 160.5 cm^{-1} [$B_{2g}(1)$] suggests the possibility to observe ferroelectricity in the $\text{HoCr}_{0.5}\text{Fe}_{0.5}\text{O}_3$ compound.

- We believe that the present results would be helpful in obtaining new compounds with multiferroic properties near room temperature.

Summary



Scope of Future Work

- In this thesis, we have limited ourselves to structural, optical, magnetic and magnetocaloric properties of transition metal doped rare earth orthoferrites ($\text{HoFe}_{1-x}\text{Cr}_x\text{O}_3$ compounds). One can study the effect of rare earth substitution at rare earth site in orthoferrites on structural, optical, magnetic and magnetocaloric properties.
- Apart from that, it would be interesting to probe these compounds with Neutron diffraction technique in order to explore the magnetic structure.
- In addition, it would be also be interesting to prepare these compounds in the form of nanoparticles as well as thin films to study the size effects on the structural, optical, magnetic and magnetocaloric properties and their comparative study with the present results.
- Recently, rare earth orthoferrite (RFeO_3) and orthochromite (RCrO_3) compounds have drawn considerable attention due to possible multiferroicity above room temperature. Hence, it would be interesting to study multiferroic properties in the aforementioned compounds.

Highlights of the thesis

Orbital mediated electron-phonon coupling is observed in the compounds with mixed Fe and Cr at B-site

Bandgap values of $\text{HoFe}_{1-x}\text{Cr}_x\text{O}_3$ ($0 \leq x \leq 1$) compounds are reported for the first time

Spin-phonon coupling is observed in $\text{HoCr}_{1-x}\text{Fe}_x\text{O}_3$ ($x = 0$ and 0.5) compounds

Large value of magnetic entropy change ($-\Delta S_M \sim 8.63$ J/kg-K) is evident in $\text{HoFe}_{0.75}\text{Cr}_{0.25}\text{O}_3$ compound

References

- [1] A. R. Chakhmouradian and P. M. Woodward, Celebrating 175 years of perovskite research: a tribute to Roger H. Mitchell, *Physics and Chemistry of Minerals* 41 (6), (2014) 387-391.
- [2] R. H. Mitchell, *Perovskites: Modern and Ancient*, Almaz Press Inc., Ontario, 2002.
- [3] V. M. Goldschmidt, The laws of crystallochemistry, *Natural Sciences* 14 (21), (1926) 477-485.
- [4] H. D. Megaw, *Crystal structures: A working approach (studies in physics and chemistry)*. W. B. Saunders Co., Philadelphia PA, 1973.
- [5] A. M. Glazer, The classification of tilted octahedra in perovskites, *Acta Crystallographica Section B: structural Crystallography and Crystal Chemistry* 28 (11), (1972) 3384-3392.
- [6] A. M. Glazer, Simple ways of determining perovskite structures, *Acta Crystallographica Section A* 31 (6), (1975) 756-762.
- [7] P. M. Woodward, Octahedral tilting in perovskites. I. Geometrical considerations, *Acta Crystallographica Section B: Structural Science* 53 (1), (1997) 32-43.
- [8] P. M. Woodward, Octahedral tilting in perovskites. II. Structure stabilizing forces, *Acta Crystallographica B* 53 (1), (1997) 44-66.
- [9] W. M. Lufaso and P. M. Woodward, Jahn–Teller distortions, cation ordering and octahedral tilting in perovskites, *Acta Crystagraphica Section B: Structural Science* 60(1), (2004) 10-20.
- [10] C. J. Howard and H. T. Stokes, Group-theoretical analysis of octahedral tilting in perovskites, *Acta Crystallographica Section B: Structural Science* 54(6), (1998) 782-789.

- [11] C. J. Howard and Z. Zhang, Structure for perovskites with layered ordering of A-site cations, *Acta Crystallographica Section B: Structural Science* 60 (2), (2004) 249-251.
- [12] C. J. Howard and H. T. Stokes, Octahedral tilting in cation-ordered perovskites—a group-theoretical analysis, *Acta Crystallographica Section B: Structural Science* 60(6), (2004) 674-684.
- [13] C. J. Howard and H. T. Stokes, Structures and phase transitions in perovskites—a group-theoretical approach, *Acta Crystallographica Section A: Foundations of Crystallography* 61 (1), (2005) 93-111.
- [14] C. J. Howard and M. A. Carpenter, Octahedral tilting in cation-ordered Jahn–Teller distorted perovskites—a group-theoretical analysis, *Acta Crystallographica Section B: Structural Science* 66 (1), (2010) 40-50.
- [15] M. A. Carpenter and C. J. Howards, Symmetry rules and strain/order-parameter relationships for coupling between octahedral tilting and cooperative Jahn–Teller transitions in ABX_3 perovskites. I. Theory, *Acta Crystallographica Section B: Structural Science* 65 (2), (2009) 134-146.
- [16] A. P. Ramirez, Colossal magnetoresistance, *J. Phys.: Condens. Matter* 9, (1997) 8171.
- [17] B. Dieny, V. S. Speriosu, S. S. P. Parkin, B. A. Gurney, D. R. Wilhoit, and D. Mauri, Giant magnetoresistive in soft ferromagnetic multilayers, *Phys. Rev. B* 43, (1991) 1297.
- [18] K. I. Kobayashi, T. Kimura, H. Sawada, K. Terakura, and Y. Tokura, Room-temperature magnetoresistance in an oxide material with an ordered double-perovskite structure, *Nature* 395, (1998) 677.
- [19] T. Valet and A. Fert, Theory of the perpendicular magnetoresistance in magnetic multilayers, *Phys. Rev. B* 48, (1993) 7099.
- [20] R. E. Camley and J. Barnas, Theory of giant magnetoresistance effects in magnetic layered structures with antiferromagnetic coupling, *Phys. Rev. Lett.* 63, (1989) 664.

- [21] J Bednorz and K. A. Müller, Possible high T_c superconductivity in the Ba-La-Cu-O system, *Z. Phys. B: Condens. Matter* 64, (1986) 189.
- [22] F. C. Zhang and T. M. Rice, Effective Hamiltonian for the superconducting Cu oxides, *Phys. Rev. B* 37, (1988) 3759.
- [23] Y. Tokura, H. Takagi, and S. Uchida, A superconducting copper oxide compound with electrons as the charge carriers, *Nature* 337, (1989) 345.
- [24] I. I. Mazin, D. J. Singh, M. D. Johannes, and M. H. Du, Unconventional superconductivity with a sign reversal in the order parameter of $\text{LaFeAsO}_{1-x}\text{F}_x$, *Phys. Rev. Lett.* 101, (2008) 057003.
- [25] T. Yildirim, Origin of the 150-K anomaly in LaFeAsO : competing antiferromagnetic interactions, frustration, and a structural phase transition, *Phys. Rev. Lett.* 101, (2008) 057010.
- [26] A. Filippetti and N. A. Hill, Coexistence of magnetism and ferroelectricity in perovskites, *Phys. Rev. B* 65, (2002) 195120-11.
- [27] T. Kimura, T. Goto and H. Shintani, Magnetic control of ferroelectric polarization, *Nature* 426 (6962), (2003) 55-58.
- [28] A. Moreira dos Santos, A. K. Cheetham, T. Atou, Y. Syono, Y. Yamaguchi, K. Ohoyama, H. Chiba and C. N. R. Rao, Orbital ordering as the determinant for ferromagnetism in biferroic BiMnO_3 , *Phys. Rev. B* 66, (2002) 064425.
- [29] S. Blundell, *Magnetism in Condensed Matter*, Oxford University press, 2001.
- [30] C. Kittel, *Introduction to Solid State Physics*, 8th ed., John Wiley & Sons Ltd., 2005.
- [31] Cullity B. D, Graham C, *Introduction to magnetic materials*, Second ed. Wiley, 2009.
- [32] A. H. Morrish, *The Physical Principle of Magnetism*, IEEE press, 2001.
- [33] P. Weiss, La Variation du Ferromagnetsme avec la temperature, *Compt. Rend.* 143, (1906) 1136.

- [34] R. L. White, Review of recent work on the magnetic and spectroscopic properties of the rare-earth orthoferrites, *J. Appl. Phys.* 40, (1969) 1061.
- [35] E. Bousquet and A. Cano, Non-collinear magnetism in multiferroic perovskites, *J. Phys.: Condens. Matter* 28 (12), (2016) 1-28.
- [36] I. Weinberg and P. Larsen, Electron Paramagnetic Resonance and Antiferromagnetism in LaCrO_3 , *Nature* 192, (1961) 445.
- [37] M. Opel, Spintronic oxides grown by laser-MBE, *J. Phys. D: Appl. Phys.* 45, (2012) 033001.
- [38] J. B. Goodenough, *Magnetism and the Chemical Bond*, Wiley Interscience, New York, 1963.
- [39] J. B. Goodenough, Theory of the role of covalence in the perovskite-type manganites $[\text{La}, \text{M}(\text{II})] \text{MnO}_3$, *Phys. Rev.* 100, (1955) 564.
- [40] J. B. Goodenough and A. L. Loeb, Theory of ionic ordering, crystal distortion, and magnetic exchange due to covalent forces in spinels, *Phys. Rev.* 98, (1955) 391.
- [41] J. Kanamori, Superexchange interaction and symmetry properties of electron orbitals, *J. Phys. Chem. Solids.* 10, (1959) 87.
- [42] P. W. Anderson, New approach to the theory of superexchange interactions, *Phys. Rev.* 115, (1959) 2.
- [43] C. Zener, Interaction between the d shells in the transition metals, *Phys. Rev.* 81, (1951) 440.
- [44] C. Zener, Interaction between the d-shells in the transition metals. II. Ferromagnetic compounds of manganese with perovskite structure, *Phys. Rev.* 82, (1951) 403.
- [45] I. Dzyaloshinsky, A thermodynamic theory of “weak” ferromagnetism of antiferromagnetics, *J. Phys. Chem. Solids.* 4, (1958) 241.
- [46] T. Moriya, New mechanism of anisotropic superexchange interaction, *Phys. Rev. Lett.* 4, (1960) 228.
- [47] T. Moriya, Anisotropic superexchange interaction and weak ferromagnetism, *Phys. Rev.* 120, (1960) 91.

- [48] S. W. Cheong, and M. Mostovoy, Multiferroics: a magnetic twist for ferroelectricity, *Nat. Mater.* 6, (2007) 13.
- [49] T. Chatterji, M. Meven and P. J. Brown, *AIP Advances* 7, (2017) 045106.
- [50] E. Granado, A. García, J. A. Sanjurjo, C. Rettori, I. Torriani, F. Prado, R. D. Sánchez, A. Caneiro, and S. B. Oseroff, "Magnetic ordering effects in the Raman spectra of $\text{La}_{1-x}\text{Mn}_{1-x}\text{O}_3$." *Phys. Rev. B* 60, (1999) 11879.
- [51] Hayes. W and Loudon. R, *Scattering of Light by Crystals*, John Wiley & Sons, New York, 1978.
- [52] Lockwood D. J. and Cottam M. G, The spin-phonon interaction in FeF_2 and MnF_2 studied by Raman spectroscopy, *Journal of Applied Physics* 64, (1988) 5876.
- [53] R. M. Bozorth, H. J. Williams and D. E. Walsh, Magnetic properties of some orthoferrites and cyanides at low temperatures, *Phys. Rev.* 103, (1956) 572.
- [54] R. M. Bozorth, V. Kramer and J. P. Remeika, Origin of weak ferromagnetism in rare earth orthoferrites, *Phys. Rev. Lett.* 1, (1958) 362.
- [55] D. Treves, Magnetic studies of some orthoferrites, *Phys. Rev.* 125, (1962) 1843.
- [56] N. Singh, J. Y. Rhee and S. Auluck, Electronic and magneto-optical properties of rare-earth orthoferrites RFeO_3 (R= Y, Sm, Eu, Gd and Lu), *J. Korean Phys. Soc.* 53, (2008) 806.
- [57] M. Eibschütz, S. Shtrikman, and D. Treves, Mössbauer studies of Fe^{57} in orthoferrites. *Phys. Rev.* 156, (1967) 562.
- [58] Y. B. Bazaliy, L. T. Tsymbal, G. N. Nakazei and P. E. Wigen, The role of erbium magnetization anisotropy during the magnetic reorientation transition in ErFeO_3 , *J. Appl. Phys.* 95, (2004) 6622.
- [59] A. H. Bobeck, Properties and device applications of magnetic domains in orthoferrites, *Bell Sys. Tech. J.* 46, (1967) 1901.

- [60] A. H. Bobeck, R. F. Fischer, A. J. Perneski, J. P. Remeika and L. G. Van Uitert, Application of orthoferrites to domain-wall devices, *IEEE Trans. Mag.* 5, (1969) 544.
- [61] R. A. Laudise, Single crystals for bubble domain memories, *J. Crystal Growth.* 13/14, (1972) 27.
- [62] Y. Kita, F. Inose and M. Kasai, Two-dimensional shift array of magnetic bubbles and its application to pattern processing, INTERMAG Conference, Kyoto, Japan, paper 15.2, (1972) 367.
- [63] V. G. Bar'yakhtar, M. V. Chetkin, B. A. Ivanov and S. N. Gadetskii, Dynamics of topological magnetic solitons, *Springer Tracts on Modern Phys.*, Berlin, (1994) 129.
- [64] S. O. Demokritov, A. I. Kirilyuk, N. M. Kreines, V. I. Kudinov, V. B. Smirnov and M. V. Chetkin, Interaction of the moving domain wall with phonons, *J. Magn. Magn. Mater.* 102, (1991) 339.
- [65] Y. S. Didosyan, V. Y. Barash, N. A. Bovarin, H. Hauser and P. Fulmek, Magnetic field sensor by orthoferrites, *Sensors and Actuators A* 59, (1997) 56.
- [66] Y. S. Didosyan, H. Hauser and J. Nicolics, Magneto-optical current sensors of high bandwidth, *Sensors and Actuators* 81, (2000) 263.
- [67] Y. S. Didosyan, H. Hauser and P. Fulmek, Magneto-optical current sensor by domain wall motion in orthoferrites, *IEEE Transactions on instrument and measurement* 49, (2000) 14.
- [68] Y. S. Didosyan, H. Hauser, G. A. Reider and W. Toriser, Fast latching type optical switch, *J. Appl. Phys.* 95, (2004) 7339.
- [69] Y. S. Didosyan, H. Hauser, H. Wolfmayr, J. Nicolics and P. Fulmek, Magneto-optical rotational speed sensor, *Sensors and Actuators A* 106, (2003) 168.
- [70] Xinquan Niu, Honghua Li and Guoguang Liu, Photodegradation of Congo Red catalyzed by nanosized TiO₂, *Journal of Molecular Catalysis A: Chemical* 232, (2005) 89.

- [71] M. Gateshki, L. Suescun, S. Kolesnik, J. Mais, K. Świerczek, S. Short and B. Dabrowski, Structural, magnetic and electronic properties of $\text{LaNi}_{0.5}\text{Fe}_{0.5}\text{O}_3$ in the temperature range 5–1000 K, *Journal of Solid State Chemistry* 181, (2008) 1833.
- [72] Xiutao Ge, Yafei Liu and Xingqin Liu, Preparation and gas-sensitive properties of $\text{LaFe}_{1-y}\text{Co}_y\text{O}_3$ semiconducting materials, *Sensors and Actuators B* 79, (2001) 171.
- [73] Yuuki Hosoya, Yoshiteru Itagaki, Hiromichi Aono and Yoshihiko Sadaoka, Ozone detection in air using SmFeO_3 gas sensor, *Sensors and Actuators B* 108, (2005) 198.
- [74] S. Acharya, J. Mondal, S. Ghosh, S.K. Roy and P.K. Chakrabarti, Multiferroic behavior of lanthanum orthoferrite (LaFeO_3), *Materials Letters* 64, (2010) 415.
- [75] Y. Tokunaga, S. Iguchi, T. Arima, and Y. Tokura, Magnetic-field-induced ferroelectric state in DyFeO_3 , *Phys. Rev. Lett.* 101, (2008) 097205.
- [76] Zhou, Zhiqiang, Li Guo, Haixia Yang, Qiang Liu, and Feng Ye. Hydrothermal synthesis and magnetic properties of multiferroic rare-earth orthoferrites, *J. Alloys. And Compound* 583, (2014) 21-31.
- [77] Mikami, Itsuo, Mikio Hirano, and Gen-ichi Kamoshita, Mechanism of Magnetization Reversal of Rare-Earth Orthoferrite Single Crystals, *Jpn. J. Appl. Phys.* 12, (1973) 557.
- [78] Adhish Jaiswal, Raja Das, Suguna Adyanthaya and Pankaj Poddar, Surface effects on morin transition, exchange bias, and enhanced spin reorientation in chemically synthesized DyFeO_3 nanoparticles, *J. Phys. Chem. C* 115, (2011) 2954–2960.
- [79] E. F. Bertaut and G. T. Rado, H. Suhl (Eds.), *Magnetism III*, Academic Press Inc., New York, 1963.
- [80] L.T. Tsymbal, Ya. B. Bazaliy, V. N. Derkachenko, V. I. Kamenev, G. N. Kakazei, F. J. Palomares, and P. E. Wigen, Magnetic and structural

- properties of spin-reorientation transitions in orthoferrites, *J. Appl. Phys.* 101, (2007) 123919.
- [81] S. R. Brown and I. Hall, Mossbauer study of field-driven spin reorientations in YbFeO_3 at 4.2 K, *J. Phys.: Condens. Matter* 5, (1993) 4207-4214.
- [82] Claudio Cazorla and Daniel Errandonea, Giant mechanocaloric effects in fluorite-structured superionic materials, *Nano Lett.* 16 (5), (2016) 3124-3129.
- [83] Man Liu and Jie Wang, Giant electrocaloric effect in ferroelectric nanotubes near room temperature, *Scientific Reports* 5, (2015) 7728.
- [84] Gschneidner Jr K. A., Pecharsky V. K and Tsokol A. O., Recent developments in magnetocaloric materials, *Rep. Prog. Phys.* 68, (2005) 1479.
- [85] Gutfleisch Oliver, Matthew A. Willard, Ekkes Brück, Christina H. Chen, S. G. Sankar and J. Ping Liu, Magnetic Materials and Devices for the 21st Century: Stronger, Lighter, and More Energy Efficient, *Adv. Mater.* 23, (2011) 821.
- [86] B. G. Shen, J. R. Sun, F. X. Hu, H. W. Zhang and Z. H. Cheng, Recent Progress in Exploring Magnetocaloric Materials, *Adv. Mater.* 21, (2009) 4545.
- [87] J. H. Belo, J. S. Amaral, A. M. Pereira, V. S. Amaral and J. P. Araujo, On the Curie temperature dependency of the magnetocaloric effect, *Appl. Phys. Lett.* 100, (2012) 242407.
- [88] V. K. Pecharsky and K. A. Gschneidner Jr, Magnetocaloric effect and magnetic refrigeration, *J. Magn. Mater.* 200, (1999) 44.
- [89] K. A. Gschneidner and V. K. Pecharsky, Magnetocaloric Materials, *Annual Review of Materials Science* 30, (2000) 387.
- [90] K. Matsumoto, T. Kouen, R. Nishida, S. Abe, K. Kamiya, and T. Numazawa, Magnetocaloric Effect of RCo_2 (R : Er, Ho, Dy) Compounds for Regenerative Magnetic Refrigeration, *AIP Conf. Proc.* 850, (2006) 1581.
- [91] V. K. Pecharsky and K A Gschneidner Jr., Giant Magnetocaloric Effect in $\text{Gd}_5(\text{Si}_2\text{Ge}_2)$, *Phys. Rev. Lett.* 78 (23), (1997) 4494.

- [92] R. Bjork, C. R. H. Bahl, and M. Katter, Magnetocaloric properties of $\text{LaFe}_{13-x}\text{Co}_x\text{Si}_y$ and commercial grade Gd, *J. Magn. Magn. Mater.* 322, (2010) 3882.
- [93] H. Wada and Y. Tanabe, Giant magnetocaloric effect of $\text{MnAs}_{1-x}\text{Sb}_x$, *Appl. Phys. Lett.* 79, (2001) 3302.
- [94] M. P. Annaorazov, S. A. Nikitin, A. L. Tyurin, K. A. Asatryan and A. Kh. Dovletov, Anomalously high entropy change in FeRh alloy, *J. Appl. Phys.* 79, (1996) 1689.
- [95] M. Tishin, *Handbook of Magnetic Materials*, edited by K. H. J. Buschow, North Holland, Amsterdam, Vol. 12, (1999) 395–524.
- [96] K. A. Gschneidner Jr and V. K. Pecharsky. Magnetic refrigeration materials (invited). *J. Appl. Phys.* 85, (1999) 5365-5368.
- [97] H. Takeya, V.K. Pecharsky, K.A. Gschneidner Jr and J.O. Mooman. New type of magnetocaloric effect: Implications on low-temperature magnetic refrigeration using an Ericsson cycle. *Appl. Phys. Lett.* 64, (1994) 2739-2741.
- [98] E. Warburg, Magnetic investigations, *Ann. Phys. Chem.* 249, (1881) 141.
- [99] P. Debye, Some remarks on the magnetization at low temperature, *Ann. Phys.* 386, (1926) 1154.
- [100] W. F. Giauque, A thermodynamic treatment of certain magnetic effects. A proposed method of producing temperatures considerably below 1° absolute, *J. Am. Chem. Soc.* 49, (1927) 1864.
- [101] Ling-Wei Li, Review of magnetic properties and magnetocaloric effect in the intermetallic compounds of rare earth with low boiling point metals, *Chin. Phys. B* 25, (2016) 037502.
- [102] A. H. Morrish, *The Physical Principles of Magnetism*, chapter 3, Wiley, New York, 1965.
- [103] J.-H. Park, E. Vescovo, H.-J. Kim, C. Kwon, R. Ramesh and T. Venkatesan, Direct evidence for a half-metallic ferromagnet, *Nature* (London) 392, (1998) 794.

- [104] A. V. Kimel, C. D. Stanciu, P. A. Usachev, R. V. Pisarev, V. N. Gridnev, A. Kirilyuk and Th. Rasing, Optical excitation of antiferromagnetic resonance in TmFeO_3 , *Phys. Rev. B* 74, (2006) 060403.
- [105] A. V. Kimel, A. Kirilyuk, A. Tsvetkov, R. V. Pisarev, and Th. Rasing, Laser-induced ultrafast spin reorientation in the antiferromagnet TmFeO_3 , *Nature (London)* 429, (2004) 850.
- [106] J. Jiang, Z. Jin, G. Song, X. Lin, G. Ma, and S. Cao, Dynamical spin reorientation transition in NdFeO_3 single crystal observed with polarized terahertz time domain spectroscopy, *Appl. Phys. Lett.* 103, (2013) 062403.
- [107] A. V. Kimel, B. A. Ivanov, R. V. Pisarev, P. A. Usachev, A. Kirilyuk, and Th. Rasing, Inertia-driven spin switching in antiferromagnets, *Nat. Phys.* 5, (2009) 727.
- [108] Y. Tokunaga, N. Furukawa, H. Sakai, Y. Taguchi, T. h. Arima, and Y. Tokura, Composite domain walls in a multiferroic perovskite ferrite, *Nat. Mater.* 8, (2009) 558.
- [109] P. D. Battle, T. C. Gibb, A. J. Herod, S. H. Kim, and P. H. Munns, Investigation of magnetic frustration in A_2FeMO_6 ($\text{A} = \text{Ca}, \text{Sr}, \text{Ba}$; $\text{M} = \text{Nd}, \text{Ta}, \text{Sb}$) by magnetometry and Mössbauer spectroscopy, *J. Mater. Chem.* 5, (1995) 865.
- [110] Hideki Taguchi, Relationship between crystal structure and electrical properties of $\text{Nd}(\text{Cr}_{1-x}\text{Fe}_x)\text{O}_3$, *J. Solid State Chem.* 131, (1997) 108.
- [111] A. Dahmani, M. Taibi, M. Nogues, J. Aride, E. Loudghiri, and A. Belayachi, Magnetic properties of the perovskite compounds $\text{YFe}_{1-x}\text{Cr}_x\text{O}_3$ ($0.5 \leq x \leq 1$), *Mater. Chem. and Phys.* 77, (2003) 912.
- [112] J. Mao, Y. Sui, X. Zhang, Y. Su, X. Wang, Z. Liu, Y. Wang, R. Zhu, Y. Wang, W. Liu and J. Tang, Temperature-and magnetic-field-induced magnetization reversal in perovskite $\text{YFe}_{0.5}\text{Cr}_{0.5}\text{O}_3$, *Appl. Phys. Lett.* 98, (2011) 192510.
- [113] F. Pomiro, R. D. Sanchez, G. Cuello, A. Maignan, C. Martin and R. E. Carbonio, Spin reorientation, magnetization reversal, and negative thermal

- expansion observed in $\text{RFe}_{0.5}\text{Cr}_{0.5}\text{O}_3$ perovskites (R= Lu, Yb, Tm), *Phys. Rev. B* 94, (2016) 134402.
- [114] L. H. Yin, J. Yang, R. R. Zhang, J. M. Dai, W. H. Song and Y. P. Sun, Multiferroicity and magnetoelectric coupling enhanced large magnetocaloric effect in $\text{DyFe}_{0.5}\text{Cr}_{0.5}\text{O}_3$, *Appl. Phys. Lett.* 104, (2014) 032904.
- [115] L. H. Yin, J. Yang, P. Tong, X. Luo, W. H. Song, J. M. Dai, X. B. Zhu and Y. P. Sun, Magnetocaloric effect and influence of Fe/Cr disorder on the magnetization reversal and dielectric relaxation in $\text{RFe}_{0.5}\text{Cr}_{0.5}\text{O}_3$ systems, *Appl. Phys. Lett.* 110, (2017) 192904.
- [116] Shujuan Yuan, Ya Yang, Yiming Cao, Anhua Wu, Bo Lu, Shixun Cao and Jincang Zhang, Tailoring complex magnetic phase transition in HoFeO_3 , *Solid State Communications* 188, (2014) 19-22.
- [117] Zubida Habib, Kowsar Majid, Mohd. Ikram, Khalid Sultan, Sajad Ahmed Mir and K. Asokan, Influence of Ni substitution at B-site for Fe^{3+} ions on morphological, optical, and magnetic properties of HoFeO_3 ceramics, *Appl. Phys. A* 122, (2016) 550.
- [118] V. Gnezdilov, P. Lemmens, Yu. G. Pashkevich, Ch. Payen, K. Y. Choi, J. Hemberger, A. Loidl, and V. Tsurkan, Phonon anomalies and possible local lattice distortions in giant magnetocapacitive CdCr_2S_4 , *Phys. Rev. B* 84, (2011) 045106.
- [119] P. B. Allen and V. Perebeinos, Self-Trapped Exciton and Franck-Condon Spectra Predicted in LaMnO_3 , *Phys. Rev. Lett.* 83, (1999) 4828.
- [120] J. Anderasson, J. Holmud, C. S. Knee, M. Käll, L. Börjesson, S. Naler, J. Bäckström, M. Rübhausen, A. K. Azad and S-G. Eriksson, Franck-Condon higher order lattice excitations in the $\text{LaFe}_{1-x}\text{Cr}_x\text{O}_3$ ($x = 0, 0.1, 0.5, 0.9, 1.0$) perovskites due to Fe-Cr charge transfer effects, *Phys. Rev. B* 75, (2007) 104302.
- [121] A. Dubroka, J. Humlíček, M. V. Abrashev, Z. V. Popović, F. Sapiña, and A. Cantarero, Raman and infrared studies of $\text{La}_{1-y}\text{Sr}_y\text{Mn}_{1-x}\text{M}_x\text{O}_3$ ($M = \text{Cr}$,

- Co, Cu, Zn, Sc or Ga): Oxygen disorder and local vibrational modes, *Phys. Rev. B* 73, (2006) 224401.
- [122] M. Siemons and U. Simon, High throughput screening of the propylene and ethanol sensing properties of rare-earth orthoferrites and orthochromites, *Sensors and Actuators B* 126, (2007) 181.
- [123] I. E. Dzyaloshinskii, Thermodynamical Theory of ‘Weak’ Ferromagnetism in Antiferromagnetic Substances, *Sov. Phys. JETP* 5, (1957) 1259.
- [124] S. Iida, K. Ohbayashi and S. Kagoshima, Magnetism of rare earth orthoferrites as revealed from critical phenomena observation, *J. Phys. Colloques* 32, (1971) C1-654–C1-656.
- [125] L. Holmes, L. G. Van Uitert and Richard Hecker, Effect of Co on magnetic properties of ErFeO_3 , HoFeO_3 , and DyFeO_3 , *J. Appl. Phys.* 42, (1971) 657.
- [126] H. Shen, Z. Cheng, F. Hong, J. Xu, S. Yuan, S. Cao and X. Wang, Magnetic field induced discontinuous spin reorientation in ErFeO_3 single crystal, *Appl. Phys. Lett.* 103, (2013) 192404.
- [127] G.K. Shenoy and F.E. Wagner (Eds.), *Mössbauer Isomer Shift*, North-Holland Publ. Co, Amsterdam, New York, Oxford, 1978.
- [128] M. Shao, S. Cao, Y. Wang, S. Yuan, B. Kang and J. Zhang, Large magnetocaloric effect in HoFeO_3 single crystal, *Solid State Commun.* 152, (2012) 947.
- [129] A. McDannald, L. Kuna and M. Jain, Magnetic and magnetocaloric properties of bulk dysprosium chromite, *J. Appl. Phys.* 114, (2013) 113904.
- [130] R. Ramesh and N. A. Spaldin, Multiferroics: progress and prospects in thin films, *Nat. Mater.* 6, (2007) 21.
- [131] J. F. Scott, Applications of magnetoelectrics, *J. Mater. Chem.* 22, (2012) 4567.
- [132] P. Fischer, M. Polomska, I. Sosnowka, and M. Szymanski, Temperature dependence of the crystal and magnetic structures of BiFeO_3 , *J. Phys. C: Solid State Phys.* 13, (1980) 1931.

- [133] A. A. Belik, S. Iikubo, K. Kodama, N. Igawa, S. Shamoto, and E. Takayama-Muromachi, Neutron powder diffraction study on the crystal and magnetic structures of BiCrO_3 , *Chem. Mater.* 20, 3765 (2008).
- [134] W. S. Ferreira, J. A. Moreira, A. Almeida, M. R. Chaves, J. P. Araujo, J. B. Oliveira, J. M. M. Da Silva, M. A. Sa, T. M. Mendonca, P. S. Carvalho, J. Kreisel, J. L. Ribeiro, L. G. Vieira, P. B. Tavares and S. Mendona, Spin-phonon coupling and magnetoelectric properties: EuMnO_3 versus GdMnO_3 , *Phys. Rev. B* 79, (2009) 054303.
- [135] P. Anjali, V. R. Reddy, A. Gupta and V. G. Sathe, Study of spin-phonon coupling and magnetic field induced spin reorientation in polycrystalline multiferroic GdFeO_3 , *Materials Chemistry and Physics* 196, (2017) 205.
- [136] V. S. Bhadram, B. Rajeswaran, A. Sundaresan, and C. Narayana, Spin-phonon coupling in multiferroic RCrO_3 (R: Y, Lu, Gd, Eu, Sm): a Raman study, *Euro. Phys. Lett.* 101, (2013) 17008.
- [137] B. Rajeswaran, D. I. Khomskii, A. K. Zvezdin, C. N. R. Rao, and A. Sundaresan, Field-induced polar order at the Neel temperature of chromium in rare-earth orthochromites: Interplay of rare-earth and Cr magnetism, *Phys. Rev. B* 86, (2012) 214409.
- [138] A. Ghosh, A. Pal, K. Dey, S. Majumdar and S. Giri, Atypical multiferroicity of HoCrO_3 in bulk and film geometry, *J. Mater. Chem. C* 3, (2015) 4162.
- [139] C. M. Naveen Kumar, Crystal and spin structure and their relation to physical properties in some geometrical and spin spiral multiferroics, Forschungszentrum Jülich GmbH, Thesis, 2012.
- [140] A. R. West, *Solid State Chemistry and its Applications*, Wiley India, 2007.
- [141] S.-J.L. Kang, *Sintering, Densification, Grain Growth and Microstructure*, Elsevier, 2005.
- [142] B. D. Cullity, *Elements of X-ray diffraction*, Addison-Wesley Publishing Company, Inc, 1956.

- [143] M. A. Wahab, Solid State Physics, 2nd Edition, Narosa Publishing House, 2005.
- [144] H. M. Rietveld, A profile refinement method for nuclear and magnetic structures, *J. Appl. Cryst.* 2, (1969) 65.
- [145] R. A. Young, The Rietveld Method, A International Union of Crystallography Publication, New York, Oxford University, 1996.
- [146] Ian R. Lewis and Howell G. M. Edwards, Hand Book of Raman Spectroscopy, Taylor and Fransis group, 2001.
- [147] A. Hagfeldt and M. Graetzel, Light-Induced Redox Reactions in Nanocrystalline Systems, *Chem. Rev.* 95, (1995) 49.
- [148] Mössbauer spectroscopy, edited by D. P. E. Dickson and F. J. Berry, Cambridge University Press, Cambridge, 1986.
- [149] Simon Foner, Versatile and Sensitive Vibrating Sample Magnetometer, *Review of Scientific Instruments* 30, (1959) 548-557.
- [150] T. Van Duzer and C. W. Turner, Superconductive devices and Circuits Prentice Hall PTR, QC611.92V36 2nd ed., 1998.
- [151] http://www.icmmo.u-psud.fr/Labos/LCI/Service_SQUID/squid.php.
- [152] Quantum Design, San Diego, CA, Physical Property Measurement System (PPMS). Hardware Reference Manual, 3rd ed., 2000.
- [153] Jie Su, Yunfeng Guo, Juntong Zhang, Hui Sun, Ju He, Xiaomei Lu, Chaojing Lu and Jinsong Zhu, Ferroelectric behaviour and magnetocapacitance effect caused by Fe²⁺ in Ho₃Fe₅O₁₂ ceramics, *Ferroelectrics* 448, (2013) 71.
- [154] N. Kimizuka, A. Yamamoto, H. Ohashi, T. Sugihara, T. Sekine, The stability of the phases in the Ln₂O₃-FeO-Fe₂O₃ systems which are stable at elevated temperatures (Ln: Lanthanide elements and Y), *J. Solid State Chem.* 49, (1983) 65-76.
- [155] A.C. Larson and R.B. Von Dreele, General Structure Analysis System (GSAS), Los Alamos National Laboratory Report LAUR, (2004) 86-748.

- [156] R.D.Shannon, Revised effective ionic radii and systematic studies of interatomic distances in halides and chalcogenides, *Acta Cryst. A* 32, (1976) 751.
- [157] Tapan Chatterji, Bachir Ouladdiaf, P. Mandal, B. Bandyopadhyay, and B. Ghosh, Jahn-Teller transition in $\text{La}_{1-x}\text{Sr}_x\text{MnO}_3$ in the low-doping region ($0 < x < \sim 0.1$), *Phys. Rev. B* 66, (2002) 054403.
- [158] M. A. Peña and J. L. G. Fierro, Chemical structures and performance of perovskite oxides, *Chem Rev.* 101, (2001) 1981.
- [159] S. Venugopalan, M. Dutta, A. K. Ramdas, J. P. Remeika, Magnetic and vibrational excitations in rare-earth orthoferrites: A Raman scattering study, *Phys. Rev. B* 31, (1985) 1490.
- [160] Manoj K. Singh, Hyun M. Jang, H. C. Gupta and Ram S. Katiyar, Polarized Raman scattering and lattice eigenmodes of antiferromagnetic NdFeO_3 , *J. Raman Spectrosc.* 39, (2008) 842.
- [161] M. N. Iliev, M. V. Abrashev, H. -G. Lee, V. N. Popov, Y. Y. Sun, C. Thomsen, R. L. Meng, C. W. Chu, Raman spectroscopy of orthorhombic perovskite YMnO_3 and LaMnO_3 , *Phys. Rev. B* 57, (1998) 2872.
- [162] H. C. Gupta, Manoj Kumar Singh and L. M. Tiwari, Lattice dynamic investigation of Raman and infrared wavenumbers at the zone center of orthorhombic RFeO_3 ($\text{R} = \text{Tb}, \text{Dy}, \text{Ho}, \text{Er}, \text{Tm}$) perovskites, *J. Raman Spectrosc.* 33, (2002) 67.
- [163] Vasili Perebeinos and Philip B. Allen, Multiphonon resonant Raman scattering predicted in LaMnO_3 from the Franck-Condon process via self-trapped excitons, *Phys. Rev. B* 64, (2001) 085118.
- [164] K. Miura and K. Terakura, Electronic and magnetic properties of $\text{La}_2\text{FeCrO}_6$: Superexchange interaction for a d^5 - d^3 system, *Phys. Rev. B* 63, (2001) 104402.
- [165] J. Wong and C. A. Angell, Glass structure by spectroscopy, (Marcel Dekker, New York, 1976).

- [166] T. Arima, Y. Tokura, and J.B. Torrance, Variation of optical gaps in perovskite-type $3d$ transition-metal oxides, *Phys. Rev. B* 48, (1993) 17006.
- [167] Yong Wang, Kenneth Lopata, Scott A. Chambers, Niranjana Govind, and Peter V. Sushko, Optical absorption and band gap reduction in $(\text{Fe}_{1-x}\text{Cr}_x)_2\text{O}_3$ solid solutions: A first principles study, *J. Phys. Chem. C* 117, (2013) 25504.
- [168] J. S. Zhou and J. B. Goodenough, Intrinsic structural distortion in orthorhombic perovskite oxides, *Phys. Rev. B* 77, (2008) 132104.
- [169] J. S. Zhou, J. A. Alonso, V. Pomjakushin, J. B. Goodenough, Y. Ren, J. Q. Yan, and J. G. Cheng, Intrinsic structural distortion and superexchange interaction in the orthorhombic rare-earth perovskites RCrO_3 , *Phys. Rev. B* 81, (2010) 214115.
- [170] Takasu Hashimoto, Magnetic properties of the solid solutions between KMnF_3 , KCoF_3 and KNiF_3 , *J. Phys. Soc. Jpn.* 18, (1963) 1140.
- [171] O. Nikolov, T. Ruskov, G.P. Vorobyov, A.M. Kadomtseva, and I.B. Krynetskii, A new mechanism of the spin reorientations in HoFeO_3 , *Hyperfine Interact.* 54, (1990) 623.
- [172] J. C. Walling and Robert L. White, Study of magnetic interactions in HoFeO_3 , *Phys. Rev. B* 10, (1974) 4748.
- [173] J. S. Griffith, Spin Hamiltonian for even-electron systems having even multiplicity, *Phys. Rev.* 132, (1963) 316.
- [174] W. C. Koehler, E. O. Wollan, and M. K. Wilkinson, Neutron diffraction study of the magnetic properties of rare-earth iron perovskites, *Phys. Rev.* 118, (1960) 58.
- [175] Su Yuling, Zhang Jincang, Feng Zhenjie, Li Zijiong, Shen Yan, Cao Shixun, Magnetic properties of rare earth HoCrO_3 chromites, *J. Rare Earths* 29, (2011) 1060.
- [176] Y. L. Su, J. C. Zhang, L. Li, Z. J. Feng, B. Z. Li, Y. Zhou and S. X. Cao, Novel magnetization induced by phase coexistence in multiferroic HoCrO_3 chromites, *Ferroelectric* 410, (2011) 102.

- [177] N. Kumar and A. Sundaresan, On the observation of negative magnetization under zero-field-cooled process, *Solid State Commun.* 150, (2010) 1162.
- [178] Xinzhi Liu, Lijie Hao, Yuntao Liu, Xiaobai Ma, Siqin Meng, Yuqing Li, Jianbo Gao, Hao Guo, Wenze Han, Kai Sun, Meimei Wu, Xiping Chen, Lei Xie, Frank Klose, Dongfeng Chen, Neutron powder diffraction investigation of magnetic structure and spin reorientation transition of $\text{HoFe}_{1-x}\text{Cr}_x\text{O}_3$ solid solutions, *J. Magn. Mater.* 417, (2016) 382.
- [179] A. J. Dekker, *Solid State Physics*, Prentice-Hall, New York, 1970.
- [180] Vidhya G. Nair, L. Pal, V. Subramanian, and P. N. Santhosh, Structural, magnetic and magnetodielectric studies of metamagnetic $\text{DyFe}_{0.5}\text{Cr}_{0.5}\text{O}_3$, *J. Appl. Phys* 115, (2014) 17D728.
- [181] B. Rajeswaran, P. Mandal, Rana Saha, E. Suard, A. Sundaresan, and C. N. R. Rao, Ferroelectricity induced by cations of non-equivalent spins disordered in the weakly ferromagnetic perovskites, $\text{YCr}_{1-x}\text{M}_x\text{O}_3$ ($\text{M} = \text{Fe}$ or Mn), *Chem. Mater.* 24, (2012) 3591.
- [182] A. Wattiaux, J. C. Grenier, M. Pouchard, and P. Hagenmuller, Electrolytic oxygen evolution in alkaline medium on $\text{La}_{1-x}\text{Sr}_x\text{FeO}_{3-y}$ perovskite related ferrites, *J. Electrochem. Soc.* 134, (1987) 1718.
- [183] H. W. Brinks, H. Fjellvag, A. Kjekshus, and B. C. Hauback, Structure and magnetism of $\text{Pr}_{1-x}\text{Sr}_x\text{FeO}_{3-\delta}$, *J. Solid. State. Chem.* 150, (2000) 233.
- [184] Mahdi S. Lataifeh, Abed-Fatah D. Lehlooh, Mössbauer spectroscopy study of substituted yttrium ion garnets, *Solid State Commun.* 97, (1996) 805-807.
- [185] P. C. Piña, R. Buentello, H. Arriola and E. N. Nava, Mössbauer spectroscopy of lanthanum and holmium ferrites, *Hyperfine Interact* 185, (2008) 173–177.
- [186] Francis Menil, Systematic trends of the ^{57}Fe Mössbauer isomer shifts in (FeO_n) and (FeF_n) polyhedral. Evidence of a new correlation between the isomer shift and the inductive effect of the competing bond T-X ($\rightarrow\text{Fe}$)

- (where X is O or F and T any element with a formal positive charge), *J. Phys. Chem. Solids* 46, (1985) 763.
- [187] G.M. Bancroft, *Mössbauer Spectroscopy: An Introduction for Inorganic Chemists and Geochemists*, McGraw-Hill, New York, 1973.
- [188] I. B. Krynetskii, V. M. Matveev, *Metamagnetism and magnetostriction of the Ising antiferromagnet DyCrO₃*, *Phys. Solid State* 39, (1997) 584.
- [189] Q. Zhang, J. H. Cho, B. Li, W. J. Hu, and Z. D. Zhang, *Magnetocaloric effect in Ho₂In over a wide temperature range*, *Appl. Phys. Lett.* 94, (2009) 182501.
- [190] Zhong Wei, Au Chak-Tong, and Du You-Wei, *Review of magnetocaloric effect in perovskite-type oxides*, *Chin. Phys. B* 22, (2013) 057501.
- [191] T Chatterji, N Jalarvo, C M N Kumar, Y Xiao and Th Brückel, *Direct observation of low energy nuclear spin excitations in HoCrO₃ by high resolution neutron spectroscopy*, *J. Phys: Condens Matter* 25, (2013) 286003.
- [192] M. Shao, S. Cao, S. Yuan, J. Shang, B. Kang, B. Lu, and J. Zhang, *Large magnetocaloric effect induced by intrinsic structural transition in Dy_{1-x}Ho_xMnO₃*, *Appl. Phys. Lett.* 100, (2012) 222404.
- [193] M. C. Silva-Santana, C. A. daSilva, P. Barrozo, E. J. R. Plaza, L. de los Santos Valladares, N. O. Moreno, *Magnetocaloric and magnetic properties of SmFe_{0.5}Mn_{0.5}O₃ complex perovskite*, *J. Magn. Magn. Mater.* 401, (2016) 612.
- [194] S. Yin, V. Sharma, A. McDannald, A. Reboledo, and M. Jain, *RSC Adv* 6, (2016) 9475.
- [195] Lingwei Li, Ye Yuan, Yikun Zhang, Takahiro Namiki, Katsuhiko Nishimura, Rainer Pöttgen, and Shengqiang Zhou, *Giant low field magnetocaloric effect and field-induced metamagnetic transition in TmZn*, *Appl. Phys. Lett.* 107, (2015) 132401.
- [196] Lingwei Li, Katsuhiko Nishimura, Wayne D. Hutchison, Zhenghong Qian, Dexuan Huo, *Giant reversible magnetocaloric effect in ErMn₂Si₂ compound*

- with a second order magnetic phase transition, *Appl. Phys. Lett.* 100, (2012) 152403.
- [197] Yikun Zhang, Yang Yang, Xiao Xu, Long Hou, Zhongming Ren, Xi Li, and Gerhard Wilde, Large reversible magnetocaloric effect in $\text{RE}_2\text{Cu}_2\text{In}$ ($\text{RE} = \text{Er}$ and Tm) and enhanced refrigerant capacity in its composite materials, *J. Phys. D: Appl. Phys.* 49, (2016) 145002.
- [198] Lingwei Li, Takahiro Namiki, Dexuan Huo, Zhenghong Qian, and Katsuhiko Nishimura, Two successive magnetic transitions induced large refrigerant capacity in HoPdIn compound, *Appl. Phys. Lett.* 103, (2013) 222405.
- [199] Lingwei Li, Jing Wang, Kunpeng Su, Dexuan Huo, Yang Qi, Magnetic properties and magnetocaloric effect in metamagnetic $\text{RE}_2\text{Cu}_2\text{O}_5$ ($\text{RE} = \text{Dy}$ and Ho) cuprates, *J. Alloys Compd.* 658, (2016) 500-504.
- [200] S. Yin and M. Jain, Enhancement in magnetocaloric properties of holmium chromite by gadolinium substitution, *J. Appl. Phys.* 120, (2016) 043906.
- [201] Venkatesh Chandragiri, Kartik K Iyer and E. V. Sampathkumaran, Magnetic and magnetotransport behaviour of RFe_5Al_7 ($\text{R} = \text{Gd}$ and Dy): Observation of re-entrant inverse magnetocaloric phenomenon and asymmetric magnetoresistance behaviour, *Phys. Rev. B* 92, (2015) 014407.
- [202] Goncalo Oliveira, thesis “Local probing spinel and perovskite complex magnetic systems”, 2017.
- [203] O. Tegus, E. Brück, L. Zhang, Dagula, K. H. J. Buschow, F. R. de Boer, Magnetic-phase transitions and magnetocaloric effects, *Physica B: Condensed matter* 319, (2002) 174.
- [204] A. Arrott, Criterion for ferromagnetism from observations of magnetic isotherms, *Phys. Rev.* 108, (1957) 1394.
- [205] B. K. Banerjee, On a generalised approach to first and second order magnetic transitions, *Physics Letters* 12, (1964) 16.
- [206] T. Yamaguchi, Theory of spin reorientation in rare-earth orthochromites and orthoferrites, *J. Phys. Chem. Solids* 35, (1974) 479.

- [207] Shiqi Yin, Mohindar S. Seehra, Curtis J. Guild, Steven L. Suib, Narayan Poudel, Bernd Lorenz, and Menka Jain, Magnetic and magnetocaloric properties of HoCrO_3 tuned by selective rare-earth doping, *Phys. Rev. B* 95, (2017) 184421.
- [208] Mohit K. Sharma, Tathamay Basu, K. Mukherjee, and E. V. Sampathkumaran, Effect of rare-earth (Er and Gd) substitution on the magnetic and multiferroic properties of $\text{DyFe}_{0.5}\text{Cr}_{0.5}\text{O}_3$, *J. Phys.: Condens. Matter* 28, (2016) 426003.
- [209] A. Duran, A. M. Arevalo-Lopez, E. Castillo-Martinez, M. Garcia-Guaderrama, E. Moran, M. P. Cruz, F. Fernandez, and M. A. Alario-Franco, Magneto-thermal and dielectric properties of biferroic YCrO_3 prepared by combustion synthesis, *J. Solid State Chem.* 183, (2010) 1863.
- [210] Hirohisa Satoh, Shin-ichi Koseki, Masaki Takagi, Won Yang Chung, and Naoki Kamegashira, Heat capacities of LnCrO_3 ($\text{Ln} = \text{rare earth}$), *J. Alloys Compd.* 259, (1997) 176.
- [211] Yi Du, Zhen Xiang Cheng, Xiao-Lin Wang, and Shi Xue Dou, Structure, magnetic and thermal properties of $\text{Nd}_{1-x}\text{La}_x\text{CrO}_3$ ($0 \leq x \leq 1$), *J. Appl. Phys.* 108, (2010) 093914.
- [212] A. Rostamnejadi, M. Venkatesan, P. Kameli, H. Salamati, and J. M. D. Coey, Magnetocaloric effect in $\text{La}_{0.67}\text{Sr}_{0.33}\text{MnO}_3$ manganite above room temperature, *J. Magn. Magn. Mater.* 323, (2011) 2214.
- [213] Charlotte Mayer, Stephane Gorsse, Geraldine Ballon, Rafael Caballero-Flores, Victorino Franco, and Bernard Chevalier, Tunable magnetocaloric effect in Gd-based glassy ribbons, *J. Appl. Phys.* 110, (2011) 053920.
- [214] S. Gorsse, C. Mayer, and B. Chevalier, Magnetocaloric effect in $\text{Tb}_{60}\text{Ni}_{30}\text{Al}_{10}$ glass: A material that can either heat or cool upon magnetization, *J. Appl. Phys.* 109, (2011) 033914.
- [215] K. Saito, A. Sato, A. Bhattacharjee, and M. Sorai, High-precision detection of the heat-capacity anomaly due to spin reorientation in TmFeO_3 and HoFeO_3 , *Solid State Commun.* 120 (4), (2001) 129–132.

- [216] M. M. Vopson, Theory of giant-caloric effects in multiferroic materials, *J. Phys. D: Appl. Phys.* 46, (2013) 345304.
- [217] F. Bartolome, J. Bartolome, M. Castro, and J. J. Melero, Specific heat and magnetic interactions in NdCrO_3 , *Phys. Rev. B* 62, (2000) 1058.
- [218] Y. Su, J. Zhang, Z. Feng, L. Li, B. Li, Y. Zhou, Z. Chen and S. Cao, Magnetization reversal and $\text{Yb}^{3+}/\text{Cr}^{3+}$ spin ordering at low temperature for perovskite YbCrO_3 chromites, *J. Appl. Phys.* 108, (2010) 013905.
- [219] Preeti Gupta, and Pankaj Poddar, Study of magnetic and thermal properties of SmCrO_3 polycrystallites, *RSC Adv.* 6, (2016) 82014.
- [220] M. N. Iliev, M. V. Abrashev, J. Laverdière, S. Jandl, M. M. Gospodinov, Y. Q. Wang, Y. Y. Sun, Distortion-dependent Raman spectra and mode mixing in RMnO_3 perovskites ($\text{R} = \text{La, Pr, Nd, Sm, Eu, Gd, Tb, Dy, Ho, Y}$), *Phys. Rev. B* 73, (2006) 064302.
- [221] J. Laverdière, S. Jandl, A. A. Mukhin, V. Y. Ivanov, V. G. Ivanov, M. N. Iliev, Spin-phonon coupling in orthorhombic RMnO_3 ($\text{R} = \text{Pr, Nd, Sm, Eu, Gd, Tb, Dy, Ho, Y}$): A Raman study, *Phys. Rev. B* 73, (2006) 214301.
- [222] M. C. Weber, J. Kreisel, P. A. Thomas, M. Newton, K. Sardar, R. I. Walton, Phonon Raman scattering of RCrO_3 perovskites ($\text{R} = \text{Y, La, Pr, Sm, Gd, Dy, Ho, Yb, Lu}$), *Phys. Rev. B* 85, (2012) 054303.
- [223] J. Kreisel, P. Jadhav, O. Chaix-Pluchery, M. Varela, N. Dix, F. Sánchez, J. Fontcuberta, A phase transition close to room temperature in BiFeO_3 thin films, *J. Phys.: Condens. Matter* 23, (2011) 342202,.
- [224] C. Himcinschi, A. Bhatnagar, A. Talkenberger, M. Barchuk, D. R. T. Zahn, D. Rafaja, J. Kortus, M. Alexe, Optical properties of epitaxial BiFeO_3 thin films grown on LaAlO_3 , *Appl. Phys. Lett.* 106, (2015) 012908.
- [225] A. J. Hatt, N. A. Spaldin, C. Ederer, Strain-induced isosymmetric phase transition in BiFeO_3 , *Phys. Rev. B* 81, (2010) 054109.
- [226] R. Krüger, B. Schulz, S. Naler, R. Rauer, D. Budelmann, J. Bäckström, K. H. Kim, S-W. Cheong, V. Perebeinos, and M. Rübhausen, Orbital ordering

- in LaMnO₃ investigated by resonance Raman spectroscopy, *Phys. Rev. Lett.* 92, (2004) 097203.
- [227] S. Mukherjee, V. Ranjan, R. Gupta, A. Garg, Compositional dependence of structural parameters, polyhedral distortion and magnetic properties of gallium ferrite, *Sol. State Commun.* 152, 1181 (2012).
- [228] K. Y. Choi, P. Lemmens, G. Güntherodt, M. Patabiraman, G. Rangarajan, V. P. Gnezdilov, G. Balakrishnan, D. McK Paul, M. R. Lees, Raman scattering of Nd_{1-x}Sr_xMnO₃ ($x = 0.3, 0.5$), *J. Phys.: Condens. Matter* 15, (2003) 3333.
- [229] M. Balkanski, R. F. Wallis, E. Haro, Anharmonic effects in light scattering due to optical phonons in silicon, *Phys. Rev. B* 28, (1983) 1928.
- [230] A. Nonato, B. S. Araujo, A. P. Ayala, A. P. Maciel, S. Yanez-Vilar, M. Sanchez-Andujar, M. A. Senaris-Rodriguez, C. W. A. Paschoal, Spin-phonon and magnetostriction phenomena in CaMn₇O₁₂ helimagnet probed by Raman spectroscopy, *Appl. Phys. Lett.* 105, (2014) 222902.
- [231] K. D. Truong, M. P. Singh, S. Jandi, P. Fournier, Influence of Ni/Mn cation order on the spin-phonon coupling in multifunctional La₂NiMnO₆ epitaxial films by polarized Raman spectroscopy, *Phys. Rev. B* 80, (2009) 134424.
- [232] R. B. Macedo Filho, A. P. Ayala, C. W. de Araujo Paschoal, Spin-phonon coupling in Y₂NiMnO₆ double perovskite probed by Raman spectroscopy, *Appl. Phys. Lett.* 102, (2013) 192902.
- [233] M. N. Iliev, M. V. Abrashev, A. P. Litvinchuk, V. G. Hadjiev, H. Guo, and A. Gupta, Raman spectroscopy of ordered double perovskite La₂CoMnO₆ thin films, *Phys. Rev. B* 75, (2007) 104118.
- [234] M. Udagawa, K. Kohn, N. Koshizuka, T. Tsushima, K. Tsushima, Influence of magnetic ordering on the phonon Raman spectra in YCrO₃ and GdCrO₃, *Sol. State Commun.* 16, (1975) 779.

List of publications

Part of the thesis

1. Band gap tuning and orbital mediated electron-phonon coupling in $\text{HoFe}_{1-x}\text{Cr}_x\text{O}_3$ ($0 \leq x \leq 1$)
Ganesh Kotnana and S. Narayana Jammalamadaka
J. Appl. Phys. **118**, 124101 (2015).
2. Magnetic and hyperfine interactions in $\text{HoFe}_{1-x}\text{Cr}_x\text{O}_3$ ($0 \leq x \leq 1$) compounds
Ganesh Kotnana, V. Raghavendra Reddy and S. Narayana Jammalamadaka
J. Magn. Magn. Mater. **429**, 353-358 (2017).
3. Inverse and enhanced magnetocaloric properties of HoCrO_3
Ganesh Kotnana, Dwipak Prasad Sahu and S. Narayana Jammalamadaka
J. Alloy. Compd. **709**, 410-414 (2017).
4. Spin-Phonon Coupling in $\text{HoCr}_{1-x}\text{Fe}_x\text{O}_3$ ($x = 0$ and 0.5) compounds
Ganesh Kotnana, Vasant. G. Sathe and S. Narayana Jammalamadaka
Journal of Raman Spectroscopy **49**, 764 (2018).
5. Magnetic and magnetocaloric properties of $\text{HoCr}_{0.75}\text{Fe}_{0.25}\text{O}_3$ compound
Ganesh Kotnana, P. D. Babu and S. Narayana Jammalamadaka
AIP Advances **8**, 056407 (2018).
6. Specific heat and magnetocaloric properties of $\text{HoFe}_{1-x}\text{Cr}_x\text{O}_3$ ($x = 0.25$ and 0.75)
Compounds
Ganesh Kotnana, P. D. Babu and S. Narayana Jammalamadaka
(*Manuscript is under preparation*)

Other publications (not included in thesis)

1. Enhanced spin-reorientation temperature and origin of magnetocapacitance in HoFeO_3
Ganesh Kotnana and S. Narayana Jammalamadaka
J. Magn. Magn. Mater. **418**, 81-85 (2016).
2. Magnetocaloric effect and nature of magnetic transition in low dimensional DyCu_2
M. Venkat Narayana, **Ganesh Kotnana** and S. Narayana Jammalamadaka
J. Alloy. Compd. **683**, 56-61 (2016).
3. Spin-orbit coupling and Lorentz force enhanced efficiency of TiO_2 based dye sensitized solar cells
U. M. Kannan, M. Venkat Narayana, **Ganesh Kotnana**, L. Giribabu, Surya Prakash Singh, and S. Narayana Jammalamadaka
Phys. Status. Solidi A **214**, 1600691 (2017).

PRESENTATIONS IN CONFERENCES

1. Poster presentation entitled “Magnetocapacitance in HoFeO_3 ” at International Conference on Magnetic Materials and Applications (ICMAGMA 2015), held during 2nd – 4th December, 2015 at VIT University, Tamil Nadu, India.
2. Poster presentation entitled “Magnetocaloric properties of $\text{HoFe}_{0.5}\text{Cr}_{0.5}\text{O}_3$ compound” at Solid State Physics Symposium (DAE-SSPS 2016), held during 26th – 30th December at KIIT University, Bhubaneswar, India.
3. Poster presentation entitled “Structural and spectroscopic studies in $\text{HoCr}_{1-x}\text{Fe}_x\text{O}_3$ ($x = 0$ and 0.5) compounds” at Solid State Physics Symposium (DAE-SSPS 2017), held during 26th – 30th December at Bhabha Atomic Research Centre, Mumbai, India
4. Poster presentation entitled “Enhance magnetocaloric properties in Fe doped HoCrO_3 ” at International Conference on Magnetic Materials and Applications (ICMAGMA 2017), held during 1st – 3rd February, 2017 at Leonia International Centre for Exhibitions and Conventions, Hyderabad, India.

5. Poster presentation entitled “Magnetic and magnetocaloric properties of $\text{HoFe}_{1-x}\text{Cr}_x\text{O}_3$ ($0 \leq x \leq 1$) compounds” at 62nd Annual Conference on Magnetism and Magnetic Materials (MMM2017), held during 6th – 10th November, 2017 at The David L. Lawrence Convention Center in Pittsburgh, PA, USA.

Doctoral Committee Members

1. Dr. J. Suryanarayana (Thesis Adviser)

Associate professor,
Department of Physics,
Indian Institute of Technology Hyderabad,
Kandi, Sangareddy – 502 285,
Telangana, India.

2. Dr. V. Kanchana

Associate professor,
Department of Physics,
Indian Institute of Technology Hyderabad,
Kandi, Sangareddy – 502 285,
Telangana, India.

3. Dr. Atul Suresh Deshpande

Assistant professor,
Department of Materials Science and Metallurgical Engineering,
Indian Institute of Technology Hyderabad,
Kandi, Sangareddy – 502 285,
Telangana, India.